muSR studies in semiconductor, semimetal and powder systems and the application of a pulsed low energy muon beam line.

Donnelly, P. A

μSR STUDIES IN SEMICONDUCTOR, SEMIMETAL AND POWDER SYSTEMS AND THE APPLICATION OF A PULSED LOW ENERGY MUON BEAM LINE

by

P. A. Donnelly
MPhys. (Hons.), Warwick University, 1997

A thesis submitted in partial fulfilment of the
requirements for the degree of
Doctor of Philosophy

in

The Department of Physics,
University of Wales Swansea.
2003

DECLARATION AND STATEMENTS

DECLARATION

This work has not previously been accepted in substance for any degree and is not being concurrently submitted in candidature for any degree.

Signed .... (candidate)

Date .....20/11/03.....

STATEMENT 1

This thesis is the result of my own investigations, except where otherwise stated.

Other sources are acknowledged by footnotes and explicit references. A bibliography is appended.

Signed .. .. (candidate)

Date .....20/11/03.....

STATEMENT 2

I hereby give consent for my thesis, if accepted, to be available for photocopying and for inter-library loan, and for the title and summary to be made available to outside organisations.

Signed ..... (candidate)

Date .....20/11/03.....

ABSTRACT

The work contained in this thesis regards both surface related techniques, and the use of the muon as a hydrogen analogue in the investigation of fast charge-exchange cycles.

In the period 1997-1999, a pulsed low-energy μSR facility was developed, based on rare-gas moderation of a conventional pulsed muon beam. Various parameters of the technique were investigated, including the first direct measurements of the muon energy distribution. A full account is given of the sample-handling chamber designed and built for the adaptation of this source into a full user facility.

Using conventional muon beams, muonium interactions with the surface of a fine silica powder are studied, via the addition of condensed rare gases (He, Ar, Kr, Xe) in sub-monolayer coverages. We prove for the first time that at least 60% of the muonium yield is formed at the surface of the powder grains, and discount the possibility that bulk formed muonium is dissociated at the surface by ionised gas atoms. An additional mechanism for muonium formation, based on atomic recoil, is also proposed.

Muon spin-rotation measurements on silicon show the onset of a substantial paramagnetic shift from the muon Larmor frequency. The inferred fraction of the time spent as neutral paramagnetic muonium is close to unity above 600 K, so the capture rate of conduction electrons greatly exceeds the effective ionisation rate. Configuration-coordinate models for the interplay between site and charge state are described and developed.

A number of non-magnetic semimetals and metals are found to exhibit significant muon spin relaxation, which suggests a form of Korringa relaxation, also linked to conduction electron encounter at an interstitial site. The relationship between relaxation rate and muon Knight shift is investigated; we look briefly at the nature of defect screening; and consider the similarities with electronic activity seen in semiconductors at high temperatures.

Dedicated to my parents for support both moral and financial...

ACKNOWLEDGMENTS

There's been so much; it's tricky here to show
My thanks for ALL the help and supervision
I have received throughout five years or so
That I have worked at last to end this mission.

This thesis work was first made possible
When Peter Robert's studentship was made.
I only hope it's justified by all
The knowledge that within this book is laid.

Mike Charlton, firstly, I must thank you greatly,
With faith and boundless patience, me you guided
And, luckily my friend, I've noticed lately
The Cabin fever in my head's subsided.

Thanks too Steve Cox, a guv'ner of this field,
I owe you much, you've made it all less harrowing.
You helped me understand Muonium yield,
Charge-exchange, Knight shift, and motional narrowing.

Post-docs I've met don't come much better than
Those with whom friendship biscuits helped me forge,
So gratitude Bramdrup and Amsterdam
For the team who shared the basement by the morgue.

At UCL so many lent a hand;
Ted, Ivan with your technical insights,
Matt, Aysen, Dave, the whole Department, and
Vanita who still helps me reach great heights.

At RAL beam scientists and other guys
You all did help; forget you here I shouldn't.
Steve, Phil, and James always there to advise,
And Gavin funded me when others couldn't.

I cannot overlook the Slowmu team
From Cesare inspiration; from Klaus rage.
The Germans made it fun to build the beam,
And with Italy we found wiggles on the page.

Beholden too to Swansea girls and men,
A friendly bunch, and pretty bright to boot,
Not least of course, the group from room 6-10;
Thanks for discussions with and without fruit.

To those who made me welcome in their home,
Extending hospitality and food,
You must receive a verse all of your own,
Because you have my deepest gratitude.

For full support always, I have been moved
By the greatest set of friends that luck can bring.
And Janna too, as in your turn you proved
To be a sweet and understanding thing.

Thanks everyone to whom I am in debt,
But who in my silly rhyme I've missed,
Including all the folks I've never met,
e.g. the many in my reference list.

TABLE OF CONTENTS

LIST OF FIGURES

Number *Page*

Chapter 1

Chapter 2

Chapter 3

Chapter 4

Chapter 5

LIST OF TABLES

Table *Page*

1 INTRODUCTION

Muons, μ, the second of the lepton generations are produced, with energies appropriate to their use as an experimental probe, in the natural decay of charged pions. They in turn decay into electrons/positrons via the processes indicated in Figure 1.1, or its antiparticle equivalent, with a lifetime, τ_μ, of about 2.2 μs.

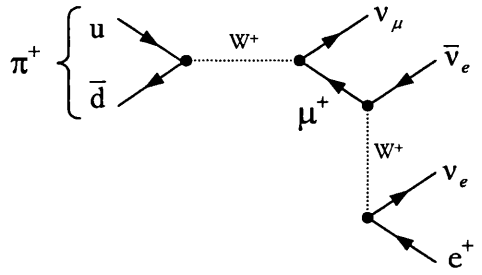

Figure 1.1. *Feynman diagram of the most prominent π decay mode.*

μ^- is often considered to be a 'heavy electron' (206.768 m_e – where m_e is electron mass). In matter, like the electron, it undergoes Coulomb attraction into atomic orbitals around a positive nucleus. It cascades quickly down to its ground state, very close to the nucleus, emitting x-ray photons. μ^-SR forms only a small subset of useful techniques covered by the acronym μSR* as both its lifetime and statistics are significantly reduced respectively by capture into the nucleus and fast depolarisation (i.e. a residual polarisation of ~1/6 after reaching the $1s_{½}$ state) [1.1].

The positive muon, on the other hand, behaves in matter rather like a 'light proton' (0.1126 m_p – where m_p is proton mass). It avoids positively charged nuclei, and generally

* Muon Spin Rotation/ Relaxation/ Resonance or simply Research – depending on applied techniques.

occupies interstitial sites. μ^+ may also capture its own electron to form the hydrogen-like muonium pseudo-atom (Mu). Mu has a Bohr radius and binding energy almost identical to H, and can be considered a valuable, readily detectable, light isotope in studying hydrogen diffusion mechanisms and chemical reactions [1.2]. Furthermore, Mu, being a purely leptonic system, and free from the influence of the strong interaction, provides a rigorous test bed for the theoretical framework of the Standard Model of particle physics [1.3]. A summary of muon properties is given in Table 1.1.

Table 1.1. Particle properties in the π-e decay chain [1.4].

	$\pi^{+(-)}$	$\mu^{+(-)}$	$e^{+(-)}$
Mass	139.57018(35) MeV 0.14983476(38) u $2.4880642(62)\times10^{-28}$ kg	105.6583568(52) MeV* 0.1134289168(34) u $1.88353109(16)\times10^{-28}$ kg	0.51099907(15) MeV $5.485799110(12)\times10^{-4}$ u $9.10938188(72)\times10^{-31}$ kg
Spin	0	½	½
Mean Life, τ (in vacuo)	26.03 ns	2.1970 μs	$> 4.3 \times 10^{23}$ yr
Magnetic Moment, μ		$+(-)4.49044813(22)\times10^{-26}$ JT^{-1} $+(-)4.84197085(15)\times10^{-3}$ μ_B	$+(-)928.476362(37)\times10^{-26}$ JT^{-1} $+(-)1.0011596521869(41)$ μ_B
Principle Decay	$\mu^+\nu_\mu$	$e^+\nu_e\bar{\nu}_\mu$	stable
μ^+ spin precession: $\tilde{\gamma}_\mu = \frac{\gamma_\mu}{2\pi} = \frac{g_\mu \mu_\mu}{h}$ = 13.569686 kHz G^{-1}			

* m_μ/m_e = 206.7682657(63) ; m_μ/m_p = 0.1126095173(34) , i.e.~1/9.

This chapter aims to acquaint the reader with the basic principles of μ^+SR, with regard to the experimental environment and the attainable information, and will be concerned primarily with the positive muon as applied to the systems studied in this work. For a more detailed treatment, including many additional aspects of μSR, the reader is referred to the following authoritative reviews [1.5, 1.6, 1.7].

1.1 A Brief History of Muon Spin Research

The first observed muon is attributed to P. Kunze [1.8] in 1933 via cosmic ray interactions inside a Wilson cloud chamber. However, it was not until observations by Neddermeyer and Anderson [1.9] in 1936 that the tracks were attributed to a new particle; more massive than an electron and lighter than a proton. At first thought to be Yukawas' meson (the predicted mediator of the strong nuclear force), it took the theoretical suggestions of Tanikawa *et al.* [1.10], in 1946, and finally experimental verification by Powell and co-workers [1.11] in 1947, before it was confirmed to involve two decay events; following the process $\pi \rightarrow \mu \rightarrow e$, shown in Figure 1.1. The muon took up a natural, but unexpected, position in the emerging Standard Model.

The study of muon decay as a test for parity non-conservation in the weak interaction was proposed by Lee and Yang in 1956 [1.12], and when this experiment was performed later that year by Garwin, Ledermann and Weinrich [1.13] they used techniques that were to form the backbone of all muon spin research (μSR) experiments to follow.

Towards the end of the 1950s, the first generation of proton accelerators made it possible to begin to use methods of muon spin rotation routinely, as well as to explore aspects of fundamental particle physics and muon catalysed fusion (μCF). The increased intensity of the second generation 'meson factories' in the mid 1970s, and the first pulsed facilities in the 1980s, brought respectable timescales and greater diversity to the experiments, and have allowed muon science to become firmly established [1.14].

μSR, being concerned with the time evolution of the muon spin, naturally brings comparisons to techniques such as nuclear magnetic resonance (NMR) and electron spin resonance (ESR). One of the great advantages of μSR is that it begins with a perfectly polarised probe, regardless of the conditions inside the medium to be studied. In contrast,

NMR and ESR rely upon a thermal equilibrium spin polarisation, usually achieved at low temperatures in strong magnetic fields; e.g. the equilibrium proton polarisation in a field of 1 T at room temperature is ~ 3×10^{-6} †.

1.2 Muon Production from Pion Decay

To produce pions in the laboratory, it is necessary to bombard nucleons with other nucleons of sufficient kinetic energy (greater than the pion rest mass of ~140 MeV). The results of interest are the following standard reactions,

$$\begin{aligned} &p+p \rightarrow p+n+\pi^{+}, \\ &p+n \rightarrow p+p+\pi^{-}, \text{and} \\ &p+n \rightarrow n+n+\pi^{+}. \end{aligned} \qquad (1.1)$$

These are typically achieved by passing an accelerated proton beam through a target of low Z material such as graphite. The optimum cross-sections for such 'single pion' production occur roughly in the 500-1000 MeV energy range, producing pions with energies peaked in the range 200-300 MeV (proton energies in excess of ~1500 MeV are required for significant 'double pion' production cross-sections)[1.15].

The pion decays after approximately 26 ns, whereby, due to violation of parity conservation – the neutrino is only produced with negative helicity (positive for the antineutrino) – the conservation of linear and angular momentum in the two body decay forces the $\mu^{+(-)}$ to have negative (positive) helicity; see Figure 1.2.

† the ratio given by the Boltzmann factor of the corresponding energy splitting.

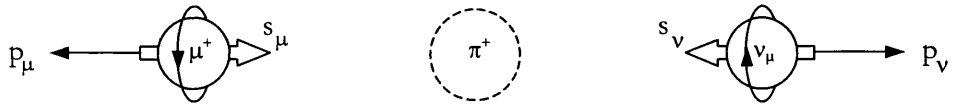

Figure 1.2. *Conservation of momentum in the π rest frame.*

In the rest frame of the pion, positive muons are therefore produced 100% spin polarised antiparallel to their momentum, which has a unique value of

$$\left|\mathbf{p}_\mu\right| = \frac{m_\pi^2 - m_\mu^2}{2\,m_\pi} c = 29.79 \text{ MeV/c}, \qquad (1.2)$$

corresponding to an energy of 4.2 MeV; i.e. a velocity in this frame of reference of $\left|\mathbf{v}_\mu\right| = 0.2714c$ $(= 81.36\times10^6 \text{ m s}^{-1}$ or $178.75 \text{ m } \tau_\mu^{-1})$.

A typical facility is the European Muon Facility at ISIS, RAL, Figure 1.3.a, where muons are selected from pions that come to rest in the surface of the production target, as detailed in Figure 1.3.b, and are guided to an experimental area. They are therefore produced almost mono-energetically, although a small momentum byte is incurred by some sub-surface π^+ distribution‡. These beams are known as 'ARIZONA' or, more obviously, 'surface' beams [1.16]. This method can necessarily produce only positive μ^+, since negative π^- stopping in the surface of the graphite target are immediately captured by the carbon nuclei, resulting in a nuclear disintegration. The alternative is a 'decay channel'; so called because the muons are collected from pions that decay in flight. This is a considerably more expensive option and has polarisation reduced to ~70-80% due to the additional π momentum, but has the advantage that the muon momentum can be selected across a broad range. A decay channel, also the only method available for creating μ^- beams, operates at the Japanese RIKEN-RAL facility at ISIS (indicated on Figure 1.3.a).

‡ At ISIS the muon beam has a mean momentum of 26.5 MeV/c, with 10% 'momentum byte'.

a

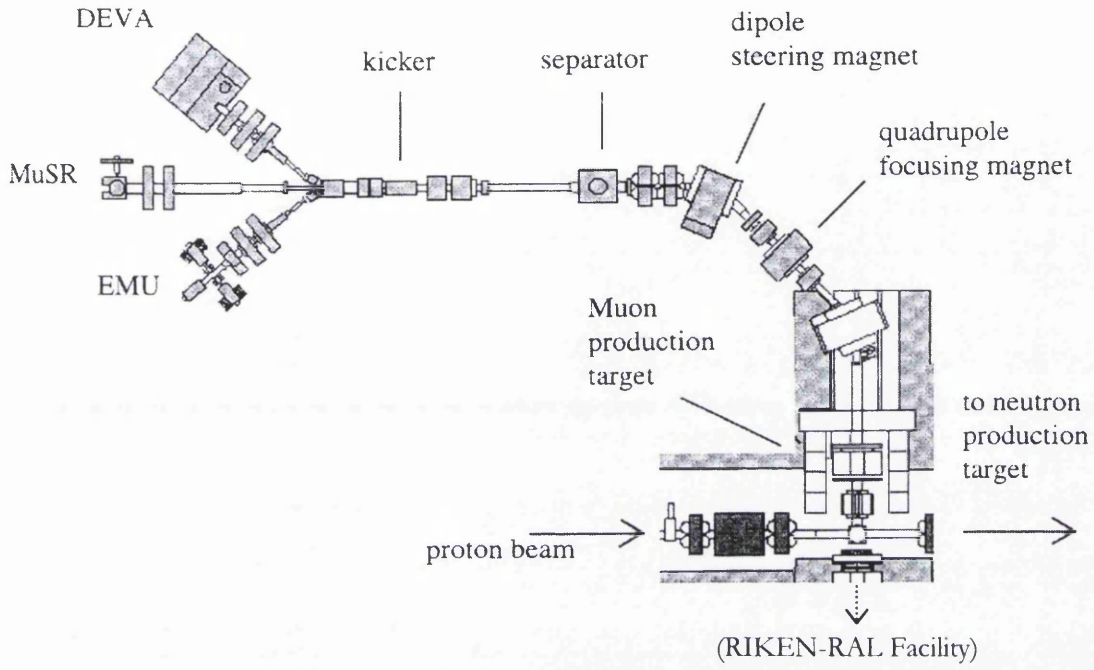

b

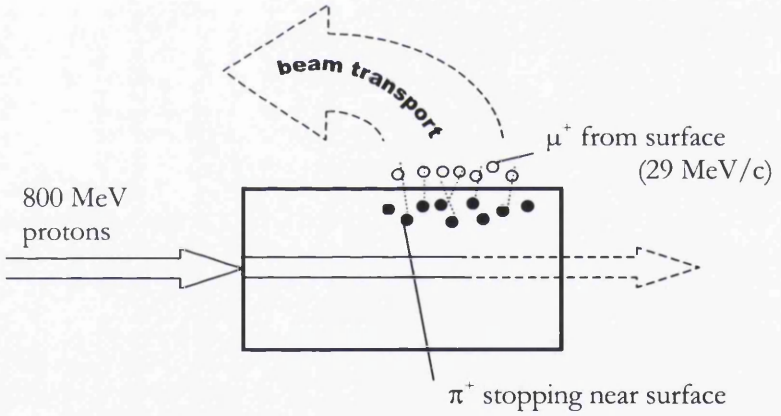

Figure 1.3.a. *Schematic of the European Muon Facility at ISIS (Courtesy of ISIS). This shows the beam line components for delivering muons to the three experimental areas; DEVA, MuSR and EMU. They consist of various steering and focusing magnets and electrostatic devices (a 'kicker' is used to 'kick' parts of the beam into different areas, while a 'separator' is used to filter particles by momentum and may also be used to rotate the muon spin).* b. *Detail schematic of the muon production target. Since ISIS is primarily a neutron facility, the integrity of the proton beam must be maintained after passing through the muon production target.*

1.3 Muon Decay

The subsequent decay of the muon is a three-body process:

$$\mu^+ \rightarrow \bar{\nu}_\mu + \nu_e + e^+. \tag{1.3}$$

Thus, the positron may be emitted within a continuous energy range, with the maximum given by

$$m_\mu c^2 = \sqrt{p_e^2 c^2 + m_e^2 c^4} + p_e c \quad \Rightarrow \quad E_{MAX} = \frac{m_\mu^2 - m_e^2}{2\, m_\mu} = 52.83 \text{ MeV}, \tag{1.4}$$

occurring when both neutrinos travel in a direction opposite to the positron, shown schematically in Figure 1.4.

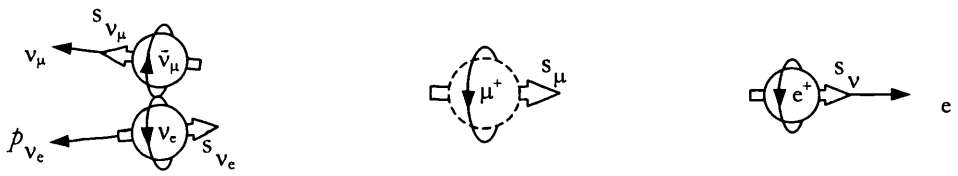

Figure 1.4. *Conservation of momentum in the μ rest frame when both neutrinos have (almost) the same direction of propagation.*

The probability of positron emission in a certain direction within a particular energy range can be calculated by integrating over the neutrinos' momenta [1.17].

If P is the muon polarisation, which is unity for a surface beam, and energy is in units of the maximum energy, $\varepsilon = E/E_{MAX}$, then positrons are emitted with an energy spectrum

$$W(\varepsilon) \propto \varepsilon^2(3 - 2\varepsilon), \tag{1.5}$$

and with an energy dependent asymmetry of

$$A(\varepsilon) = \frac{2\varepsilon - 1}{3 - 2\varepsilon} \cdot P. \tag{1.6}$$

The effective asymmetry is therefore obtained by integrating over all detectable positron energies. For example, when there are no limits on the efficiency of positron detection, the asymmetry averages to

$$a_0 = \frac{\int_0^1 W(\varepsilon')A(\varepsilon')d\varepsilon'}{\int_0^1 W(\varepsilon')d\varepsilon'} = \frac{1}{3}. \qquad (1.7)$$

Figure 1.5 shows the value, $a_0(\varepsilon)$, of a_0 when ε is the lower integral limit in equation (1.7). It is notable that cutting out lower energy positrons can increase the asymmetry, but the trade-off is count rate.

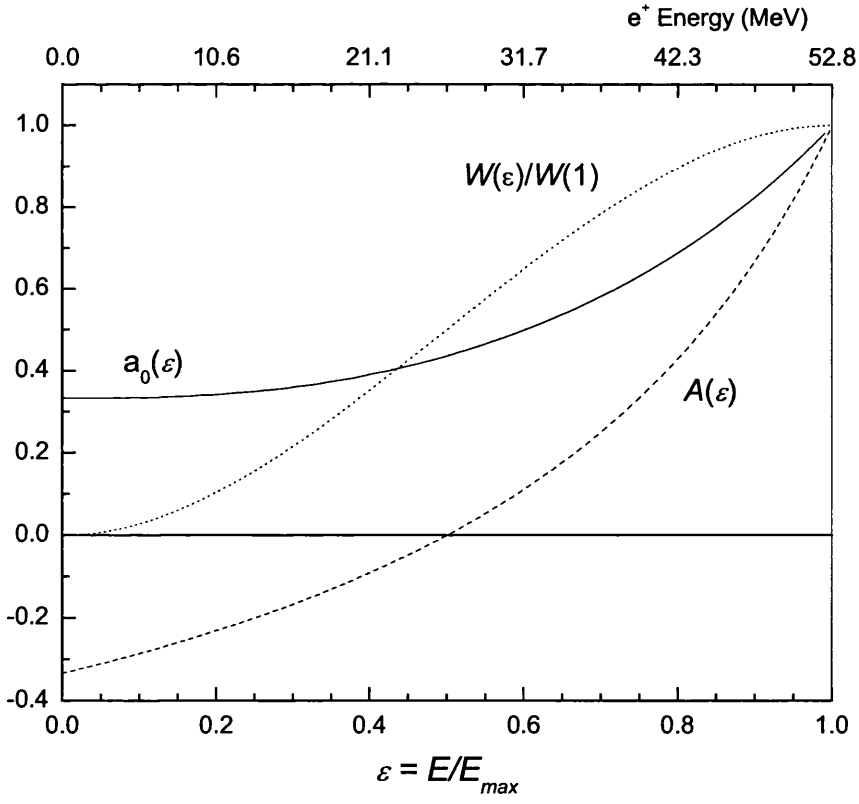

Figure 1.5. *Relative number $W(\varepsilon)/W(1)$ and asymmetry $A(\varepsilon)$ versus energy of the decay positrons.* $a_0(\varepsilon)$ *is the asymmetry given by evaluating the integral in equation (1.7) between* ε *and 1 (i.e. cutting out positrons with energy* $< \varepsilon$*).*

The positron emission cross-section then takes the form

$$\frac{dN_{e^+}}{d\theta} \approx 1 + a_0 \cos\theta . \qquad (1.8)$$

For $a_0 = 1$ a polar plot of the positron distribution is a perfect cardioid, but is reduced at more realistic values; as illustrated in Figure 1.6 for additional values of 0 and 1/3.

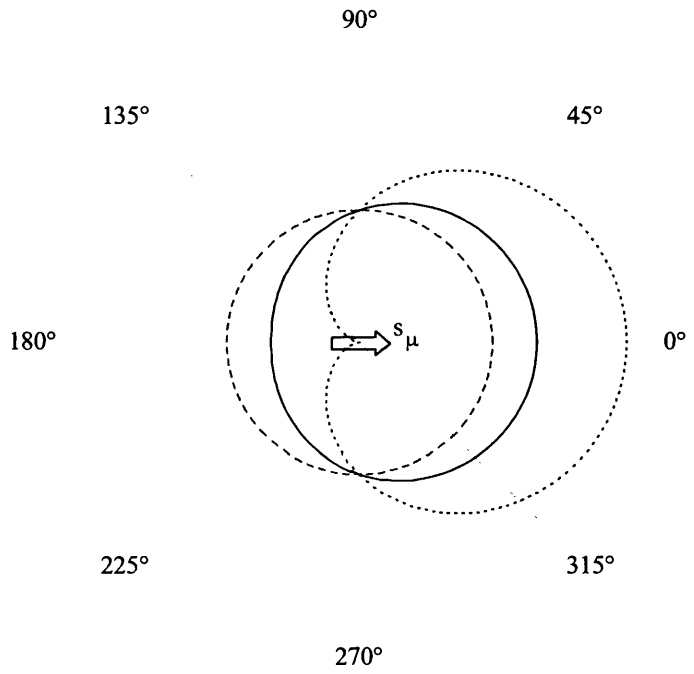

Figure 1.6. *Polar plot of the positron distribution for varying asymmetry parameter; 1 - fully polarised (dotted line); 1/3 - average (solid line); 0 - fully relaxed (dashed line)*

In practice the maximum measurable asymmetry is further reduced to ~25%, due to the finite solid angle of detection.

1.4 Spectrometers and Detection

We have shown that it is the intervention of parity non-conservation in both the production and decay of the muon that allows us to gain information on the muons spin direction. Gathering this information relies on detection of the emitted positrons.

Most experimental set-ups are adaptations of a simple geometry that places plastic scintillators, acting as positron counters, around the sample in the forward and backward directions with respect to the incoming muon spin, conventionally taken as the $\hat{z}$ direction, Figure 1.7.a.

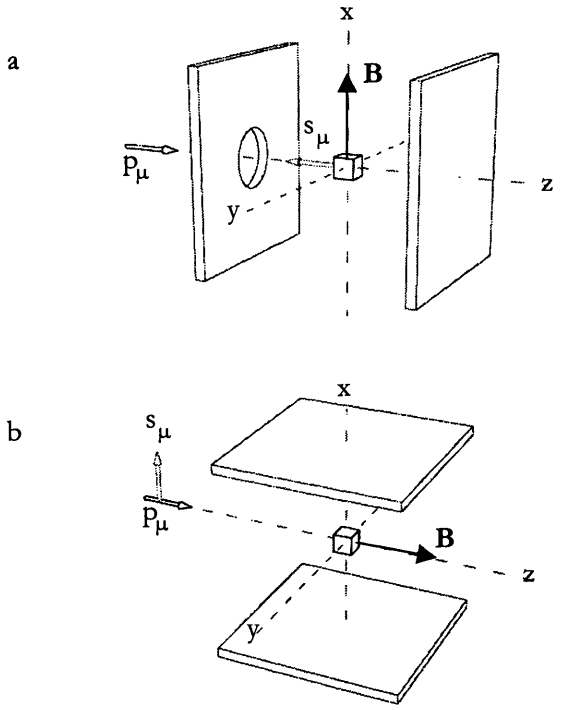

Figure 1.7.a. *Conventional transverse field detector arrangement.* b. *Alternative arrangement used for high transverse fields. In this case the spin has been rotated and the detectors are in the 'up' and 'down' directions.*

The positron count rate, measured at time t, in a detector at an angle θ to the initial spin direction of the muon ensemble, is given in general by

$$N_{e^+}(t) = N_0 \exp\left(-t/\tau_\mu\right) \left[1 + a_0 G(t) \cos\left(\theta + \omega t\right)\right] + B(t), \qquad (1.9)$$

in which N_0 is the initial count rate, which decays exponentially with the muon half-life, $\ln(2)\tau_\mu$. The expression in square brackets is the positron distribution, equation (1.8), taking into account evolution of the muon spin; ω (= γB) is the Larmor frequency of the muon in the case of an applied magnetic field with transverse component; $G(t)$ is a time-dependent relaxation function acting on the polarisation P ($\propto a_0$) – the form of which depends on the mechanism involved, and is often the subject of investigation. $B(t)$ is the time-dependent background – usually approximated to a constant value, B.

For forward and backward detectors, with count rates assigned as N^F and N^B respectively, the asymmetry is recovered from the normalised difference between the two,

$$A(t) = \frac{N^F(t) - \alpha N^B(t)}{N^F(t) + \alpha N^B(t)}, \tag{1.10}$$

where α ($= N_0^F / N_0^B$) is a parameter accounting for small differences in detection efficiency or geometry and is usually close to unity[§]. Equation (1.10) is then the 'corrected asymmetry'[**], although in a more complete analysis a β parameter may also be introduced to account for differences in maximum attainable detector asymmetry.

When background is negligible, i.e. $B^F + \alpha B^B << N_0^F e^{-t/\tau_\mu}$ (superscripts again denote forward and backward events), true at short times, this asymmetry becomes simply

$$A(t) = a_0 G(t) \cos(\theta + \omega t). \tag{1.11}$$

That is, it contains information on initial muon asymmetry and subsequent relaxation, as well as the initial phase and any frequency information. These data can be examined 'on line' using the various experimental facilities' muon data analysis packages.

---

§ A significant deviation from this value usually indicates a severe shift in the centre of gravity of the muon ensemble or a detector failure.

** All of the asymmetry data presented in this work have been subject to an α correction during analysis.

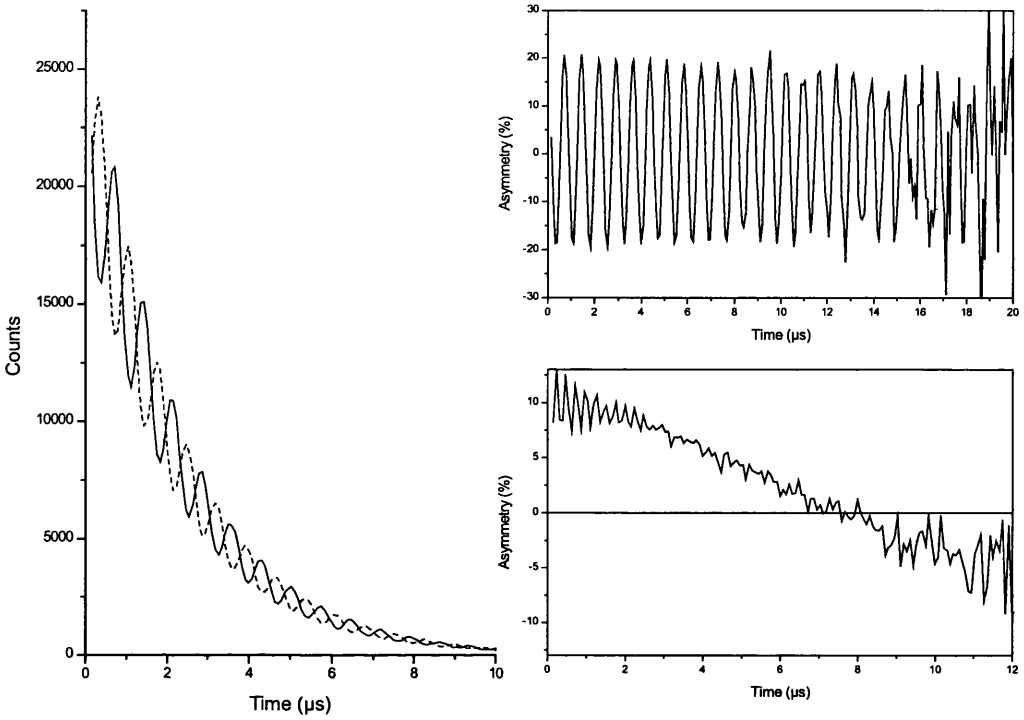

Figure 1.8. a. *Typical Transverse Field histograms – solid and dashed lines show the F and B histograms respectively, already adjusted by an α parameter.* b. *Typical asymmetry taken at 100 G. One can clearly see the precession of the diamagnetic muon – the envelope indicates almost full asymmetry and very slow relaxation.* c. *2-component signal taken at 2 G. This shows a fast relaxing paramagnetic muonium precession signal (gone after 3 μs!) superimposed on the much slower oscillation of the diamagnetic muon component. Example raw data from the Cab-O-Sil® study (chapter 3).*

1.4.1 μSR in Transverse Fields (TFμSR)

In the presence of a transverse magnetic field (***B*** normal to $\hat{z}$ direction in Figure 1.7.a), the muon ensemble undergoes spin precession at the Larmor frequency, $\omega = \gamma B$. γ is the gyromagnetic ratio and its value is given in Table 1.1. In this case histograms of the positron count rates, equation (1.9), take the form illustrated in Figure 1.8.a. Application of equation (1.10) then leads to asymmetry plots of the form shown in Figure 1.8.b & c. Since the frequency spectrum of the muon ensemble correlates exactly with the field at the muon sites, information on the field distribution is readily available. Figure 1.8.b shows the case in which all muons experience essentially the same

field, and precess at the same frequency with little or no dephasing. In other cases, where a distribution of fields gives rise to dephasing of the muon ensemble polarisation, the exact shape of the relaxation 'envelope' (most commonly *Gaussian* or *Lorenzian*) can give a clue to the magnetic environment.

At the *static* limit, the influence of an isotropic Gaussian distribution of static fields leads to the Gaussian form for the relaxation function

$$G(t) = \exp\left(-\frac{1}{2}\sigma^2 t^2\right), \tag{1.12}$$

where $\sigma^2 = \gamma^2 < B_\mu^2 >$.

With increasing temperature, the muon may begin to move and to sample more of the field distribution. In such cases the distribution of the mean field sampled by each muon in the ensemble is reduced, with consequent reduction of the relaxation rate, in a regime known as *motional narrowing* (as in the analogous case of NMR, there is a narrowing of the linewidth of the Fourier spectrum). Capture of the muon into potential wells reverses this effect, producing distinctive 'trapping' peaks in the relaxation rate.

At the *dynamic* limit, i.e. the fluctuation of local moments or thermally activated hopping of the muon with very short correlation time τ_C, so that $\tau_C \sigma << 1$, the relaxation function tends to the Lorenzian, or exponential, form

$$G(t) = \exp\left(-\sigma^2 \tau_C t\right). \tag{1.13}$$

In addition to relaxation, the distinct frequency bands encountered indicate the muon 'state'. Figure 1.8.c is a fine example of a very slowly precessing muon signal, due to muons in the diamagnetic state (½ revolution in 12 μs), with a much higher frequency superimposed at early times. This second signal is due to muonium (Mu), the bound state of μ^+ and e^- (see § 1.6), which has a frequency approximately 103 times that of the bare μ^+ due to coupling with the much larger electron magnetic moment. In the case shown here,

the muonium signal is strongly relaxed.

The binding of a muon to a molecular radical site can lead to yet higher precession frequencies. To account for the case of several states existing with different frequencies, equation (1.9) can be further generalised to a superposition of all states.

Due to the requirements of phase coherence of the muon ensemble in the TF signal, sensitivity to final states is limited to those that are reached in a fraction of the spin-precession period of the precursor.

1.4.2 μSR in Longitudinal Fields (LFμSR)

For Longitudinally oriented fields ($\boldsymbol{B}$ applied parallel to $\hat{z}$ direction in Figure 1.7.a) there is no precession and the frequency information is removed ($\omega = 0$ in equation (1.9)); and with it the spin-spin, or T_2, relaxation caused by dephasing. Instead asymmetry plots, such as in Figure 1.9, exhibit spin-lattice, or T_1, relaxation. Figure 1.9.b and c show the cases for a non-relaxing and strongly relaxing signal respectively. Although LF μSR loses much of the spectroscopic information available in the TF set-up, it is particularly sensitive to electronic activity and dynamics, and scanning the field is often used to probe for resonance conditions in coupled systems.

A time-integral (TI) counting method may be employed in longitudinal fields to complement time-differential (TD) counting. This has the advantage that time resolution is not required, so dead time in detectors or 'pile-up' in data acquisition (§ 1.5.1 & 1.5.2) is not a problem, and one can make full use of all available muons. Time integral methods are sensitive to structural information via resonance conditions, which are revealed by 'dips' in the field dependence of the time integrated muon spin polarisation.

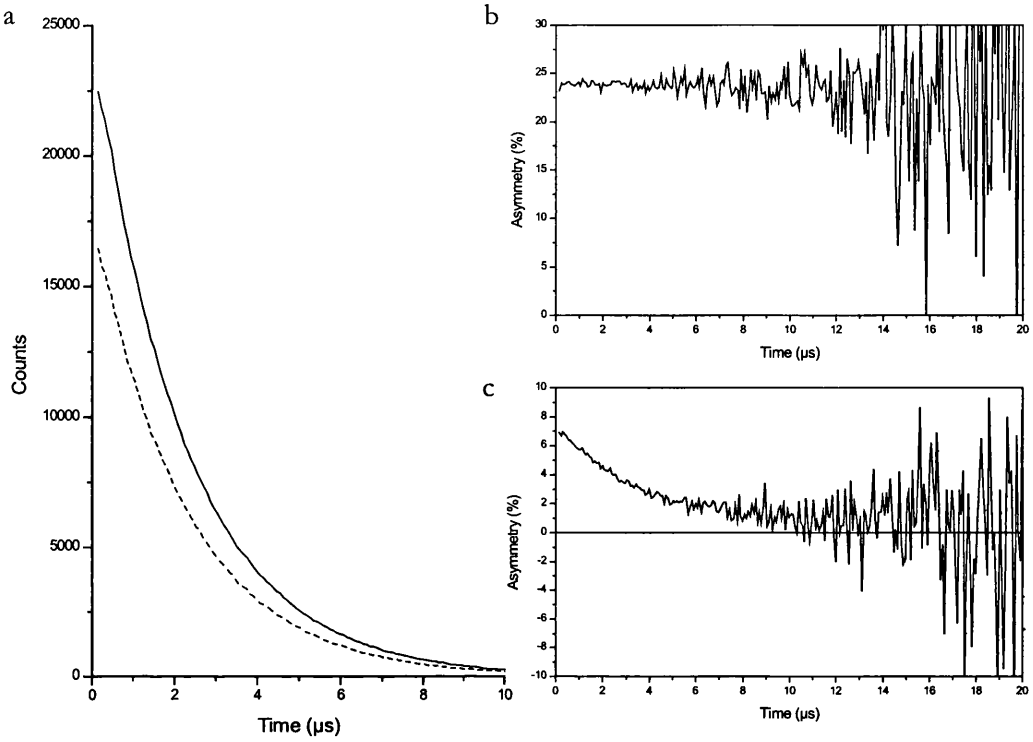

Figure 1.9. a. *Typical Longitudinal Field histograms - again both F and B histograms are shown.* b. *Full asymmetry spectra taken at 3 kG field, showing no relaxation.* c. *An example of a strongly relaxing signal taken at 2 G. The initial asymmetry indicates that this signal corresponds to only ~1/3 of the implanted muons. Example raw data from the Cab-O-Sil® study (chapter 3).*

Longitudinal fields may also be used to de-couple the μ^+ and e^- spins of muonium (§ 1.6). The nature of the *repolarisation curve* thus produced when asymmetry is plotted against field is strongly dependent on the muonium environment.

Zero Field μSR (ZFμSR) deserves a mention as the limiting case for LF μSR, although it plays no real part in the studies contained in this work. Zero field techniques (as their name suggests, no external field is applied) are used to study weak magnetism phenomena, μ^+-diffusion, spin glasses, etc. The form of the relaxation is well characterised and is very sensitive to motional effects.

1.5 Experimental Facilities and Sample Environments

There are several factors dictating the type of sample environments used for μSR experiments, considering jointly the nature of the probe and the subject of the investigation. Particle beam lines are naturally controlled under high vacuum for the purposes of beam optics and integrity, and although surface muon beams can traverse several metres of air at atmospheric pressure, it is essential to limit both beam width and momentum spread. For this reason, and for the controlled heating and cooling of samples, vacuum technology is a prerequisite for understanding and designing sample environments.

At the sample the muon beam intensity is centrally peaked with typical dimensions of around 10 mm FWHM, which prescribes sample sizes of this order. Smaller samples can lead to a significant reduction in count rate and can pose a problem with background from the immediate surroundings. Samples of low density also have limitations with regard to effectively stopping the muons within the sample (Chapter 3 explains the preparation of a very low density silica powder). To control the muons' position it is useful to understand the stopping power of materials acting on the beam in terms of surface density (= density × thickness) with units of mg cm^{-2}. By taking empirical values for the average range of the muons also in these units, one can estimate the range in any material by simply dividing this value by the material density. The muon is a bulk probe at conventional energies, with the effect that most solid samples can be placed directly in the path of the free beam, with little regard for surface quality but with due consideration for heat shielding of cryostats and ovens. Samples in other phases or forms often require containment in cells or packets, which must themselves have low surface density and, like the surrounding chambers, must conform to the strict criteria of limiting magnetic interference of this sensitive magnetic probe. The experiment on Hg in chapter 5 is an extreme example where care also had to be taken to select non-reactive materials and to contain the sample in solid and liquid phases.

The materials used for equipment must be compatible with the vacuum and must allow for the temperature and magnetic field to be varied accurately across a broad range of values. Stainless steel chambers are most common and where materials such as Cu must be used for more favourable thermal/electrical properties around a sample, masks of "ideal" materials (such as Ag[††]) or active collimators (particle detectors) are often used to remove spurious background signals.

For slow muon studies the effects of background events are more prominent and sample surface contamination also becomes an issue – Chapter 2 describes the additional requirements for muons at low energies (and low numbers) in terms of vacuum, chamber geometry and beam transportation.

These are all generic features within μSR facilities, regardless of the nature of the production and delivery of muons to the experimental areas, but the type of facility can have advantages for particular types of experiment. The work described in this thesis makes use of both a pulsed source, at the ISIS Muon Facility, part of the Rutherford Appleton Laboratory (RAL) in Oxfordshire, and a continuous 'DC' source at the Paul Scherrer Institute (PSI) in Villigen, Switzerland. Details of each facility are summarised below both as excellent examples of their kind and as a reference to the experimental environments used in this work. The main features are then collected in Table 1.2.

1.5.1 ISIS

The primary beam at ISIS consists of protons accelerated to 800 MeV in a 52 m diameter proton synchrotron. These are extracted in bursts with a repetition rate of 50 Hz, delivering 180–200 μA (~1.2×10^{15} protons s^{-1}). The bursts actually have a double pulse structure due to the extraction timing. Pions are produced by the protons passing through

[††] Ag is a well-characterised material producing negligible muon relaxation and is often used for apparatus calibration.

a 5, 7, or 10 mm Pyrolytic graphite slab at 45° to the incident beam, in turn creating muons with the proton pulse structure convoluted by the pion lifetime; each burst consists of two 80 ns FWHM pulses separated by 340 ns.

The first of these pulses is split by an electrostatic kicker, deflecting the muons into the DEVA and EMU areas (Figure 1.3.a) equally, providing each with a muon intensity of $\sim 10^5\ \mu^+\ s^{-1}$. The MuSR area receives the full second pulse. An **E**×**B** separator (Wien filter) reduces positron contamination (due to early decay of muons and pair production from π^0 decays) to $e^+/\mu^+ < 0.15$, which is further reduced by the kicker, optimised to deflect μ^+. After passing through all beam line windows, and taking into account beam line acceptance and the decay of sub-surface π^+, the momentum at the experimental areas is 26.5 MeV/c with a momentum byte $\Delta p/p$ of 10%. Muon polarisation is 100%.

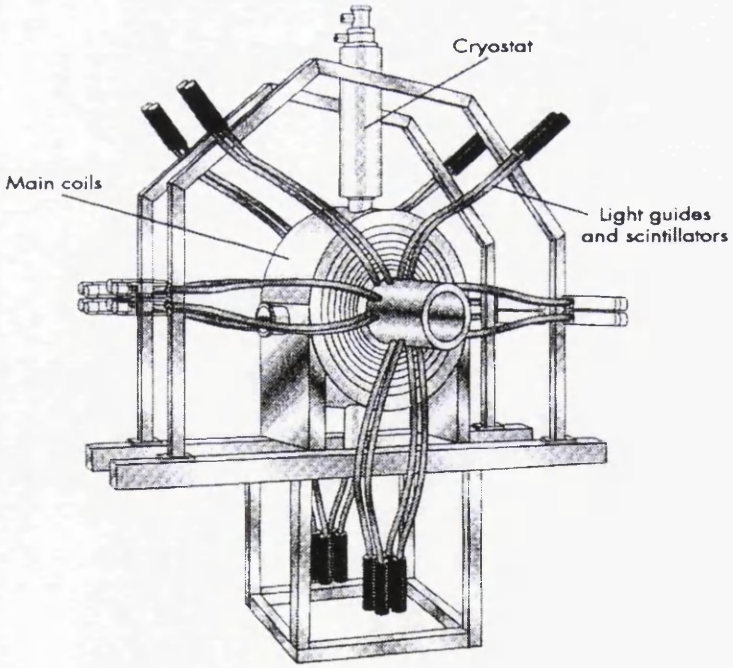

Figure 1.10. *Schematic drawing of the EMU spectrometer. This shows a typical detector geometry for a pulsed beam line, with segmented detectors in a cylindrical array connected to photomultiplier tubes (PMTs) via plastic light guides. (Courtesy of ISIS)*

EMU

EMU, Figure 1.10, is a μSR spectrometer optimised for ZF and LF measurements, supplying up to 4.5 kG LF (Helmholtz coils) and 0-100 G TF (calibration coils). The detectors consist of 32 scintillator segments grouped into 2 circular arrays, connected to time-to-digital converters (TDCs) with resolution settings of 8, 16, 24, or 32 ns. The instruments are controlled by a VAXstation 3200. Background in the histograms is constant at approximately 10^{-5} times the count-rate in the first bin.

After reaching the experimental area, traversing beam windows, the muons with a mean energy of 3.2 MeV have a range of ~ 110 mg cm^{-2}. The beam size at focus is 10 mm FWHM vertical and 10-27 mm FWHM horizontal – adjustable via collimating slits. Measurable precession frequencies are of the order 0.001-10 MHz.

1.5.2 PSI

The primary beam at PSI consists of protons accelerated to 590 MeV in a ring cyclotron. The accelerator frequency is 50 MHz and delivers a beam current of 1.6 mA DC (~ 10^{16} protons s^{-1}). These are guided to two targets, M (a 5 mm graphite target providing surface muons for the GPS area) and E (a 40 mm graphite target for surface muon and pion decay channels). Surface muons can be delivered to the areas with a maximum intensity of ~10^7 s^{-1}. Muon polarisation is >90%.

GPS

The General Purpose Spectrometer (GPS), Figure 1.11, is located on the πM3 beam line. Positron contamination can be reduced to a level of 1-2% by an electrostatic separator. The separator can also act to rotate the spin through an angle as large as 70° allowing both LF and TF measurements at all fields; with the main field parallel to the beam direction, 0-6 kG, and an auxiliary field perpendicular to the beam, 0-100 G. The detector consists of

a muon detector (for the start signal) plus five positron detectors in directions Forward, Backward, Up, Down and Right with respect to the muon beam. The time resolution is ~1 ns. Active collimators (i.e. veto scintillation counters in the backward direction, B_{veto}) can be used to match beam dimensions to the specimen, and there is also a veto counter for muons missing the sample, F_{veto}. Typically, the beam size at focus is ~ 5×5 mm^2 FWHM with the B_{veto}, but can be reduced as low as 1×1 mm^2 with external collimators.

A VAXstation 4000-90 controls data collection, and beam line components are controlled via an area PC. Background in a DC source is customarily a few orders of magnitude larger than that of pulsed sources, but extremely low background can be gained through PSIs' Muons-On-Request (MORE) set-up in which an electrostatic kicker is used to deflect muons individually into the area only when the previous muon has undergone decay.

The muons have a range of ~ 130 mg cm^{-2} after passing all beam line components. Measurable precession frequencies are of the order few kHz – 1 GHz (thanks to MORE).

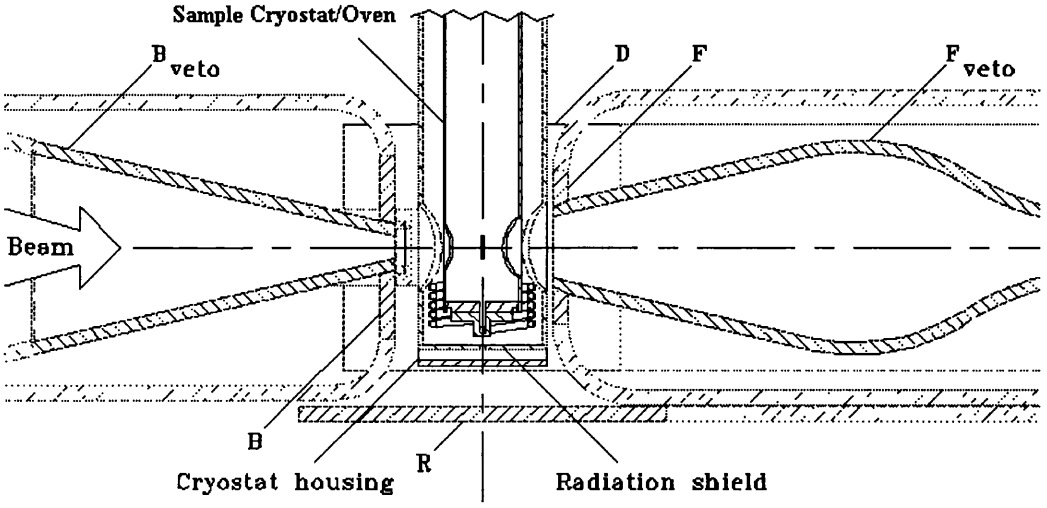

Figure 1.11. *Schematic cross-section drawing of the GPS spectrometer, viewed from above. This shows detailed configuration of the Forward (F) and Backward (B) and their respective 'veto' scintillators. The Right detector (R) is also shown, with the sample cryostat installed from the left. This particular use of veto counters and the fact that detectors require no segmentation at high rates is unique to continuous muon sources. (Courtesy of PSI).*

Table 1.2. Comparitive summary of Pulsed and DC muon sources.

Pulsed Sources	***DC Sources***
Maximum observable frequencies are limited to approximately the inverse of the muon pulse width (i.e. ~100 ns at ISIS gives a maximum of around 5-10 MHz).	The upper frequencies are governed by response of detectors and electronics (a few GHz are possible!).
Low relaxation frequencies of a few kHz are observable due to the long time window (>10 muon lifetimes).	Minimum frequencies are effectively governed by experimental time, since frequency is proportional to count rate (the arrival of a second muon before the decay of the first 'kills' both events through pile-up rejection). Typically >several kHz is the lower limit but this has been improved on GPS with the introduction of the 'MORE' fast kicker.
High rates introduce dead-time effects - which must be countered by using segmented detectors to make up solid angle.	The individual counting in DC reduces dead time problems.
Random background is small compared to muon counts but low background on small samples requires a special fly-past set up.	By using veto counters small samples can be studied easily.
Can be used in conjunction with other pulsed techniques, i.e. RF and lasers.	Laser/RF work requires a high duty cycle, leading to associated problems such as sample heating.

1.6 Muonium and Chemistry

The thermalisation of μ^+ within a solid involves various energy loss mechanisms, which occur within the order of 10^{-10} seconds (this is discussed in chapter 2 with an emphasis on low energy interactions). As mentioned previously the μ^+ may capture an e^- to form the paramagnetic[#] pseudo-atom Muonium (Mu). This was first noted in 1957 when Friedman and Telegdi [1.18] proposed the formation of "muonium" to account for the rapid depolarisation of roughly half of the muons within a nuclear emulsion. Orear *et al.* [1.19] later verified this by applying a large magnetic field to *quench* the hyperfine interaction; decoupling the spins and inhibiting this depolarisation. Possibly contrary to intuition, it turns out that the cross-section for this Mu formation is only significant at very low e^- concentrations – in cases of high conduction electron concentration, i.e. most metals, an effective screening potential is set up around the μ^+ preventing e^- capture.

Table 1.3. Muonium and the Mu/H analogy.

	H	Mu	Mu/H
Reduced mass, m_0	9.1044×10^{-31} kg	9.0564×10^{-31} kg	0.9957
Bohr radius $\frac{4\pi\varepsilon_0\hbar}{m_0e^2}$	0.529 Å	0.532 Å	1.0042
Ionisation energy	13.598 eV	13.539 eV	0.9957
$\Delta\nu_{HFS}$ (in vacuo)	1.4204057517667(9) GHz	4.46330288(11) GHz	3.1422
Mu spin precession:	$\tilde{\gamma}_{Mu} = \frac{\gamma_{Mu}}{2\pi} = \frac{(g_\mu\mu_{\mu^+} + g_e\mu_{e^-})}{2h}$ = -1.3960878 MHz G^{-1} *		

* The –ve sign indicates precession in the opposite sense to the bare muon (cf. Table 1.1).

Thanks to its similar reduced mass, the chemistry of Mu is effectively identical with that of hydrogen (see Table 1.3 for some comparisons). For this reason it is used as a tool by

On account of the unpaired electron.

which one may infer the nature of H states and dynamics, which we explicitly take advantage of in this work for the hot semiconductor (chapter 4) studies. One must remain aware, however, that zero-point energy is significant for the relatively light muons and muonium atoms, and its effect can be considerable in determining transitions as well as ground states.

1.6.1 Representation of the Spin-States.

In vacuum in the presence of an external magnetic field, the isotropic spin Hamiltonian for muonium is

$$H = A_\mu h\mathbf{S}\cdot\mathbf{I} - \tilde{\gamma}_e h\mathbf{S}\cdot\mathbf{B} - \tilde{\gamma}_\mu h\mathbf{I}\cdot\mathbf{B}. \qquad (1.14)$$

The second and third terms on the right are Zeeman terms for the electron and muon respectively; **S** and **I** are the respective spin operators for the electron and muon. The first term is the hyperfine interaction – the hyperfine constant (frequency) is defined as $A_\mu = \frac{8}{3}\mu_0\tilde{\gamma}_\mu\tilde{\gamma}_e|\psi(0)|^2 h$ and, as can be seen, is proportional to the unpaired electron density (the expectation value of the electron wavefunction) at the muon (nucleus); this term is also called the 'contact' hyperfine interaction.

The general solution of this Hamiltonian [1.20] gives the energy eigenvalues (Figure 1.12):

$$\frac{E_1}{h} = \frac{A_\mu}{4} - \frac{\tilde{\gamma}_e + \tilde{\gamma}_\mu}{2}B, \qquad (1.15)$$

$$\frac{E_2}{h} = -\frac{A_\mu}{4} + \frac{A_\mu}{2}\sqrt{1+x^2},$$

$$\frac{E_3}{h} = \frac{A_\mu}{4} + \frac{\tilde{\gamma}_e + \tilde{\gamma}_\mu}{2}B, \text{ and}$$

$$\frac{E_4}{h} = -\frac{A_\mu}{4} - \frac{A_\mu}{2}\sqrt{1+x^2},$$

where $x = -\frac{(\tilde{\gamma}_e - \tilde{\gamma}_\mu)}{A_\mu}B = \left(\frac{B}{B_0}\right)$ is a dimensionless parameter in units of the hyperfine field. The value of B_0 for Mu in vacuum is ~0.1583 T.

For completeness, the corresponding individual eigenfunctions, in terms of eigenstates $|m_e, m_\mu\rangle$, have the form

$$\psi_1 = |+,+\rangle, \tag{1.16}$$

$$\psi_2 = s|+,-\rangle + c|-,+\rangle,$$

$$\psi_3 = |-,-\rangle, \text{ and}$$

$$\psi_4 = c|+,-\rangle + s|-,+\rangle,$$

where "+" and "–" are conventionally used to indicate $m_e, m_\mu = +½$ and $–½$ respectively.

The amplitudes for the mixed states of eigenfunctions ψ_2 and ψ_4, are

$$\text{(sine) } s = \frac{1}{\sqrt{2}}\left(1 - \frac{x}{\sqrt{1+x^2}}\right)^{\frac{1}{2}} \text{ and (cosine) } c = \frac{1}{\sqrt{2}}\left(1 + \frac{x}{\sqrt{1+x^2}}\right)^{\frac{1}{2}}, \tag{1.17}$$

and the initial populations of the four hyperfine states (assuming no electron polarisation) are given by the probabilities [1.21]:

$$P_1 = \frac{1}{2} \;;\; P_2 = \frac{s^2}{2} \;;\; P_3 = 0 \;;\; P_4 = \frac{c^2}{2}. \tag{1.18}$$

The energies of the four possible spin states of the two-spin-½ Mu system, comprised of a triplet (total spin $F = 1$) and singlet ($F = 0$), are often plotted against magnetic field in a Breit-Rabi diagram, such as Figure 1.12. The Breit-Rabi diagram is a common reference point for an intuitive understanding of many aspects of muonium spectroscopy, and it is particularly valuable when extended to more complex systems by including additional environmental factors in the Hamiltonian.

In the case of isotropic muonium, with a magnetic field applied along the z-axis, the time-dependent muon spin polarisation may be calculated using a density matrix approach [1.22]

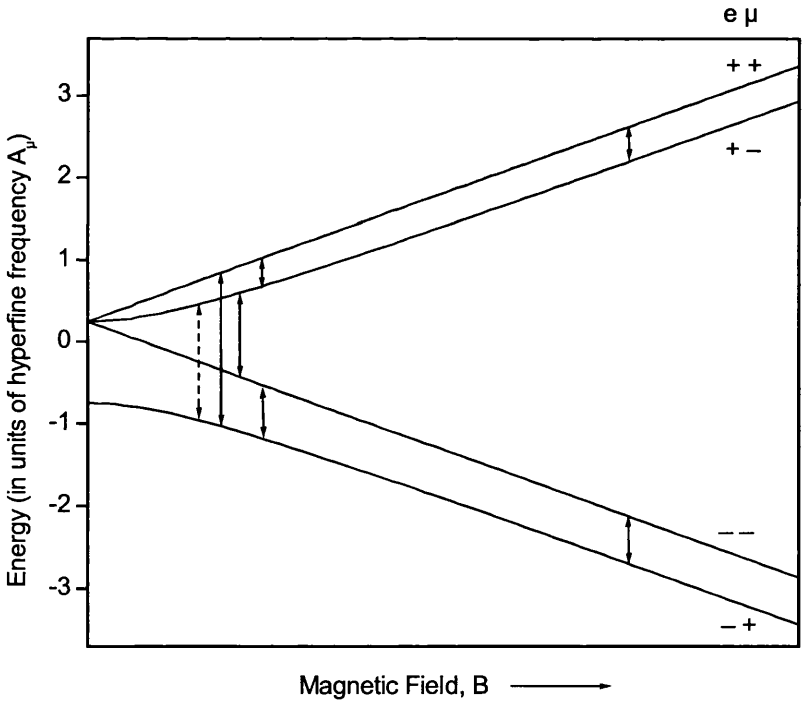

Figure 1.12. *The Breit-Rabi diagram, developed originally for atomic hydrogen, provides a clear representation of the energy eigenvalues for multiple spin systems as a function of magnetic field. Here it shows the hyperfine and Zeeman splitting for ground state ($1S_{½}$) muonium in vacuum. Eigenstates are indicated on the right by the respective sign of the electron and muon spin (i.e. positive for spin ↑ and negative for spin ↓). Solid and dashed arrows indicate prominent transitions between the states in TF and LF respectively.*

to give

$$P_z(t) = \frac{1+2x^2}{2(1+x^2)} + \frac{1}{2(1+x^2)}\cos(\omega_{24}t), \quad (1.19)$$

in a LF experiment, and

$$P_x(t) = \frac{1}{2}\left(c^2\cos(\omega_{12}t) + s^2\cos(\omega_{23}t) + c^2\cos(\omega_{34}t) + s^2\cos(\omega_{14}t)\right) \quad (1.20)$$

in a TF experiment. We define

$$\omega_{ij} = \frac{E_i - E_j}{\hbar} = 2\pi\nu_{ij} \quad (1.21)$$

as the transition frequency between states $|i\rangle$ and $|j\rangle$. The amplitudes of the transitions are generated from the squares of the expectation values of the Pauli spin operators [1.23]:

$$|\langle i|\hat{\sigma}_z|j\rangle|^2 \qquad \text{for LF, and}$$

$$|\langle i|\hat{\sigma}_x|j\rangle|^2 \qquad \text{for TF.} \quad (1.22)$$

In the general case, at low transverse fields the separation of energy levels leads to the four $\Delta M = \pm 1$ transitions; $|1\rangle \leftrightarrow |2\rangle$, $|2\rangle \leftrightarrow |3\rangle$, $|3\rangle \leftrightarrow |4\rangle$ and $|4\rangle \leftrightarrow |1\rangle$, shown in Figure 1.12. However, in a solid with no electron polarisation (i.e. equal proportions spin-up $\uparrow$ and spin-down $\downarrow$ w.r.t. μ^+ spin direction) the fully polarised nature of the incoming μ^+ beam means that ½ of the Mu ensemble forms in the polarised *ortho*-muonium state $|m_e, m_\mu\rangle = |++\rangle = |1\rangle$, and the other half forms in the mixed *para*-muonium state $|m_e, m_\mu\rangle = |-+\rangle = s\,|2\rangle + c\,|4\rangle$. Para-muonium is immediately depolarised by phase oscillations between triplet and singlet states at frequencies (ν_{34} and ν_{14}) of the order of the

hyperfine structure interval, A_μ, and cannot therefore be 'seen'. Precession signals with frequencies ν_{12} and ν_{23} only are visible, together accounting for half the muonium polarisation. The amplitude of the muonium asymmetry signal detected in a typical TFμSR experiment therefore represents only half of the true *muonium fraction*[§§].

At the high field limit, within the Paschen-Back régime, the Zeeman terms dominate the hyperfine term in equation (1.14). The electron and muon spins are then fully decoupled and the muon feels an effective magnetic field, equal to the applied field plus or minus half of the so-called hyperfine field (according to whether the electron is spin ↑ or spin ↓). As equations (1.17) and (1.20) imply, only transitions $|1\rangle \leftrightarrow |2\rangle$ and $|3\rangle \leftrightarrow |4\rangle$ are left with significant intensity, and to first order have frequencies $\nu_{12} = \tilde{\gamma}_\mu B - A_\mu/2$ and $\nu_{34} = \tilde{\gamma}_\mu B + A_\mu/2$. Measurement of the vacuum hyperfine frequency A_μ was first performed indirectly by measuring these two transitions, before more sensitive techniques were developed to resolve the frequency directly in zero field [1.24].

In low longitudinal fields only the $\Delta M = 0$ transition, $|2\rangle \leftrightarrow |4\rangle$, is allowed, where $\nu_{24} = A_\mu\sqrt{1+x^2}$. It is also the only non-zero frequency transition at zero field. As ν_{24} is $\geq A_\mu$ it cannot be detected in a typical LFμSR experiment, and $\cos(\omega_{24}t)$ averages to zero. In high longitudinal fields the amplitude of this transition becomes negligible, as can be seen from equation (1.19), and $P_z(t) \rightarrow 1$. A plot of the initial asymmetry vs. field is known as a repolarisation (or decoupling)[***] curve and is described by the time-independent term in equation (1.19). More generally, for a system containing both a fraction f_d of diamagnetic muons and a fraction f_{Mu} (= $1-f_d$) of isotropic muonium, the repolarisation curve is defined by

§§ The fraction of incident muons forming Mu (often expressed as a percentage).
*** Polarisation is 'recovered' at high longitudinal fields as the electron and muon spins are decoupled.

$$P_z(0) = f_d + f_{Mu}\left(\frac{1+2x^2}{2(1+x^2)}\right). \tag{1.23}$$

Some typical repolarisation curves are plotted in Figure 1.13 for diamagnetic fractions $f_d = 0$ and ½. Phenomena such as spin-exchange, chemical reactions and anisotropy have characteristic effects on the form of the repolarisation, and will be dealt with further for the systems studied in chapter 3, where anisotropy in particular is introduced by the interaction of the muons with the surface of fine powder samples.

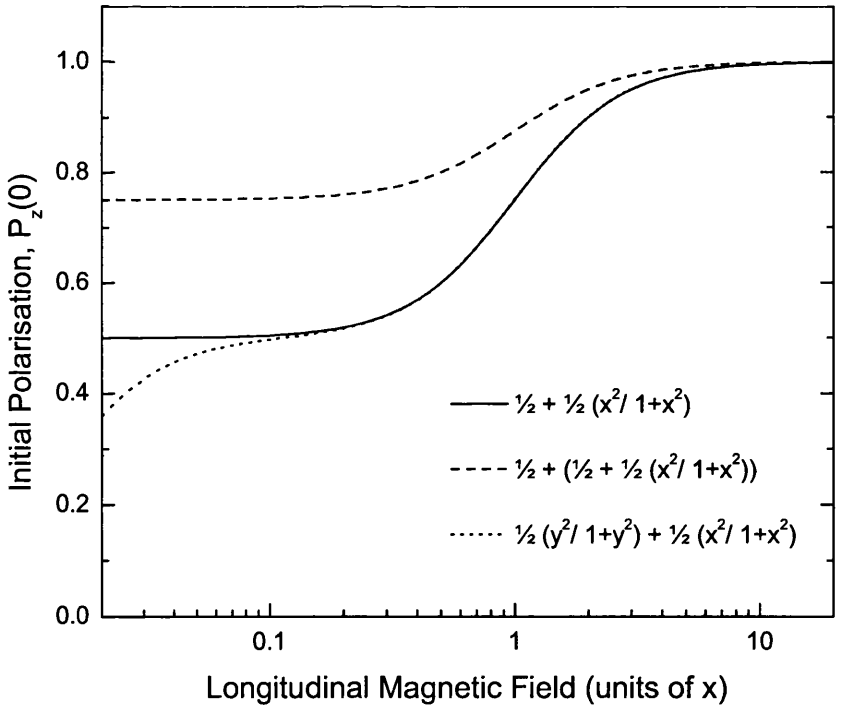

Figure 1.13. *Repolarisation curve for systems containing muonium. The solid and dashed lines represent a diamagnetic fraction f_d of 0 and ½ respectively. The dotted line indicates a modification to the f_d = 0 case which is characteristic of anisotropy in the hyperfine interaction which is decoupled at a significantly lower field. For this example* y *is simply set to 80*x.

1.7 Overview

This is by no means an exhaustive account of the techniques of μSR, instead it is intended as a guide to the fundamental features that make the muon such a unique and interesting probe. Each of the following chapters deal with a particular system separately, and all will draw heavily on the vocabulary that has been outlined here.

For the work on slow muons there will be an emphasis on muon beam technology and adaptations required to account for the nature of the particle at low energy. We will examine the phenomenon of muonium formation in more detail, and the techniques of TF μSR will also be applied to the observations of muons in thin films, where determination of relative fractions of Mu and μ^+ is the key to realising the implantation profile.

The process of muonium formation is also studied in silica powder systems, this time with both TF and LF techniques being applied to elucidate dynamic processes occurring at the surface of the powder in the presence of various quantities of adsorbed noble gases.

The following chapter on silicon at high temperature will take advantage of Mu as a hydrogen analogue to examine the state and dynamics of H in these materials with the benefit of the muons' sensitivity. For Si at high temperatures we examine in particular the effects of charge exchange from two perspectives; attempting to correlate TF frequency information with LF, $1/T_1$, relaxation data. LF relaxation is then investigated in semimetal systems, as we extend our understanding of these effects to materials with small or zero band gap.

2 SLOW MUONS

2.1 Why Slow Muons?

Until recently the energies at which muons are produced meant that μSR has been simply a bulk probe*. Building on tests in the late 1980's however, the latter part of the 1990's has seen moves toward moderating the existing beams to lower energies and thus making the techniques accessible to thin films, surfaces and interfaces (multilayers), and nanomaterials [2.1]; it has also been observed that a slow muon beam of sufficient intensity could be re-accelerated to take advantage of the much improved phase space characteristics for low background on small samples [2.2]. So a high intensity, low energy muon beam is desirable from many aspects. The main difficulties lie in the short lifetime of the muon and the relatively poor phase-space characteristics resulting from their production, which limit 'cooling' methods to those that act quickly and randomly with consequent low efficiency.

This chapter centres round an internationally collaborative project for the development of a slow muon beam at the ISIS facility (RAL), through a method of moderation using frozen gas moderators. This beam is unique in that it is the first of its kind commissioned at a pulsed source, where the inherent timing signal overrides the need for a beam counter beyond the production target (as in a DC beam), and the fine energy resolution of the low energy muons at the production target (§ 2.4.6) is maintained. The method is detailed and evaluated with reference to competitive methods, and with regard to results achieved by early 1999. This is followed by preparative work towards the transformation of such a developmental beam into a user facility through the addition of dedicated sample handling apparatus developed at University College London (UCL).

* Current surface beams (>3 MeV) have ranges of ~100 mg/cm^2; i.e. 100 μm in Ag or 1 mm in water.

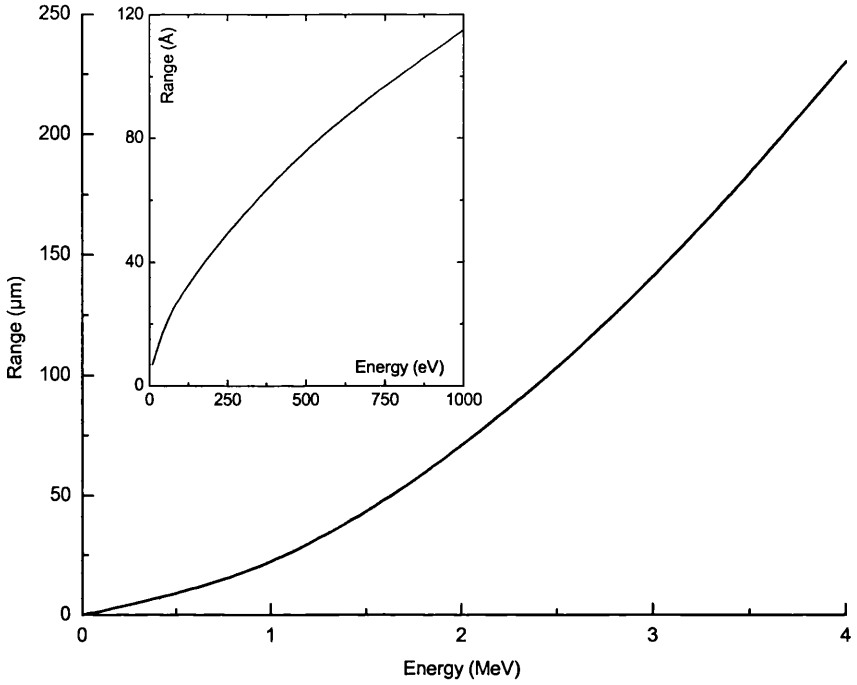

Figure 2.1. *Muon ranges in silver – obtained from the Monte Carlo simulation package SRIM-2000 [2.3]. Inset shows detail at low energies.*

2.2 Slowing Down of Muons

Figure 2.1 illustrates the average ranges (via simulation) of muons for a given energy in Ag. The inset shows that energies below a few keV are required for films of a few hundred angstroms, and significantly lower energies are needed to probe the first few monolayers of a sample†. Slowing muons down to these kind of energies through the application of techniques such as phase space cooling, frictional cooling, anticyclotron traps, degraders, rare gas moderation and ionisation of thermal muonium have all been discussed elsewhere [2.5, 2.6, 2.7], but in practice only the latter two methods are currently viable options; both methods beget a similar slow muon production efficiency, and although laser ionisation of muonium may have arguably more potential for improvement [2.8], rare gas moderation boasts relative technical simplicity and reliability.

† Some inconsistencies with SRIM simulation of muons below several tens of keV have been noted [2.4]. However, our results for implantation profiles (§ 2.5.1) prove SRIM guilty only of minor overestimation.

The rare gas moderation technique is not only applicable to noble gases, indeed other *cryosolids*[‡] have also been studied in the course of this work. Noble gases have simply shown the best results to date in terms of moderation efficiency. The technique involves condensation of the gas on the downstream side of a substrate/degrader (typically a metal foil) at cryogenic temperatures. Muons lose energy in the substrate mainly as a result of inelastic excitation and ionisation processes. These lower energy muons, normally distributed about a range characteristic of the material, may then act as a *source* for producing epithermal μ^+ (i.e. muons with energies in the range of a several tens of eV – defined also as 'very slow'[§] muons). The substrate is designed to have the peak of the muon stopping profile at its downstream surface where the muons enter the gas layer (which, for Al substrates, means a foil of a few hundred μm thickness; see Figure 2.2 and Figure 2.5). This maximises the number of muons within an energy range that can be reduced to epithermal energies by the rare gas solid (RGS).

For RGS films of order 0.1 μm thick, it is clear from Figure 2.2 that most of the original surface muons are either stopped within the Al substrate or continue into the system beyond the RGS layer. This is the first indication of the low moderation efficiency that is an inevitability of such techniques. The number of *source* muons is a very small fraction; at the downstream surface of the degrader, transmitted muons have a broad peak in their energy distribution with only a very low intensity below several tens of keV (Figure 2.3) – a consequence of the stochastic processes involved. Attempting to exploit additional muons from around the peak of the stopping profile, tests were performed on the application of several consecutive substrates in a Venetian-blind-like array, but effective extraction of moderated muons from the 'inner' surfaces proved to be impracticable [2.9]. To date there has been no significant development in either substrate geometry or material that has

‡ Weakly bound solids that condense only at very low temperatures.

§ The term '*very* slow' is appropriate to epithermal energies; in contrast to 'slow' muons, defined as having energies of several keV, but which we use here as a generic term for low energy.

managed to shift the transmitted muon energy distribution towards lower energies.

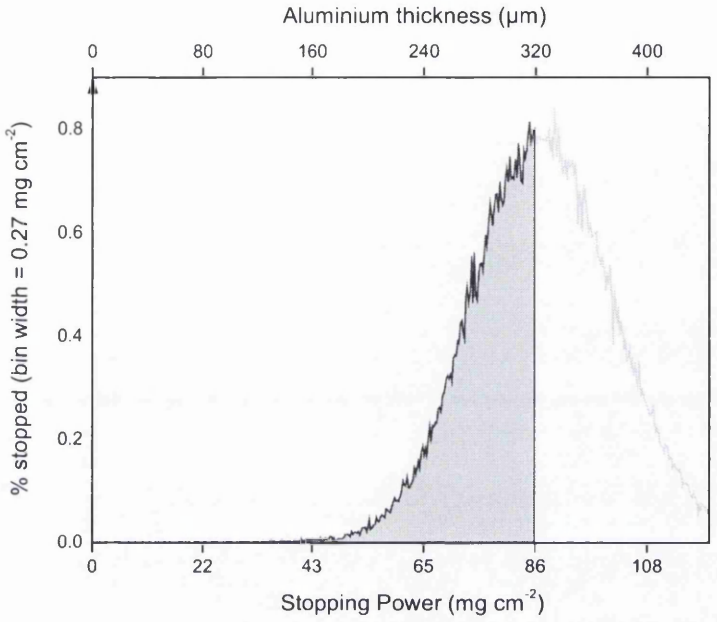

Figure 2.2. *Approximate stopping profile for μ^+ within the moderator (obtained from SRIM-2000, based on 10^5 particles). The equivalent depth in Al is also indicated. 86 mg cm^{-2} corresponds to the thickness (320 μm) chosen for the moderator in this study, based on such simulations.*

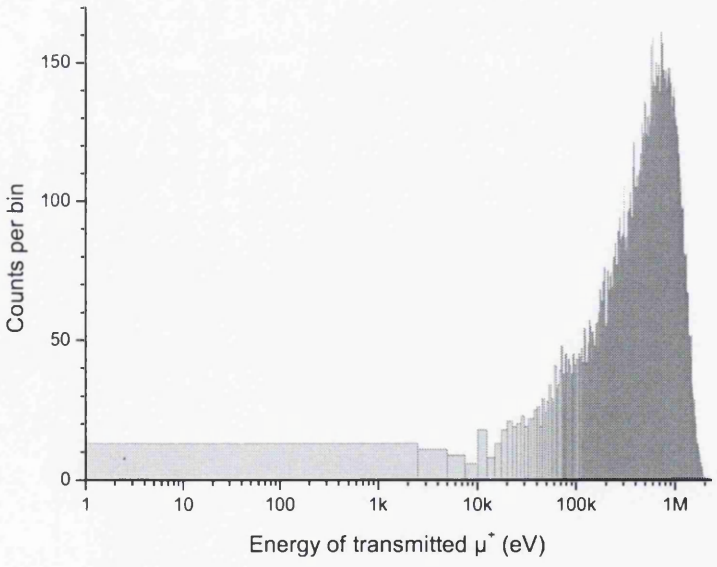

Figure 2.3. *Energy distribution for μ^+ transmitted through a 320 μm Al moderator (obtained from SRIM-2000, based on 10^5 particles). Note the bin size of 2.5 keV; the number in the first bin corresponds to 10^{-4} of the incident muons.*

The application of frozen inert gases was first successfully used in *positron* moderation experiments in the mid 1980's [2.10], and much empirical evidence has been gained in this area since that time as radioisotopes provide an abundant bench-top source for e^+ beams. For the noble gases, values of the positron moderation efficiency ε_{e^+} $\left(= N_{\text{slow}}^{\text{out}} / N_{\text{fast}}^{\text{in}}\right)$ achieved to date are around 10^{-3} to 10^{-2} [2.11]. The dynamics are usually described in terms of emission as a result of inefficient cooling below the positronium (Ps) formation threshold within these wide-band-gap insulators.

With due regard for the important mass differences (e.g. in dynamics, binding energies, etc.), these results have been used as guidance in the development of the analogous slow-μ^+ beams. Systematic increases in efficiency are entirely dependent on an understanding of the moderation processes and how they can be optimised but, despite much work aimed at understanding muon moderation and muonium formation in the last decade (see also chapter 3 of this work), there is yet little detailed unambiguous understanding of the muon emission process at low energies. Importantly, for the use of slow muons as a probe, the moderation has been shown to fully conserve initial polarisation [2.12], i.e. the muon undergoes no prompt relaxation within the moderation materials used and typical μSR techniques may still be applied at low energies (LE-μSR).

The experiments detailed in the following section were designed to provide more insight into these low energy processes through systematic studies of gas conditions whilst developing the ISIS slow μ^+ beam. We examine not only the part played by Mu formation and other processes as the muon velocity becomes comparable with that of the valence electrons and the Bethe-Bloch formula breaks down, but also look to how moderator growth conditions and operating environment are empirically chosen to maintain a dedicated slow muon beam line at optimal efficiency.

2.3 Construction of the Slow Muon Beam Line

The ISIS slow muon beam line is illustrated schematically in Figure 2.4.a & b. Developed by the Heidelberg group [2.7], this consisted of a stainless steel system pumped by two turbo molecular pumps (*Balzers*, TPU 450H) placed at the target and sample ends. Considering a general monolayer formation time of 1 sec at 10^{-6} mbar, ultra high vacuum (UHV) of about 10^{-10}-10^{-11} mbar was required to maintain integrity of both the condensed gas target, and the sample surface, on the experimental timescale. This was regularly achieved by baking out the chambers for up to three days at 180 °C after each breach of the vacuum. Vacuum measurements were made with a cold cathode ionisation gauge (*Balzers*, IKR 070) and a mass spectrometer residual gas analyser (*Leda-Mass*, Vacscan) was used for vacuum diagnostics during target preparation.

Beam line components upstream of the target were designed with regard to limiting range straggling and beam spot enlarging. Materials were chosen with low mean atomic charge number and were positioned as close as possible to the target; high energy μ^+ passed firstly through a rotatable Kapton® degrader (25 μm), which allowed depth adjustment of the peak of the stopping profile within the moderator target. This was followed by a scintillation beam counter (25 μm) for time-of-flight and slow muon efficiency calculations. A stainless steel window (48.7 μm) then separated the $\geq 10^{-6}$ mbar DEVA beam line vacuum (see § 1.5.1) from the UHV of the slow muon apparatus. Finally, the μ^+ passed through liquid N_2 and liquid He heat shields (13 μm each) before coming to rest at the downstream side of the moderator. The combined stopping power through all materials was 141(5) mg cm^{-2}.

The effect of these components on the primary beam is discussed fully by Träger [2.6]. The result was a beam-spot size of 32(3) × 22(2) mm^2 FWHM (H × V) based on the nominal DEVA beam dimensions of 27 × 10 mm^2 FWHM (H × V).

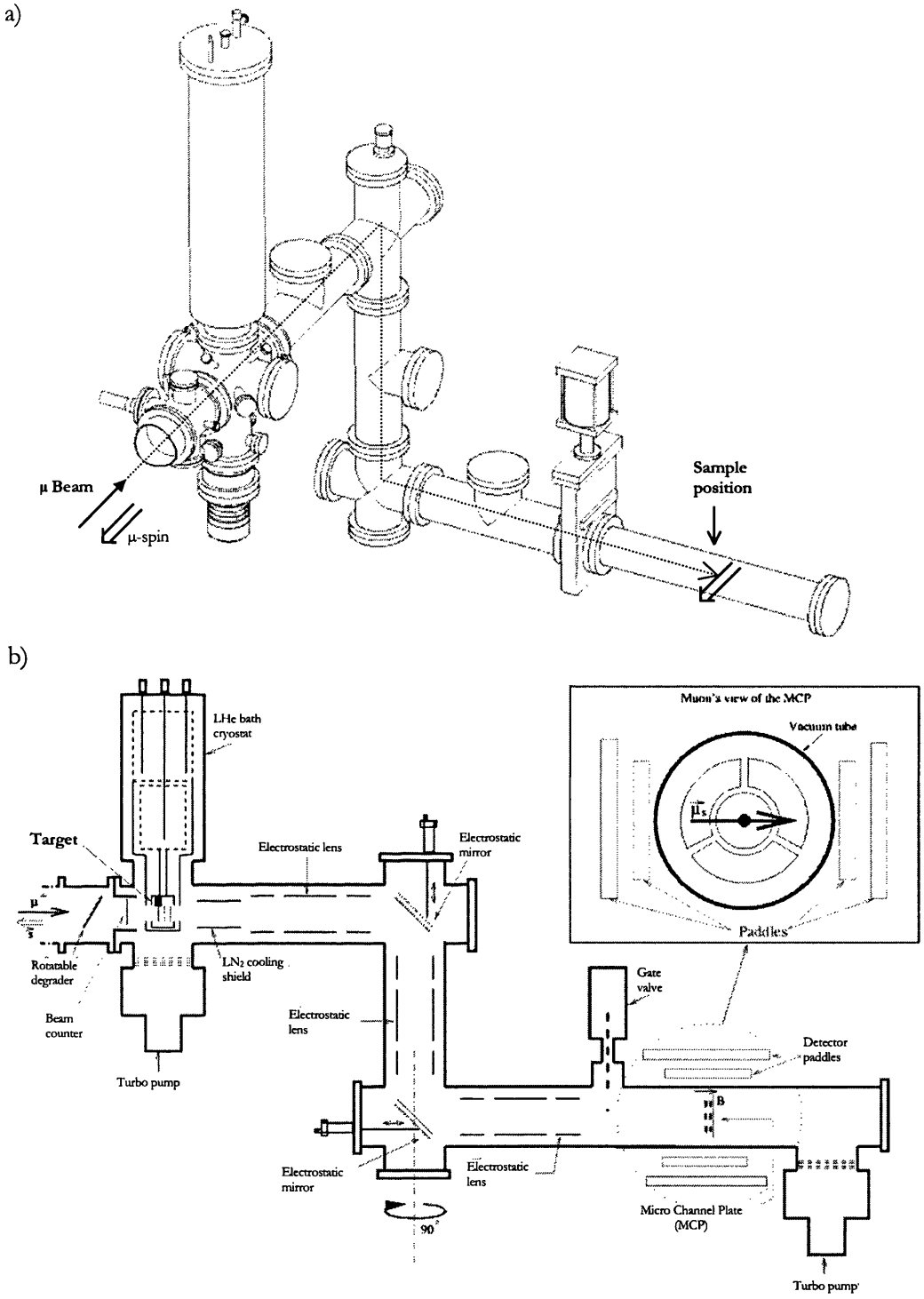

Figure 2.4.a. *A representation of the slow μ apparatus installed (1997-1998) at ISIS. The schematic,* b, *shows its function in a little more detail. The high-energy muons enter the apparatus from the left, passing through a beam counter before striking the moderation target. Moderated muons are then extracted and transported by means of electrostatic mirrors and lenses, before reaching the sample position, shown here as a Micro Channel Plate (MCP).*

2.3.1 Moderation Target

The target was mounted on a liquid He bath cryostat consisting of two 12-litre tanks for liquid He and liquid N_2. The 80 mm diameter circular cold finger was equipped with a silicon diode for temperature measurement and an electric heater for removal of the gas layer by evaporation/ sublimation. Attached to this was a substrate holder built of oxygen free copper (OFHC) to limit out-gassing and optimise heat conduction to the cryostat cold finger. A 3 mm sapphire plate was used to electrically insulate the substrate holder from the cold finger whilst maintaining good thermal conductivity. The 48 mm diameter substrate was an aluminium foil (thickness 320 μm, purity 99.999%), mounted to the copper holder with a stainless steel frame.

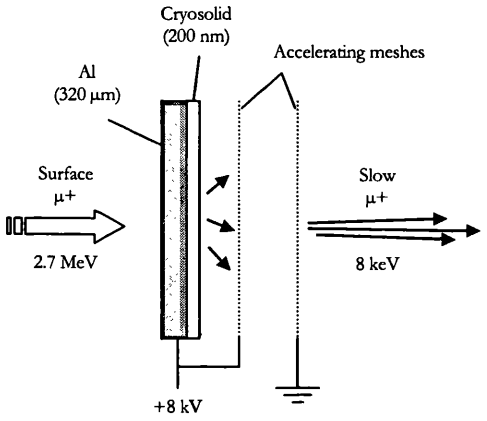

Figure 2.5. *Schematic illustration of the moderator target and accelerator components. Surface muons enter from the left and slow (epithermal) muons escaping the cryosolid are accelerated to an appropriate transport energy (in this case 8 keV).*

On the downstream side of the substrate was a two-stage acceleration system made up of electroformed copper meshes producing planes of equal potential; each had a transmission of 95% and was held sandwiched between copper frames of 48 mm inner diameter and separated by Macor® spacers for electrical isolation. The sample holder and substrate were kept at a positive high voltage, with the second mesh at ground. A 'guard' ring was

mounted in the gap of the first accelerator stage to improve field homogeneity, by reducing influence from the grounded surroundings. For the direct measurement of the slow muon energy distribution (§ 2.4.6), where maximum slow muon transmission was not so vital, the accelerator configuration was changed to include additional stages, with various circuit wiring used between the intermediate grids in order to apply reverse potentials for the measurements.

The high purity gases (≥99.999%) were introduced through a precision sapphire leak valve[**], along a tube directed at the substrate. A quartz thickness sensor was mounted next to the substrate and calibrated by means of interferometric measurements taken in conjunction with film growth. This calibration was found to be independent of growth rate and temperature, and dependent on gas type only.

2.3.2 Transport System

Following the acceleration stage, the muons were transported through 3.23 meters of vacuum tube and two 90° bends using a system of electrostatic Einzel lenses and mirrors (Figure 2.4.b). Each Einzel lens consisted of three co-axial stainless steel electrodes, with the central one held at a high positive voltage (typically ~70% of the accelerating voltage) and the outer two at ground. These were made to the largest diameter possible within the confines of the beam tube to limit beam attenuation.

Two elliptical copper frames holding parallel grids of gilded tungsten wires made up the electrostatic mirrors. These were held 10 mm apart and placed at 45° in the plane of the bend. With a reasonably homogeneous field created between these grids, the front one at ground and the rear one at the accelerating voltage, the slow muons were deflected by 90°. Under-moderated muons would pass through the first mirror and could be detected with

[**] Partial gas pressures could be adjusted very precisely over several orders of magnitude and remained stable.

an MCP placed behind the mirror. The two-bend set-up was used to eliminate the large background from the decay of these under-moderated muons, which had been a significant problem in an earlier single bend arrangement [2.7]. MCPs behind both mirrors were used to detect the beam position during the optimisation of the lens and mirror settings. The mirrors were attached to the system at three points and adjustment was made via linear drives attached to two of these points. The necessary three-bend arrangement naturally made it more difficult to achieve a good focus at the sample position, and the extra length increased the loss of muons via in-flight decay.

2.3.3 Sample Stage

For the developmental procedures that took up all of the early part of this work the 'sample' used was a micro channel plate, as information on beam position and intensity were the main points of interest. The MCP was partitioned into a central and three outer sectors for spatial resolution. The beam spot at this sample position, based on numbers incident in each sector of the MCP and assuming a radially symmetric Gaussian distribution, was determined to 60(15) mm FWHM.

The sample chamber, simply a continuation of the beam tube isolated from the target and transport section by a gate valve, was separately pumped. This reduced bakeout and pump down times after sample changes to about 12 hours. Detector paddles were mounted in a directional array (see Figure 2.4.b) acting as positron telescopes by requiring coincident events. The low numbers of slow muons meant that shielding from background events, from both DEVA and surrounding areas, had to be given full consideration. Lead bricks were built up around the sample end and telescopes to a thickness > 150 mm; a lead wall was also constructed around the final bend to cover the line-of-site opening made by the entry of the slow muon beam line into the sample chamber.

2.4 Moderator Performance and Dependencies

In order to both achieve maximum efficiency and gain insight into the moderation process, various preparation methods were studied for solid argon and nitrogen films for the effects of altering structure and surface properties. N_2 has a slightly larger band gap energy than that of Ar and below 35 K forms a face-centred cubic structure analogous to that of RGSs. The results, also used as a measure of the repeatability of previous PSI results [2.13], are summarised below[††]. As this section is concerned with comparative efficiency only, each set of data is normalised to its own maximum.

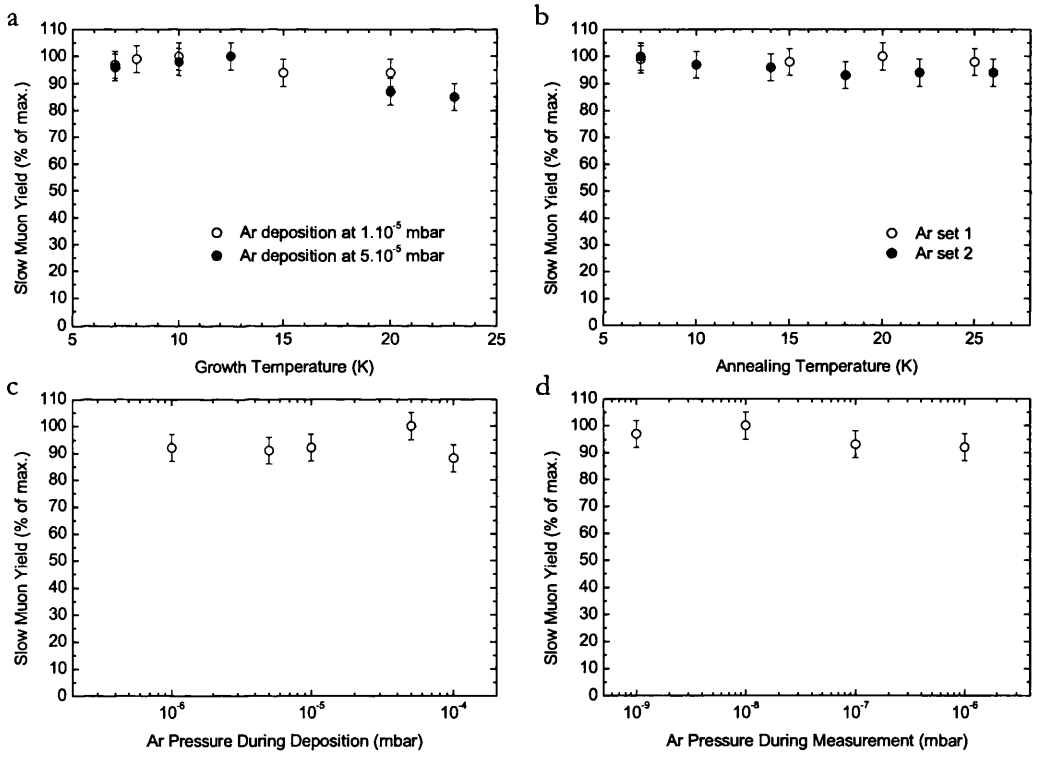

Figure 2.6.a-d. *Results of the preparation and measurement condition studies. Statistical uncertainties are purely a result of low count rates. Counts are performed by summing over the slow muon time-of-flight peak, which is adjusted to include only single events which are coincident with the detection of a decay positron in the telescope within 10 μs of the MCP hit.*

†† These results are discussed more fully in [2.6]

2.4.1 Growth Temperature

Temperature during growth was varied in the range 7-25 K. The growth temperature was then maintained for the duration of each measurement. The film thickness for each temperature was kept consistent (180(6) nm), and argon films were grown at 2 different deposition rates to give the separate data series' shown in Figure 2.6.a. The substrate was heated at 70 K to remove the films between measurements which took approximately 1 hour. Both series showed marginal maxima in the range 10-13 K, with temperature dependence larger for films grown at a higher deposition rate; maximum differences found were 5% and 15% for deposition at 1×10^{-5} mbar and 5×10^{-5} mbar respectively, both with a statistical uncertainty of ±7%.

2.4.2 Annealing

Annealing was investigated for its role in the control of film structure. The substrate was heated for 10 minute periods in the range 7 K to 25 K between alternate one hour measurements at 7 K. Two series' of measurements were taken, both performed on films prepared at 7 K, at 1.10^{-5} mbar argon gas pressure, to a thickness of 180(6) nm. As evident from Figure 2.6.b, very little influence was found in this temperature range, which is limited by the low sublimation temperatures at the level of UHV required for the slow muon beam; the maximum difference in one set of measurements being a decrease of ~7(7)% between 7 K and 18 K.

2.4.3 Growth Speed

Fast growing layers usually possess a greater disorder and porosity, which are expected to respectively reduce the slow muon production efficiency (due to the lower degree of crystallisation) and enhance it (due to the increase in active surface area). To test the effects of deposition rate, measurements were made for Ar films deposited to a consistent thickness of 105(3) nm at pressures ranging between 1×10^{-6} mbar (i.e. a rate of

~0.05 nm s^{-1} for 34 mins.) and 1×10^{-4} mbar (~4.2 nm s^{-1} for 25 secs.). Preparation and measurement (1 hour) was performed at 7 K and Figure 2.6.c shows the results. Very little rate dependence can be seen, with the possibility of a slight maxima (by about 7%) at 5×10^{-5} mbar (corresponding to a deposition rate of ~2.1 nm s^{-1}).

2.4.4 *Maintained Gas Pressure*

Various partial gas pressures during measurement were also used to investigate the long-term stability of the film. Under normal running conditions, reduction in moderation efficiency under UHV was found to be linear in time at a rate of 0.23(2)% loss of the initial yield per hour. This is expected to be due to the deposition of impurities in the vacuum vessel onto the surface of the film. The flow of moderator gas was therefore controlled through the leak valve and adjusted over several orders of magnitude (the upper pressure being limited to $<10^{-6}$ mbar to avoid electrical break-down at the MCP). Measurements were performed at 7 K with an initial moderator thickness of 158(3) nm. This was found to have very little effect on efficiency (Figure 2.6.d), maintaining maximum efficiency except for pressures above 10^{-7} mbar where the film thickness is understood to be slowly increasing (allowing for a small reduction in yield of about 10(5)% - see § 2.4.5).

It also proved impossible to rejuvenate targets that had previously deteriorated simply by replenishing the top layers; confirming that not only is deterioration the result of impurities, but implying that it is independent of the location of the impurity layer – be it within the sample or at the vacuum-solid interface.

2.4.5 *Film Thickness and Muon Escape Depth*

Figure 2.7 shows the yield of slow muons as a function of layer thickness for both Ar and N_2, where each film has been grown separately at 7 K and at a moderator gas partial pressure of 1×10^{-5} mbar. In addition, nitrogen moderator thickness was scanned by

incrementally increasing the film without removal of the previous layer.

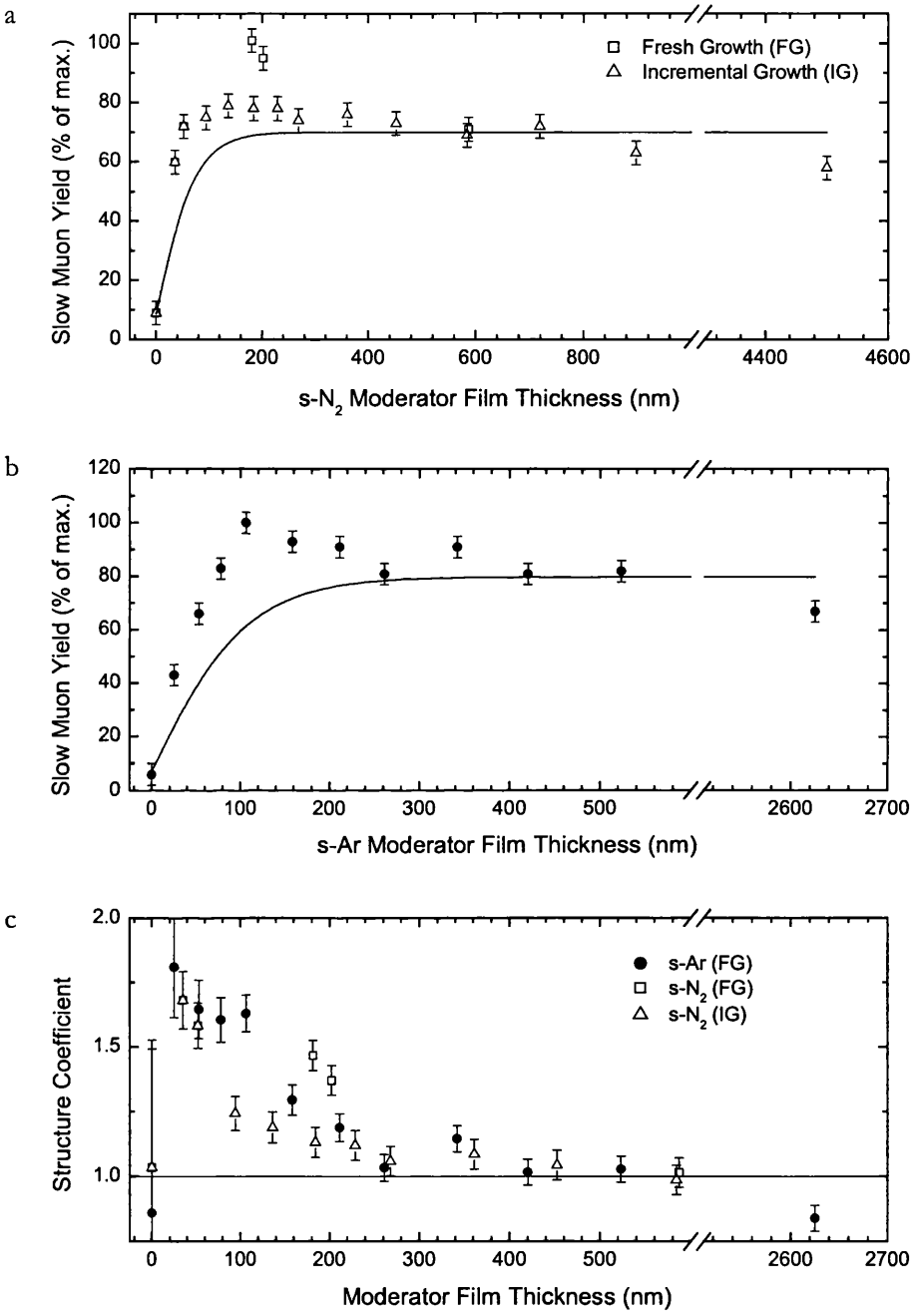

Figure 2.7.a & b. *Film thickness dependence of the slow muon yield in s-N_2 and s-Ar moderators. Results for films freshly grown at each thickness show the same qualitative behaviour for both N_2 and Ar, with maxima at 200 nm and 100 nm respectively. Solid lines show the muon flux from equation (2.1) according to the PSI parameters given in the text.* c. *Multiplication factor required under the assumption that the curves in* a *and* b *correspond to a totally flat gas layer.*

Since even the largest films are still very thin with respect to the muon stopping distribution, there can be little effect due to increased stopping power and film thickness dependence has been linked to the dynamics of the epithermal μ^+ in terms of diffusion-like processes through the film layer . An assumed uniform distribution of epithermal muons within the RGS leads to an exponentially decreasing emission probability with increasing distance from the surface, and an analytical expression for the slow muon flux j leaving the surface as a function of thickness d, with a characteristic *escape depth* L, may be derived [2.14] as

$$j(t) = NL \tanh\left(\frac{d}{2L}\right). \tag{2.1}$$

N is a parameter related to the epithermal muon density in the moderator. Typical escape depths for s-Ar and s-N_2 as given in [2.14] are 67(5) nm and 50(10) nm respectively. Here we have taken d to be the sum of the film thickness d_{film} and a constant d_0, to account, in a simple manner, for the yield at zero coverage – equating the bare substrate with a finite thickness of noble gas. Satisfactory fits cannot be made to our data due to the quite clear maxima in yield efficiency at 100 nm and 200 nm respectively for both Ar and N_2. This had not been observed previously due, most likely, to the conditions of growth at PSI. Indeed, for our own films grown in the same incremental manner, we find that the maximum almost disappears, being replaced by a series that more closely resembles their gradual increase to a saturation value.

The explanation of this peak links the effect of surface structure to the angular distribution of emitted slow muons demonstrated in separate experiments at PSI. There, structured substrates of simple geometry were found to have an increased yield that corresponds directly with the increased surface area [2.15]. This indicates that the distribution of

epithermal muons inside the gas layer is isotropic and they are emitted from the surface with a cosine distribution; a pronounced forward emission would show far less sensitivity to structure, being dependent only on the projected area.

At the temperatures used for forming moderators, the growth of initial layers involves solidification directly from the vapour and is dominated by island formation [2.16][#] as a large number of crystals are individually nucleated. This leads to a defective crystal structure with small grains containing many stacking faults and dislocations. The roughness of the surface of a film formed in this way is still apparent at a thickness of around 100 nm, where the enhanced effective surface area produces a maximum in the slow muon yield. As the average thickness is increased beyond this optimal value, the surface becomes more and more uniform, and the decrease in effective surface area is accompanied by a drop in the slow muon moderation efficiency towards an asymptotic value at large thickness. The incremental build up of layers appears to preclude this effect to a degree.

Figure 2.7.c shows the effect of the changing surface roughness in terms of a "structure coefficient" based on the escape depths determined from the PSI data. Intuitively, the form of this thickness dependent coefficient backs up the argument for a surface structure that becomes increasingly uniform.

2.4.6 Energy Distribution of Re-Emitted Muons from s-Ar and s-N_2 Moderators

Measuring the energy distribution of slow muons leaving the moderator surface is one of the keys to providing a detailed understanding of the interaction of the muon with materials, as well as its own radiolysis products, at low energies. Previous determinations of the slow muon energy distribution at both RAL [2.7] and PSI [2.17] were based on time-of-flight (TOF) measurements, which do not have a simple one to one correspondence with

[#] see also a brief discussion on early layer formation and *wetting* in Chapter 3 (§ 3.5.5)

energy due to the angular distribution of slow muons escaping the moderator. Instead these measurements are fitted by comparison with simulated results encompassing several parameters of the transport system such as the time-structure of the incoming muon pulse, the angular distribution of the slow muon emission from the surface, the field distribution in the electrostatic accelerator and the properties of the deflecting and focussing elements. Simulations performed at discrete energies had to be summed with different weights in order to reproduce the TOF data. The weighting required was then taken as the corresponding muon intensity at the given energy. These results consistently produced energy spectra of slow muons from s-Ar showing a low intensity near zero, with a peak at ~10 eV of ~15 eV width, and a tail to higher energies.

Here the measurement was approached directly through the application of additional retarding grids added to the acceleration section of the transport system. This grid system was developed through numerical calculations of the potential distribution inside several multiple-stage set ups and was shown to produce a well defined potential barrier, by

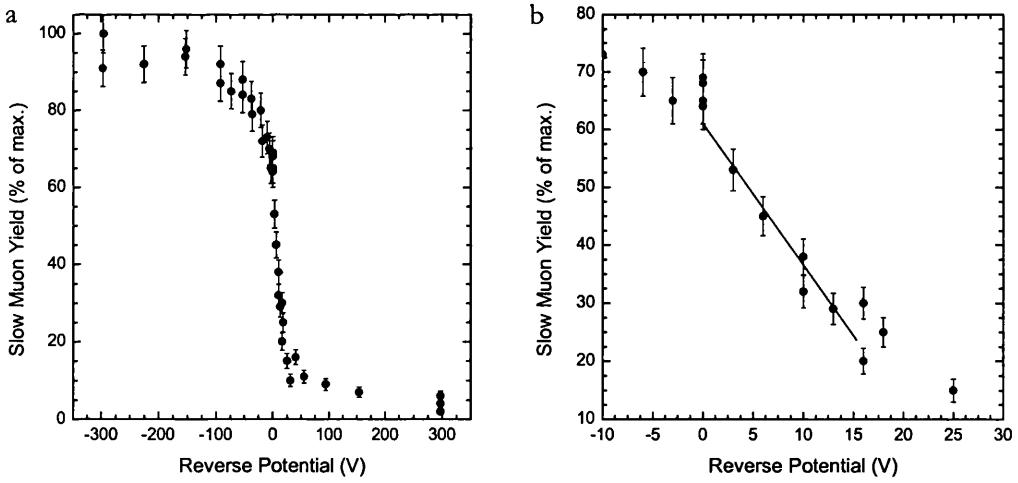

Figure 2.8.a. *Normalised slow muon yield from the s-Ar moderator reaching the MCP versus the retarding potential applied in the first stages of the accelerator. Negative voltages refer to accelerating potential.* b. *Detail enlargement of* a *indicating the linear dependence at low voltage, which represents a flat energy distribution. Film thickness = 105(2) nm.*

providing complete screening from the high voltage accelerating field [2.18], when three intermediate electroformed copper meshes (each 86% transmission) were held at equal potential. This barrier could then be raised and lowered by changing the voltage on a battery pack electrically 'floated' between the sample holder accelerating voltage and the first mesh of the accelerator system. In this way the retarding voltage was finely scanned from –300 V to 300 V, while maintaining a constant total accelerating potential of 8 kV.

An example of the slow muon rate at the MPC as a function of applied reverse potential is shown in Figure 2.8. Several such measurements were made for both Ar and N_2 moderators of thickness 105(2) nm and 180(4) nm respectively, grown at 7 K substrate temperature. Under these conditions, the slow muon rate $F(E)$ as a function of barrier energy E is proportional to the perpendicular component of the slow muon energy distribution $f(E')$ from E to ∞[§§]:

$$F(E) \propto \int_{E}^{\infty} f(E')\,dE' . \qquad (2.2)$$

The slow muon rate is greatly attenuated by applying a reverse potential of a few tens eV. Of particular interest is the linear dependence of rate on the retarding potential up to around 15 V, which has been expanded in Figure 2.8.b. This is indicative of a uniform energy distribution below this energy, which corresponds closely to the energy of the band gap of solid argon (= 14.2 eV), implying that the energy dissipating mechanisms below the band gap (i.e. phonon scattering/creation) are very weak. It also contradicts the idea of decreasing intensity in the muon distribution towards zero energy, which would be revealed as a plateau in the measured yield at low retarding potential. Moreover, simulations based on previously deduced energy distributions, taking into account angular

§§ In practice the upper limit is the cut-off energy of the transport system.

distribution and retarding potential, could not be fitted successfully to the directly measured results. Instead, the most promising fits were obtained by assuming an energy distribution that has a plateau for energies below the band gap width, followed by an exponentially decrease to a small but finite level remaining at high energies. The initial energy distribution $f(E')$ may then be written as

$$f(E') = C \qquad \text{for } E' < E_{gap}, \text{ and}$$

$$f(E') = C \cdot \left[\exp\left(\frac{E' - E_{gap}}{A} \right) + B \right] \qquad \text{for } E_{gap} \le E' < 5000 \text{ eV}, \tag{2.3}$$

where A is the decay parameter of the exponential decrease, B is the constant level at high energies, and C is simply a normalisation constant. Slow muons from s-Ar gave best agreement with data with $A_{Ar} = 30$ eV and $B_{Ar} = 0.1\%$. Nitrogen data suggested a smoother distribution with parameters $A_{N_2} = 55$ eV and $B_{N_2} = 0.15\%$. These distributions are indicated in Figure 2.9. A more detailed comparison of theory and

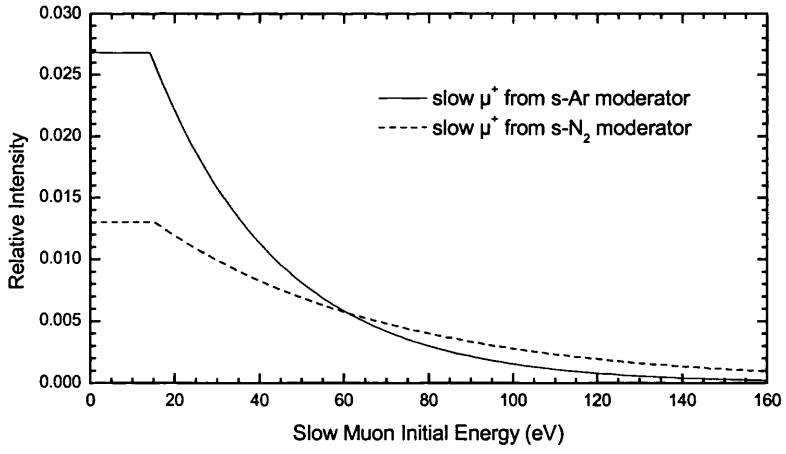

Figure 2.9. *Distribution of the initial energy of slow muons from s-Ar and s-N_2 moderators obtained from reverse potential measurements. The functions are described by equation (2.3).*

experiment is given by Träger in [2.6].

Additional evidence of the angular distribution of emitted slow muons is provided by the boost in yield towards increasing negative reverse potential (i.e. accelerating potential). The flight paths of the muons inside the accelerator are bent towards the beam direction by the accelerating field, allowing some that would otherwise miss the second grid to enter the transport system. No dependence of the emitted muon energy distribution on thickness of the s-Ar moderator was apparent over the range 30.0(5) nm to 517(9) nm.

2.4.7 Conclusions and Discussion

Following these moderator studies, we may conclude that the moderator efficiency showed very little dependence on both annealing (possible small reduction in efficiency at higher temperatures due to decrease in film porosity and therefore active surface area) and partial gas pressure during measurement (possible small decrease at high pressures linked to moderator thickness dependence). A growth rate of ~2.1 nm s^{-1} (5.10^{-5} mbar deposition pressure) gave maximum efficiency, which is consistent with the greater disorder providing two counteracting effects, as described in § 2.4.3, at higher rates. Growth temperature echoes this structural dependence with a maximum in efficiency towards lower temperatures (most clearly defined at a deposition pressure of 1.10^{-5} mbar).

A further effect of surface structure was evident in the dependence on film thickness. We conclude that the escape depth model, although essentially correct, requires the incorporation of the active surface area into the model in order to restore its ability to accurately describe the experimental data.

The epithermal muon emission spectra obtained in § 2.4.6 give a clear picture of the energy

distribution for the first time, highlighting the uniform distribution below the band gap for the two cryosolids studied.

These results are in reasonable agreement with PSI results, where optimal s-Ar moderator temperature was found to be ~15 K, for films of 280 nm thickness, and a slight preference was shown towards higher deposition rates. They also compare well with positron moderator performance [2.11, 2.19]. Optimum positron moderation efficiency has been reported for s-Ar at ~16 K. Annealing on the other hand, shows a far more pronounced effect for e^+ than for μ^+. For instance, the e^+ moderation efficiency of a s-Kr moderator grown at 13 K showed a two-fold increase in efficiency after annealing several times at 42 K. Although positron moderator thickness is of the order of 10 μm, in comparison to a muon moderator of the order of 100 nm, the structure and morphology characteristics appear to play a similar qualitative role. However, large quantitative differences arise due to the nature of the particle within the relevant energy regimes. Even at a few eV, μ^+ still behaves as a point-like classical particle, whereas e^+ has a wavelength that exceeds atomic dimensions. The quantum mechanical nature of epithermal positrons may therefore not be neglected; they are more sensitive to the quality of the crystallites, and in addition may lose energy efficiently to phonons.

For muons, the cryosolids may be considered to act like dense gases with only binary collision processes taken into account, which is justified by the short interaction of the epithermal muons with the solid (the mean free path of the muon is much larger than lattice dimensions). Although many-body interactions may be expected at even lower energies, they are not required for a fundamental understanding of the moderation process. Here we describe some of the basic qualitative features of muon moderation - Morenzoni details more quantitative arguments based on carefully scaled data and theories of proton and hydrogen collisions [2.14].

Below the applicable range of the Bethe-Bloch formula, as the muon reaches epithermal energies, muonium formation within a charge exchange regime is the most important inelastic process remaining. Furthermore, the yield of μ^+ at low energies (<30 keV) is reduced by increasing competition from Mu formation [2.20]. Two mechanisms, which were developed to describe the energy spectra of positrons, have been applied to explaining the final state of the muon as it is emitted from the moderator.

The *spur model* describes a recombination-assisted diffusion mechanism, occurring after full thermalisation. As the muon degrades in a material, it creates spurs (or offshoots) of radiolysis products along its track. As the muon reaches thermal energies at the end of this track it may then capture one of its own radiolytic electrons. The muonium atom must then diffuse to the surface, where the recombination of the muonium electron and a hole could result in the emission of the muon with several eV of kinetic energy.

The second, more favoured, model is the *hot muon model* describing an emission mechanism where the muon is not yet fully thermalised. The muonium formation may occur down to a threshold energy which is the difference between the band gap energy and the muonium binding energy in the solid, $E_{\text{Threshold}} = E_{\text{Gap}} - E_{\text{Binding}}$. Below the threshold level, this energy loss mechanism is prohibited, and the only remaining energy loss mechanisms are a result of relatively inefficient elastic scattering. For moderators where $E_{\text{Threshold}}$ is negative, the probability of the muon ending up as epithermal Mu is large, and the corresponding slow μ^+ yields are low.

Figure 2.10 shows the moderator materials tested at RAL, together with some comparative PSI results. The most efficient moderator target in this study was found to result from solid argon, band gap 14.16 eV, deposited on an Al substrate, producing $\varepsilon_\mu = 2.9\times10^{-5}$ slow muons per incident *surface* muon. This is reasonably in line with the hot muon model

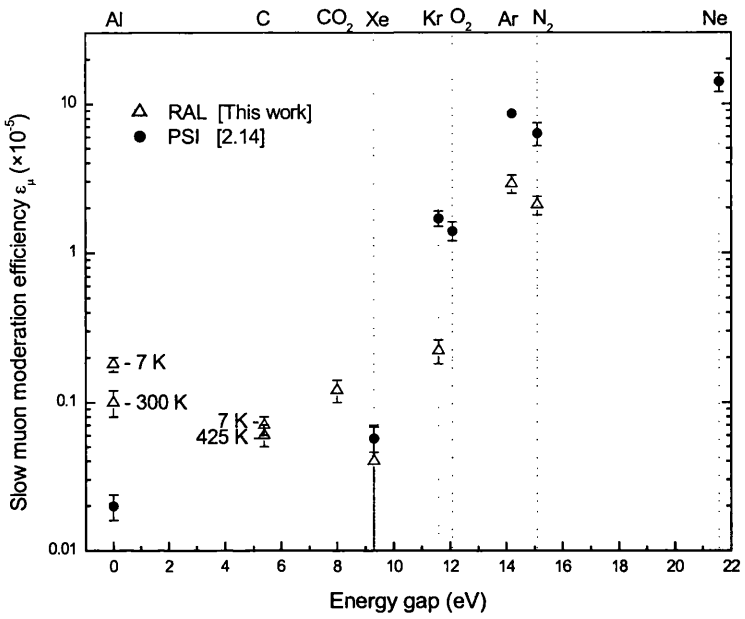

Figure 2.10. *Measured efficiencies for various moderator targets as a function of band gap [2.21, 2.22, 2.23]. Differences between RAL and PSI results for the same material are expected to be due to the narrower momentum spread of the incoming surface muon beam at PSI, which narrows the muon stopping profile.*

with the efficiency seemingly correlated with band gap for other noble gases. Ne, band gap 21.58 eV, giving greater efficiency according to this model (verified by PSI results [2.14]), proved impossible to grow in thick layers at the cryostat base temperature (nominally 7 K) in UHV. Solid N_2, with band gap 15.1 eV, forms a FCC structure below 35 K, analogous to the noble gases, and was found to have an efficiency of $2.2(4)\times10^{-5}$.

A diamond film produced by chemical vapour deposition, CVD, was also tested, as a solid non-van der Waals bonded material with reasonably large band gap (5.4 eV). An efficiency of $7(1)\times10^{-7}$ was found at 7 K; comparable to that of the bare Al substrate value of 10^{-6} at the same temperature. These results for diamond reinforce previous evidence from measurements on LiF and SiO_2, that the existence of a relevant band gap alone is not sufficient to produce high muon moderation efficiencies. However its highly covalent

nature refutes the argument that the poor moderation efficiencies of LiF and SiO_2 are associated with their ionic bound character.

The higher yields gained at PSI may be attributed to the narrower momentum byte of the surface muon beam, $\Delta p_\mu / p_\mu$ = 1.5 % at PSI as opposed to 10% at RAL, which produces a higher stopping efficiency in the film. Absolute efficiency calculations at RAL are also adjusted for efficiency of the transport system (both geometric efficiency and in-flight decay) and MCP.

2.5 Implantation Studies Using Slow Muons (LE-μSR)

Preliminary physics investigations with slow muons were performed to prove the significance of low energy μSR (LE-μSR) at the ISIS facility. To allow fine energy tuning of the pulsed beam a decelerator structure, composed of two 95%-transmission copper meshes, was positioned upstream of the sample. With the upstream mesh held at ground, the downstream mesh and the samples themselves could be positively or negatively biased to control the μ^+ energy between ~10 eV (the intrinsic energy spread at the muon production site) and ~15 keV[***].

The detector paddles were upgraded to a custom detector array provided by Gresham Scientific Instruments [2.24]. As depicted in Figure 2.11, the array was composed of two concentric rings of plastic scintillator, forming an inner and outer shell, with each shell segmented into four equal quadrants. They were also divided in the beam direction to give two complete arrays upstream and downstream of the sample[†††]. This array was designed to subtend approximately 2π solid angle at the sample position.

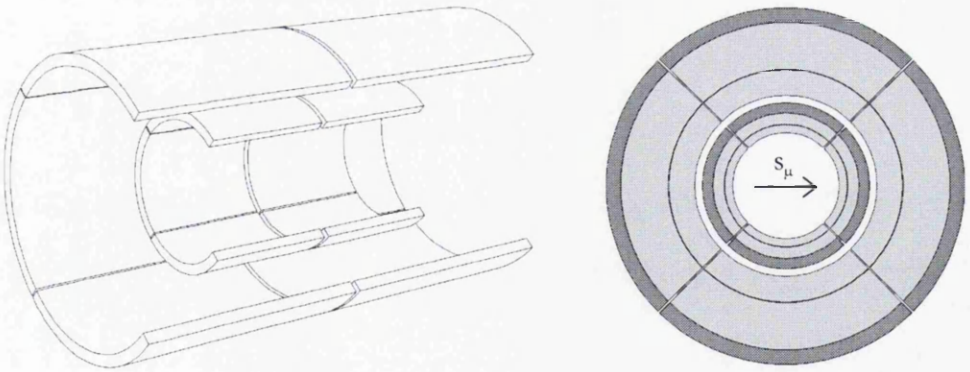

Figure 2.11. *Custom detector geometry.* a. *Scintillator quadrants are shown removed from one of the sides to reveal the layout of the inner detectors.* b. *8 keV muons' eye view (w.r.t momentum direction); the quadrants are oriented at 90 degree intervals with respect to the initial muon spin direction,* s_μ.

[***] Negative bias >7 kV could not be achieved without breakdown of the circuit.

[†††] This split provided both compatibility with the UCL sample chamber (§ 2.7.3) and increased precision in the telescopic effect around the sample.

A solenoid of 104 coils of insulated copper wire wrapped around the chamber gave a uniform magnetic field perpendicular to the sample surface (transverse to the initial muon spin direction) across the sample region. The value of this applied field was limited by resistive heating of the solenoid, at high current, which challenged the heat tolerance of the surrounding scintillation counters. A field of 42.0(8) G was used for the 'energy tuning' LE-μSR experiments.

The 'sample' MCP was replaced by a Parma group sample holder; four samples were mounted on a 4×4 cm Al cube, which could be remotely rotated in order to face a given sample into the beam without the need to break the vacuum. A Kapton® foil collimator with a 70 mm aperture was mounted 0.27 m upstream of the sample to reduce background from muons striking the decelerator structure.

2.5.1 Implantation Profile of Epithermal Muons

A sample of 200 Å copper layer over quartz was chosen to demonstrate depth profiling. The spatial sensitivity and resolution depends not only on the sample material, but on muon straggling, and for Cu depths of 0-1000 Å are expected to be accessible for the ISIS slow muon beam. Shifts of the stopping distribution across the Cu-quartz interface are then apparent in the observed changes in muon asymmetry due to the very different precession frequencies in each material; muons remain in the diamagnetic state in copper, but have a muonium fraction in this quartz sample[##] close to 90(2)% [2.25]. The quartz, a disc of 40 mm diameter, had been optically polished, cleaned and sputtered with a 200 Å layer of copper in an Ar atmosphere. Subsequent examination of the surface by atomic force microscopy showed a modest roughness (~7 nm deep with an average angle of 0.9°); uniform enough to allow reliable 'slicing' experiments to be performed. Auger analysis found, in addition, a 2-3 nm layer of Cu_2O across the surface of the copper, which

[##] Measured in a *surface* muon beam prior to these LE experiments.

was the result of unavoidable exposure to atmosphere. This unanticipated oxide layer has a well known muon precession that cannot be detected within the ISIS frequency passband, and therefore adds an additional feature to the sample profile.

Due to the rather large spot size of the beam (§ 2.3.3) and the inherent difficulties in focussing a slow muon beam passing through two bends, a sample of very pure quartz was first measured as a control. This was a 40 mm diameter slab (the same dimensions as the Cu/quartz sample) of SiO_2 that had been shown to exhibit optimum Mu asymmetry (i.e. 50% of the maximum beam line asymmetry) [2.26].

Measurements of diamagnetic asymmetry values at various implantation energies in the pure quartz (shown in Figure 2.12) show a random distribution of data points around a fitted mean of 12.4(7)%. Assuming there is no large energy dependence in the diamagnetic fraction, this allows us to conclude that the fraction of muons entering the sample is independent of decelerator potential in the range studied. It also provides us with a base (background) level for the diamagnetic asymmetry, for use in subsequent normalisations.

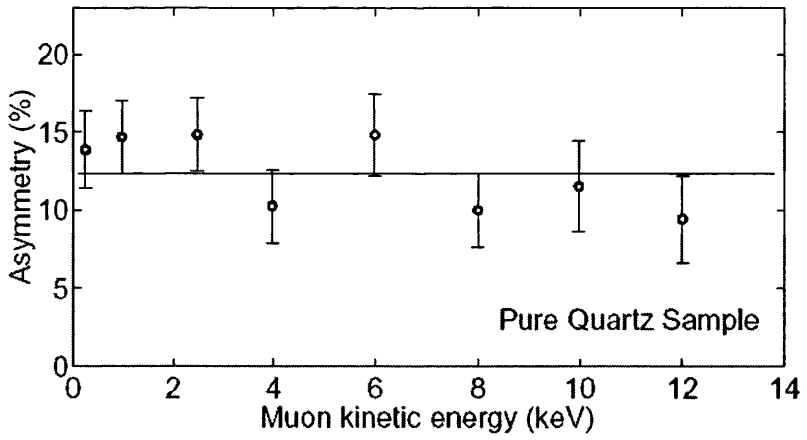

Figure 2.12. *Calibration measurement of LE-μSR in a pure quartz sample. The experimental data, taken at the same energies as the subsequent Cu on quartz experiment, appear to be randomly distributed around a fitted mean value of 12.4(7)% (solid line). These measurements exclude possible decelerator effects on measured asymmetry.*

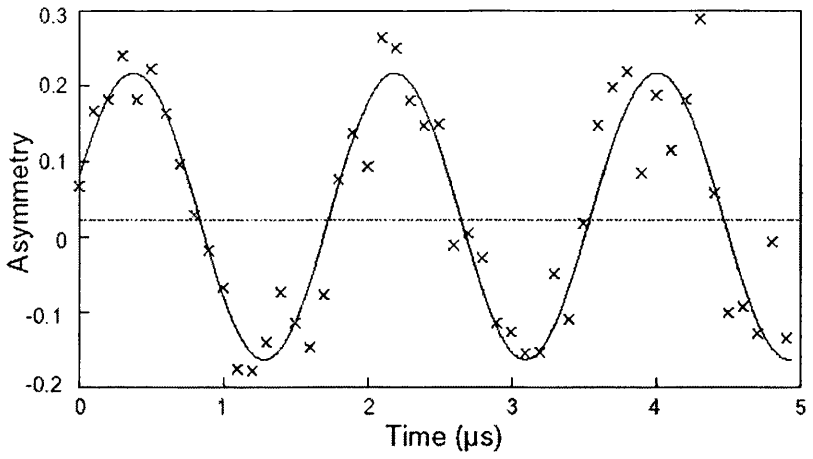

Figure 2.13. *Asymmetry plot for 1 keV muons precessing in the 200 Å film at 42 G applied magnetic field. The solid line shows the best fit curve using a standard μSR decaying harmonic function, which highlights the large asymmetry at this implantation energy and the low relaxation rate that is characteristic of copper.*

Similar measurements were then performed on the Cu on quartz sample at the same implantation energies. A typical asymmetry histogram, obtained for 1 keV muons, is shown in Figure 2.13. This shows the case where the number of muons stopping in the Cu layer is maximized and the diamagnetic asymmetry is about 20.5%. The asymmetry is then reduced with increasing muon implantation energy (Figure 2.14) until it levels off, for energies above 8-10 keV, to approximately 12.5%. This corresponds to the value found for pure quartz (Figure 2.12) and indicates that most of the muons have passed through the Cu layer and stopped in the quartz substrate.

In the absence of an oxide layer the asymmetry would be expected to tend towards a maximum as the energy approaches zero, as shown by the thin solid line in Figure 2.14. The decrease in the measured value at 500 eV indicates the presence of the oxide layer, where muonium formation is prevalent, as is typical of most insulators. The family of curves in Figure 2.14 are derived from Monte Carlo simulations using SRIM-2000 to indicate the effect of different thickness' of oxide layer. They suggest a 3-4 nm oxide layer

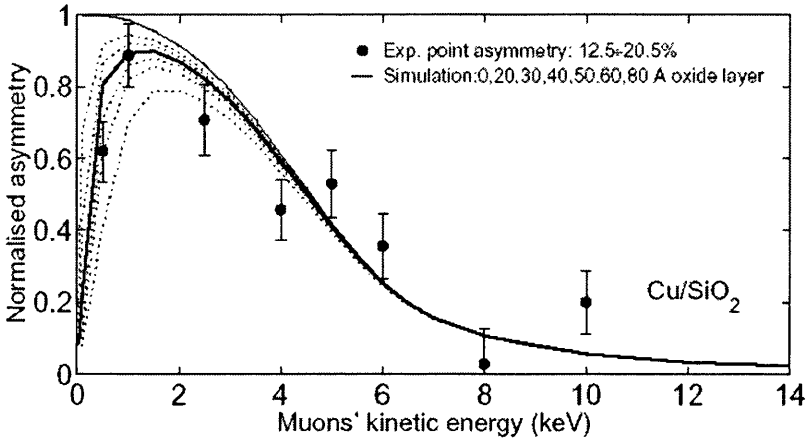

Figure 2.14. *Measured diamagnetic asymmetry as a function of incident muon kinetic energy into the Cu/quartz sample. Examples of the fitted histograms are given above. Simulations of the diamagnetic asymmetry using SRIM-2000 are based purely on the fraction of muons stopped in the Cu layer and are adjusted for a background diamagnetic signal of 12.5% and a total measurable asymmetry of 20.5%.*

thickness (bold curve) which was fully confirmed by the independent Auger analysis of the sample surface, indicating the presence of a 2-3 nm layer.

The experiment confirms that an electrostatic decelerator, employed in front of the sample, allows the accurate selection of muon energy, which retains the narrow distribution characteristic of a pulsed source. The narrow stopping profile produced permits investigations on thin films and interfaces in the range of a few tens of Å.

2.5.2 Investigation of Thin Magnetic Films

A 200 Å copper layer over hexagonal cobalt provided a system within which to explore the potential of a LE muon beam for studying the magnetic properties of thin films and interfaces between magnetic and non-magnetic materials. The interest for this sample lies mainly in the Co film grown by sputtering to a thickness of 800 Å over a 40 mm diameter Si substrate. The morphology was determined by X-ray diffraction and magnetometry, showing the film to be composed of grains with hexagonal structure having

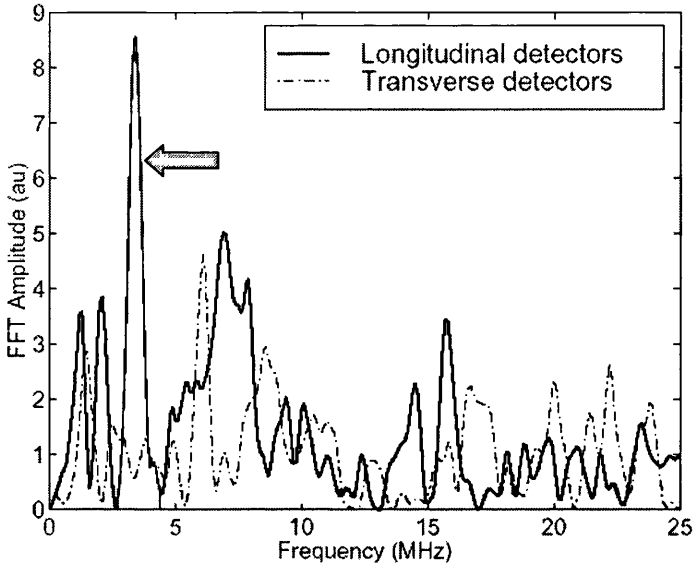

Figure 2.15. *Fourier spectra of the histograms obtained from muons stopping in the hexagonal Co film. The peak corresponding to a muon precession frequency in the expected range in Co is indicated with an arrow.*

the c-axis in the film plane (no preferential direction in the plane was evident). Conventional μSR experiments on Co single crystals at room temperature (where Co has a hexagonal structure) indicate a zero-field precession at ~2.5 MHz, 20% asymmetry, with a damping of 2.5 μs^{-1} [2.27]. No applied field is necessary as the precession occurs in the materials' intrinsic magnetic field.

The spectrometer set-up was the same used for the previous sample, but only detectors in the forward and backward (longitudinal) direction with respect to the initial muon spin direction could detect the precession signal, due to the orientation of the cobalt c-axis. Also, because of the cluster morphology of the film, the measurable asymmetry was expected to be much less than 10%. The muon beam was tuned to 8 keV in order to cross the 200 Å Cu film sputtered over the Co.

Figure 2.15 shows a FFT spectrum of the only data that was attainable due to problems with the ISIS primary proton accelerator during the limited experimental time. By

comparison of the spectra in both the longitudinal and transverse detectors, the presence of a muon precession frequency in the expected range can be seen (peak indicated with an arrow in the figure). The rest of the spectrum consists mainly of statistical noise. We believe this peak to show the existence of the muon precession signal in the small cobalt clusters within the film, although only further experiments will provide information on the spread and relative strengths of the local magnetic fields. Possible investigations include the existence of finite-size effects which depress the fundamental parameters of the magnetic system in its thermodynamical limit.

The overriding difficulty faced in these experiments was one of timescales. Even with the ISIS primary beam operating reliably at maximum current, the maximum efficiency gives $\sim 3\ \mu^+_{LE}\ s^{-1}$ produced at the moderator target on the DEVA beam line. When transport losses are taken into account and during more realistic running conditions, the figure for decay-positron count rate at the sample is an order of magnitude below this value. This means that an entire day of measurement of LE-μSR on DEVA is required to gain the equivalent statistics of less than 1 second of conventional μSR measurements on EMU. The consequences of this for the future of pulsed LE-μSR are discussed in § 2.7.

The following section describes a sample handling apparatus developed to maximise beam time by minimising sample changeover time for this system, where UHV is a necessary running condition.

2.6 Creating a User Facility: the UCL LE-μSR Sample Chamber

One of the central roles of UCL within the collaboration was the provision of UHV sample cleaning and target chambers, to develop the apparatus into a user facility at ISIS.

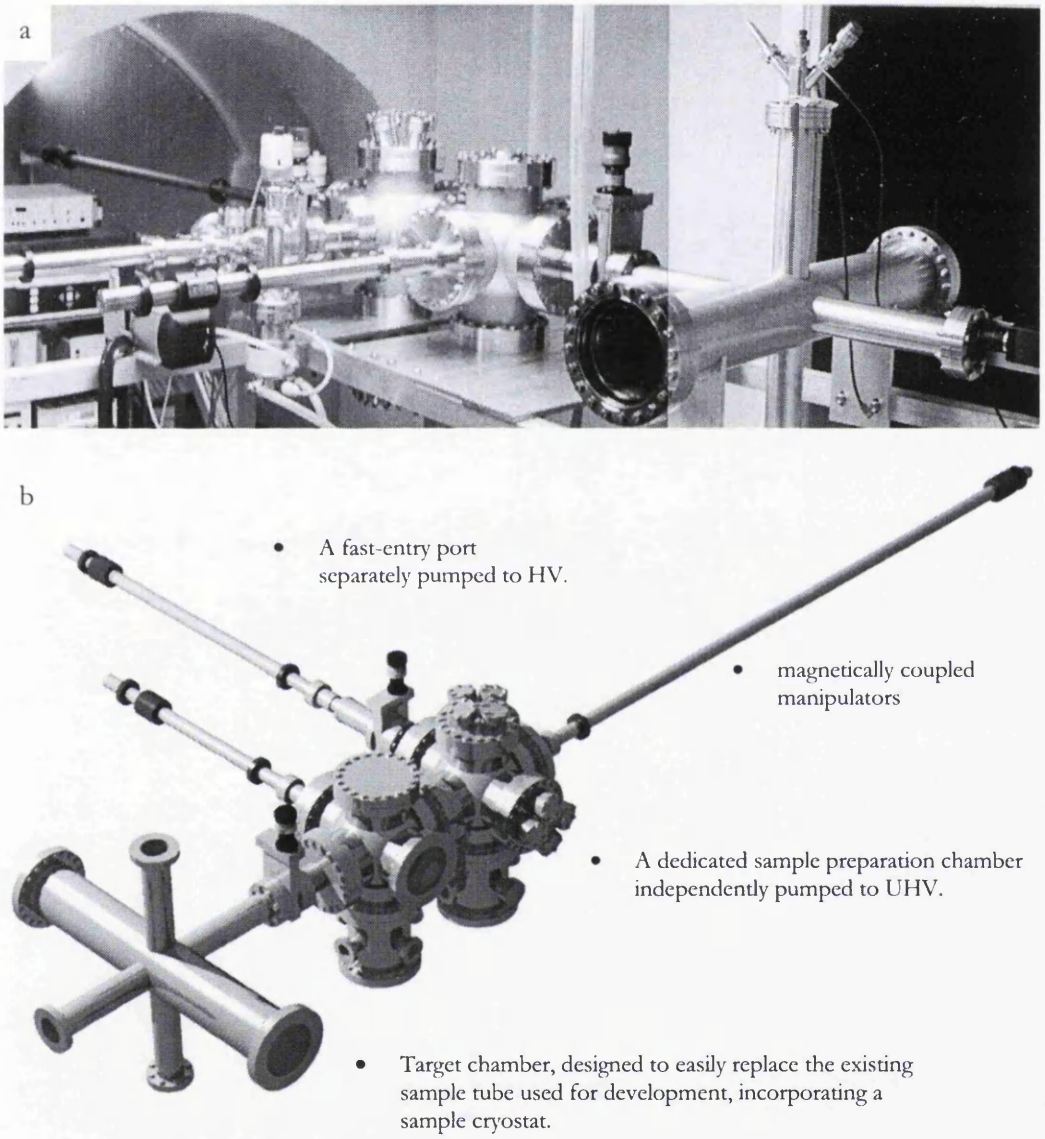

Figure 2.16.a. *A picture of the sample preparation chamber at UCL. The six-way chamber in the foreground is the muon chamber. The top of the sample cryostat can be seen mounted from the vertical arm of the chamber. A camera, extreme right, is used in conjunction with manipulators for accurate sample mounting.* b. *A graphical representation of the system is shown pointing out the main components.*

During developmental stages of the slow muon beam, the introduction of a new sample required bake-out and pump-down for at least 12 hours before measurements could be resumed. The UCL sample chamber was designed to limit the introduction of impurities during entry and preparation of a sample and to allow this to be done concurrently with measurements on the previous sample. Whilst saving time to the order of a day per sample, the handling chamber was naturally required to be user friendly and adaptable to different preparation requirements. The apparatus built to achieve this objective may be considered to be composed of 3 sections, isolated from each other by UHV gate valves and distinguished by the function they perform. Each is detailed here with regard to the level to which requirements are met, and possible improvements, additions, or changes. Caburn MDC UK [2.28] provided the vacuum chamber parts and gauges were from Pfeiffer [2.29].

2.6.1 Access Port.

This access lock, shown in Figure 2.17.a and Figure 2.18, is a small volume chamber that can be quickly pumped down to high vacuum (HV) and prevents contamination of the main chamber. The entry hatch is hinged along one side with a screw-down fixing on the other and is sealed with a rubber gasket built into the flange. This allows samples on Cu holders (Figure 2.17.b) to be quickly exchanged in the 'parking block' of the entry manipulator without the need for any tools and with an adequate seal for reasonable pump-down times to HV. A small turbo pump (TMH 064, DN63), backed by a diaphragm pump (MVP 015 T), is used for this chamber and is capable of achieving a base pressure of 10^{-5} mbar within 1-2 hours. However, the small bore of the backing line between the turbo and the diaphragm pump allowed a pressure gradient which severely limited the backing pressure in lines longer than ~0.5 m. The need for a short backing line therefore meant mounting the pump on the frame of the apparatus, causing potential issues with vibration in the (perhaps unlikely) event that high precision techniques need to

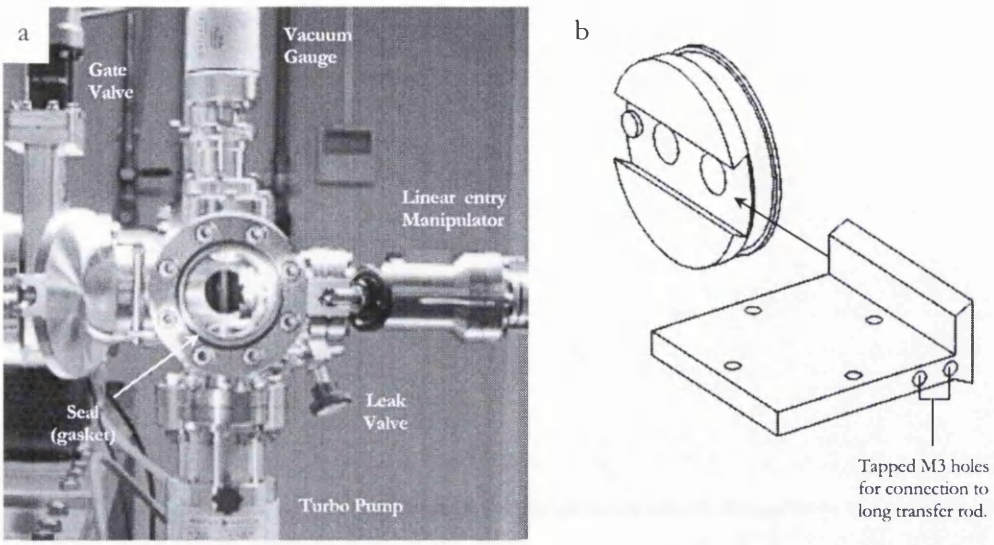

Figure 2.17.a. *A picture of the open entry lock showing the sample transfer block in the centre of the image. The transfer rod moves from the right into the chamber on the left (out of picture). Turbo pump and full-range gauge can be seen to the bottom and top respectively.* b. *Cu sample holder and 'parking block' detail – the spring in the parking block (responsible for pressing dovetails firmly together) is not shown.*

be performed on the samples in the future. Ideally a larger bore backing line and/or more powerful backing pump could be employed.

From here the sample may be passed on a magnetically coupled linear/rotary manipulator, through a (manual) gate valve, and docked with a second manipulator in the main chamber.

2.6.2 Preparation and Handling Chamber

As an intermediate chamber, this next section is designed to remain between HV and UHV at all times, and contains two sample-docking stations to facilitate quick sample changeover (Figure 2.18). The main component is a long travel magnetically coupled linear/rotary manipulator for transport of the sample between the entry stick and the cryostat. This attached to the sample via a screw fitting at the side of the sample holder (Figure 2.17.b) and was mounted on a ±12 mm x-y manipulator to allow adjustment for accurate location of the sample onto the other manipulators. The prepared sample may be

docked with a station in the central 'exchange' chamber, which contains two parking slots to facilitate removal of the previous sample.

The second purpose of this chamber (besides sample exchange) is to carry out sample preparation for future surface studies. This should typically be in the form of cleaning, but may extend to include film growth (e.g. molecular beam epitaxy, MBE), and/or ideally some surface characterisation. One of the main priorities in a surface experiment is to keep the surfaces clean for experimental timescales. The main constituents of the remnant gas in a UHV chamber at base pressure are H_2 and CO, which can react readily with surfaces, and pressures of $<10^{-10}$ mbar must be used to keep monolayer formation time to the order of several hours. Naturally there is some debate as to the value of model (unrealistic) surfaces, and where depth profiling across the first few hundred nm is the aim, the first few monolayers may not be so important. However, as the Cu on SiO_2 study (§ 2.5) illustrates, even the effects of an oxide layer of ~30 Å can have a dramatic effect on the results of a slow muon experiment.

Methods for in-situ cleaning should be catered for and may involve cleavage (applicable to oxides, alkali halides, semiconductors, layer compounds); heating (for desorption of loosely bound species – this has possible consequences regarding inter-diffusion between layers); ion bombardment (this removes layers destructively and should usually be followed by annealing); chemical processing (for specialised cases).

This section is pumped via a turbo molecular drag pump (TMU 520, DN160), roughed and backed by a rotary vane pump (UNO 005 A) through a catalyser trap (URB 025). A bakeout is performed during the initial pump-down from atmosphere and allows subsequent pump-downs from HV (sample entry) to routinely reach a base pressure around 5×10^{-10} mbar. A Pirani gauge and a cold cathode ionisation gauge (Balzers) are

installed for vacuum measurement and a mass spectrometer (VACSCAN 200F) is included for vacuum analysis/ leak testing. Connection to the muon target chamber is made through a (manual) UHV gate valve.

Both turbo pumps can operate at up to a 90° incline, as can the cryostat, meaning that the apparatus can be placed at any orientation around the muon beam axis. In the horizontal configuration, travelling over the full distance of >1 m, the manipulator had a tendency to sag under its own weight by ~15 mm[§§§]. A vertical, or near-vertical, configuration would therefore be beneficial from the point of view not only of floor space[****], but also for parking the sample without the gravity-induced droop causing difficulties. This would however require a control device for the freely-moving long manipulator, either in the form of a simple locking mechanism on the actuator or a mechanical drive to compensate for the more awkward operational position.

The cross-section of the chamber shown in Figure 2.18 suggests a couple of places where compartments may be shortened to reduce the overall travel of the long manipulator. On the other hand, the proximity of a strong magnetic field when Helmholtz coils are placed around the sample may introduce restrictions and/or shielding considerations on the apparatus of the preparation chamber.

To suit its unknown future as an apparatus for experiments not-yet-conceived, the design of the remaining elements has been geared towards adaptability, with several extra ports (including 2 4-port cluster flanges centred on the preparation chamber) available for the various apparatus requirements (i.e. cleaning methods) of a user community.

---

§§§ This is the reason for a second (lower) connection hole in the sample holder (Figure 2.17.b).
**** The full length of the chamber is in excess of 3 metres.

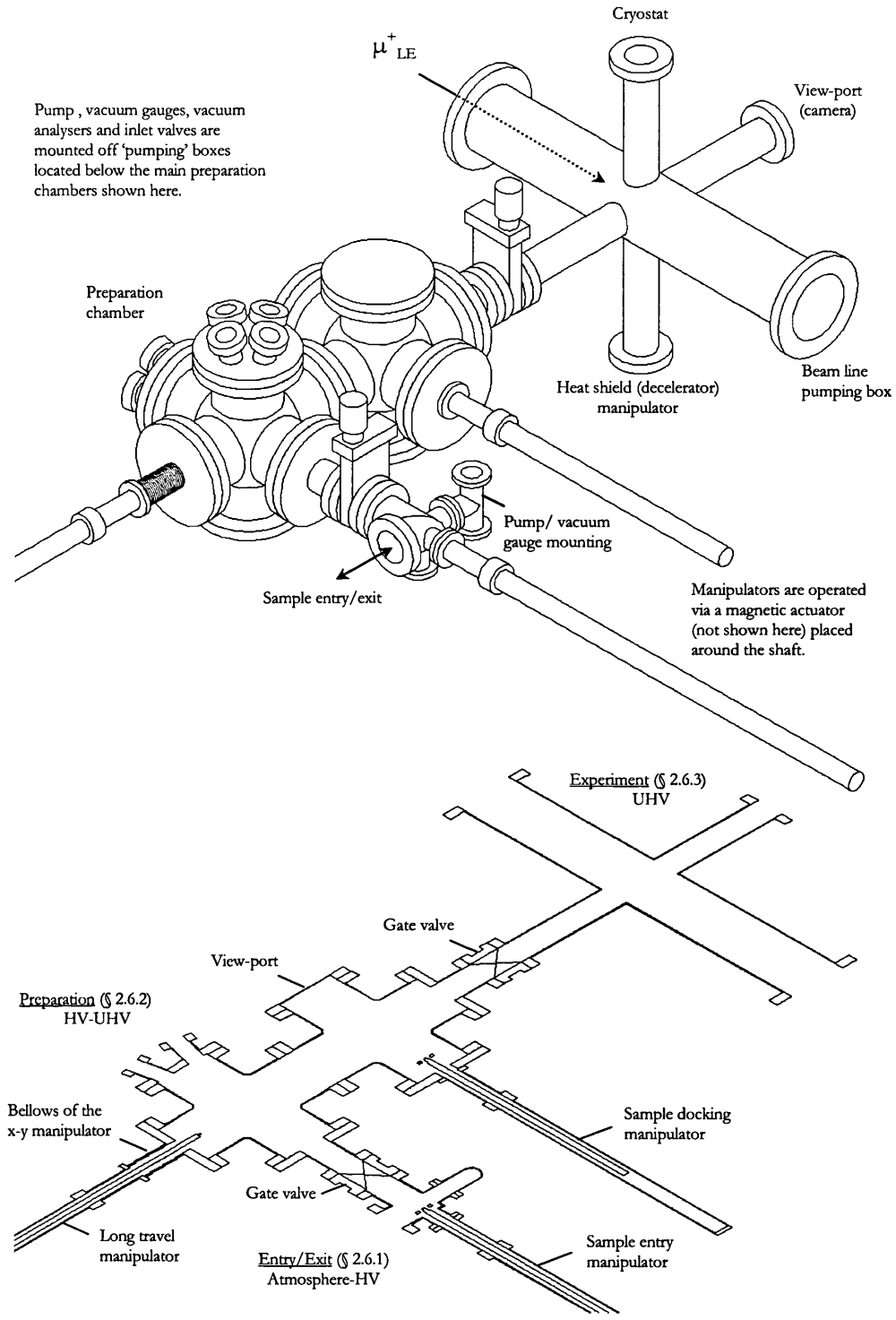

Figure 2.18. *Schematic of the sample handling chambers showing the relationship of the main components. A cross-section through the sample-handling plane is shown below the main chamber – the three component sections are delimited by the two gate valves.*

2.6.3 Slow Muon Target Chamber

The sample holder/cryostat is housed in a special 6-way chamber designed to replace the simple, cylindrical test chamber with a central section of the same dimensions. All 4 side arms are the same length and are a minimum for allowing the slow muon spectrometer set-up, which, in addition to detectors, includes a custom built lead shield and a pair of Helmholtz coils. Opposite the UHV gate valve is a view-port to allow alignment

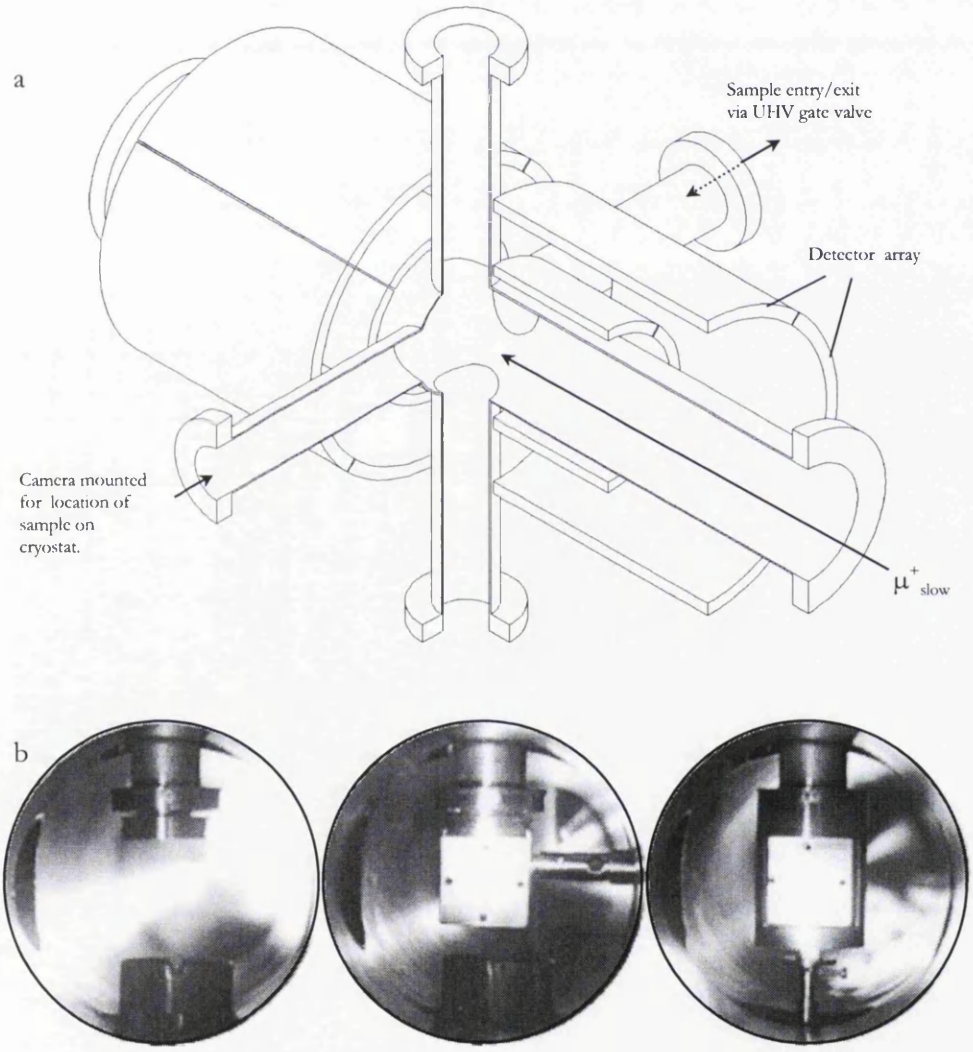

Figure 2.19. a. *Cut-away view of sample chamber with detectors in place.* b. *Location of the sample holder onto the cryostat shown in sequence – seen from the direction of the incoming slow muon beam. The heat shield is held clear from below as the sample holder is positioned, the transfer rod is then withdrawn and the heat shield replaced.*

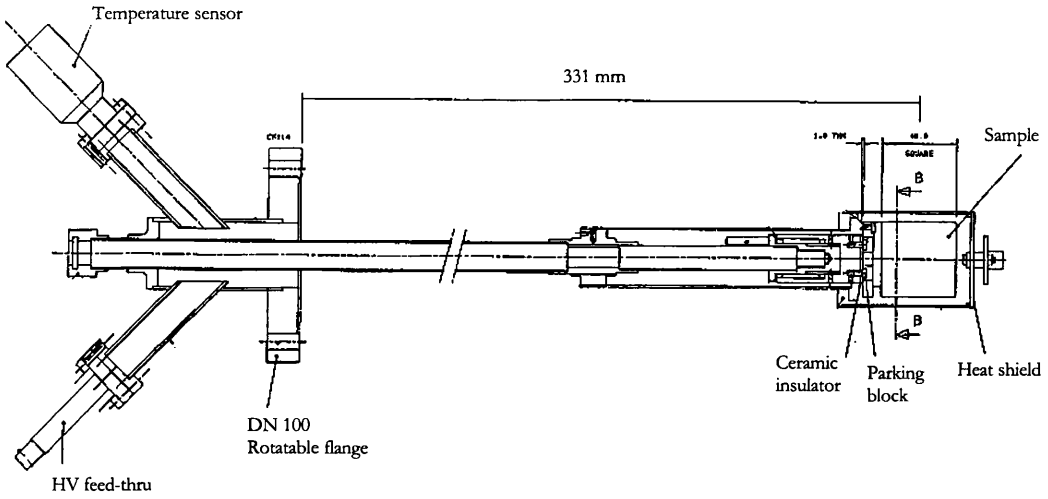

Figure 2.20. *Main components of the Oxford Instruments continuous-flow cryostat.*

of the sample into the cryostat parking block. A third arm holds the cryostat, and is faced on the opposite side by a "z-only" (uni-directional) manipulator for removal and replacement of the heat-shield surrounding the sample.

The cryostat itself is made by Oxford Instruments [2.30] and is shown in Figure 2.20. It is a continuous flow model with a base temperature of around 10 K. A sapphire disk between the cold finger and parking block allows the sample to be electrically floated to ± 8 kV for deceleration/acceleration of the slow muon beam before impact. Teflon coated Cu wire is used for the HV connection – attached at a ceramic feed-through and wrapped around the He down-tube to minimise thermal leaks[††††].

The dove-tails of the sample holder require occasional painting with a thin layer of colloidal graphite to prevented sticking that can otherwise occur in the parking blocks; assumed due to the onset of cold welds forming between the two clean Cu surfaces.

With a camera installed at the view-port on the target station (Figure 2.19.a) the complete

†††† An ideal method for securing the wire to the tube is to tie it with un-waxed dental floss.

apparatus can be operated by a single user, using a monitor to guide the long travel manipulator.

The manipulator used to position the heat shield consisted of a flange mounted on bellows and adjusted along a threaded shaft. This proved very inefficient and impossible to operate without undesirable vibration of the entire apparatus. A short-travel magnetically coupled manipulator with a lockable actuator may therefore prove to be a better option (if more costly).

The heat shield itself provides an ideal platform on which to mount the beam decelerator. Its proximity to the sample should eliminate losses due to the divergence of the decelerated beam, and one may also envisage decelerator arrangements providing a focussing effect onto smaller samples.

This chamber is designed to remain permanently under UHV; pumped via the original pumping box from the test chamber. In this way it achieves the overall aim of allowing samples to be changed in only a few minutes, with no breach of vacuum.

2.7 Prospects for Pulsed LE-μSR

Despite the successful demonstration of pulsed low energy μSR experiments, it is clear that the existing slow muon delivery rate of this apparatus is the limiting factor in its development and the precluding factor in its use as an experimental facility. This is the result of a combination of low incident muon numbers[###], moderation efficiency and sub-optimal slow muon transport.

Analysis of the apparatus in light of the experimental results indicated that transport losses

Relative to dedicated muon facilities, such as PSI.

were primarily due to the position of the final electrostatic lens. This was mounted asymmetrically, a smaller distance from the last mirror than from the sample position, to accommodate the gate valve (Figure 2.4), and resulted in a large beam spot with a significant fraction of the muons hitting the decelerator structure or missing the sample altogether. Pachl [2.31] has shown, via Monte Carlo simulations, that the beam spot may be reduced by a factor of 4 in area by the introduction of a fourth lens in front of the sample. This should improve beam intensity at the sample by at least a factor of 2 and perhaps more, depending on the full extent of the beam divergence. A second approach to improving transport losses could be simply to transport the muons at higher energy. However, a 2-fold increase in accelerating potential, for example, would only attain a 30% decrease in travel time (i.e. only ~10-15% increase in muon survival), and the small gain may not be worth the extra technological effort.

Further increases in moderation efficiency seem some way off. The high initial energy of surface muons poses the greatest difficulty and severely limits the effectiveness of the rare gas moderation (recall the energy distribution in Figure 2.3). Once this can be addressed, the limitation of losses to processes such as muonium formation, using knowledge of the muon-RGS interaction, may become important.

A greater incident muon flux[§§§§] is therefore currently the only solution to allowing the pulsed slow muon apparatus to operate on practical timescales. PSI boasts a DC beam providing two orders of magnitude more incident surface muons (see Chapter 1, § 1.5)[*****], and for this reason the PSI group leads the field in slow muon research, with several publications to date (see [2.34] and references therein).

The pulsed beam has the potential disadvantage of low timing resolution, due to the finite

§§§§ As promised by projects such as the European Spallation Source (ESS) [2.30] or upgrades to ISIS.

***** Even greater rates (one order of magnitude) will be available with the upgrade to the PSI Muon Facility planned for the years 2003/2004 [2.31].

pulse width, but this could be overcome by allowing slow muons to 'collect' before pulsing the accelerating potential. The DC beam, too, is not without its disadvantages. Energy resolution is limited to ~500 eV by the need to trigger the timing circuit with a detector downstream of the moderator, although Morenzoni suggests that this may be overcome by the application of an energy 'buncher' downstream of the beam trigger itself [2.14]. The pulsed beam apparatus does not require such measures, and has a very small (~O(10 eV)) uncertainty in energy, due only to different paths through the transport system and the natural energy spread on emission, but it is true that this advantage may be lost anyway if the depth resolution of the beam is limited by straggling at low energies (perhaps to ~500 eV [2.35]).

Some members of the scientific community believe the essential role of Ultra Slow muons is in studying bulk properties on "rare" samples and materials [2.2] and that the relevance of the ability to study ultra-thin films and surfaces is therefore limited. Experimental interest to date, concentrating on depth profiles in various magnetic materials, does not seem to support this view, although there has been no push to increase the depth resolution available at PSI.

The RGS moderation technique has been shown here to be fully applicable to a pulsed source. It is a relatively simple technique and straightforward to implement. By contrast, the only competing method involves the resonant laser ionisation of thermal Mu, which requires high powered synchronised laser illumination; a technically demanding procedure which is currently limited to efficiency of the same order as the RGS moderators.

3 CONDENSED NOBLE GASES ON SILICA POWDER

3.1 Motivation

This chapter deals with the interaction of the muon with solid noble gas layers and the processes controlling its subsequent release into the vacuum. This has obvious consequences for understanding the efficiency of slow muon production using rare gas moderators; particular in view of the fact that control of the environment may allow the muonium fraction to be suppressed in favour of the bare muon – this was considered a possible limiting factor for efficient slow muon production.

The experiments performed are an extension of earlier work by Harshman [3.1] where helium was adsorbed onto ultra fine Cab-O-Sil® silica powder. Studies by Harshman and others [3.2] provided evidence that muonium is probably formed from muons stopped in the bulk of the powder grains, and then diffuses the short distance to the surface. Also shown was the effect that the muonium fraction appears to be suppressed as the fraction of the surface covered with helium atoms is increased. The mechanism leading to the suppression of the muonium yield was suggested to involve the gas in one of two ways, which were impossible to distinguish unambiguously from the available data. The gas atoms could be considered to have a passive role, covering up active sites at the powder surface and preventing bare muons from forming muonium; alternatively the gas could play an active role, with gas ions scavenging the electrons from muonium formed within the powder. The aim of the work in this chapter is to distinguish these two mechanisms through a systematic study of adsorbed noble gases, where the lower ionisation energies for the heavier atoms should result in very different behaviour. By probing some of the basic energetics of muonium formation in this way, we once again investigate formation

processes such as the spur model and the hot model, which were introduced in § 2.4.7.

The following sections introduce the powder-gas system and briefly summarise the earlier research. We then detail the experimental method with regard to powder preparation, gas handling, and isotherm measurements used to calculate surface coverage. Finally, we present our results and draw what conclusions we can about the proposed models.

3.2 Cab-O-Sil® Silica Powder (EH-5 grade)

The Cab-O-Sil® fumed silica powder in this study was obtained from the Cabot corporation [3.3], where it is produced by vapour phase hydrolysis of $SiCl_4$ in a hydrogen oxygen flame. The resulting condensed amorphous particles then collide and sinter together to form aggregates with dimensions of a few tenths of a micron; an example is shown in the electron micrograph of Figure 3.1. Cab-O-Sil® is currently the purest available SiO_2 powder with very small particle size, and has been used in various muon studies of surface effects and catalysis (see e.g. [3.4] and [3.5]). Some properties of the powder are given in Table 3.1, the main qualities of interest being large surface area and high purity.

The true density of the Cab-O-Sil® aggregate is about 2.2 g cm^{-3}, but the bulk (tap) density of uncompressed Cab-O-Sil® is much lower when compaction and agglomeration* is kept to a minimum, resulting in the particularly low density shown for this EH-5 grade powder. Alternative grades are available catering for various particle sizes and purity levels required in such applications as thixotropy, emulsification, anti-caking, gloss-reduction and anti-slip coatings. The nature of Cab-O-Sil® EH-5 in its initial dry state makes it quite difficult to handle unless adequately compacted, as the fluffy white powder has a tendency to flow.

* Large agglomerates are formed during compaction by the mechanical entanglement of the aggregates.

Table 3.1. Properties of the Cab-O-Sil® silica powder sample [3.6].

Grade	EH-5
Surface area	380 ± 30 m^2 g^{-1}
Tap density	40 mg cm^{-3}
Mean grain diameter	70 Å
Average particle (aggregate) length	0.2-0.3 μm
Major impurities	HCl 30-40 ppm Fe 3-4 ppm Al 3-4 ppm

Figure 3.1. *Electron micrograph of a Cab-O-Sil® fumed silica aggregate showing the outlines of individual primary particles. Magnification approx. 350,000 ×. (taken from [3.6])*

3.2.1 Structure and Surface Chemistry†

Cab-O-Sil® is an amorphous powder as a consequence of the extremely rapid cooling of the aggregates during production. The particles themselves are essentially spherical and gas adsorption studies by Cabot have shown the material to be non-porous, leaving almost all surfaces certainly accessible to the gas atoms used in this study.

Isolated and hydrogen-bonded hydroxyl (OH) groups attached to the silicon atoms of the particle surface bestow some very hydrophilic characteristics upon the powder; the EH-5 grade can pick up ~7% moisture (by weight) at 50% humidity and ~20% moisture at 80% humidity, measured around room temperature. These hydroxyls cover only part (about half) of the particle surface‡, with siloxane (Si-O-Si) groups covering most of the rest of the surface, which are themselves hydrophobic.

It is necessary to protect the powder from ambient atmospheric conditions, but moisture may be driven from the surface by heating and/or pumping. Above 110° C the powder undergoes reversible dehydration as adjacent hydroxyls combine and are released as water, leaving behind additional siloxane groups. The hydroxyls may be restored by exposure to air at 100% humidity or immersion in water. Heating beyond 800° C leads to sintering of the fine powder, and an irreversible reduction in the surface area.

Surface hydroxyls are fundamental to most of the useful properties of Cab-O-Sil® and we shall see in the following section how they appear to play an important role in the depolarisation of Mu spin on the silica surface, and also in the diffusion rate.

† Data taken from reference [3.6].
‡ ~4.5 OH groups per nm^2.

3.2.2 Muons in Cab-O-Sil®

A summary of the extensive earlier work on silica powder surfaces is given in a 1986 review by Harshman [3.7], which along with his doctoral thesis [3.1] provides much of the background to this current work. The sphere of these investigations extends into the areas of surface diffusion and relaxation, surface reactions and catalysis, and surface emissions (which initiated the birth of slow muon beams via moderation – see Chapter 2). Here we concentrate on muonium formation and dynamics and some of the open questions that remain despite work going back to the late seventies.

Mu forms readily in both crystalline and fused (amorphous) quartz (see Table 3.2), where epithermal processes (i.e. the hot muon model) are expected to play the most significant role [3.8]. Applications of high electric fields to bulk fused quartz [3.9], where there is no dependence of muonium yield on **E** (up to 60 kV cm^{-1}), indicate that the spur mechanism does not feature heavily and the apparent lack of temperature dependence discounts thermal processes.

The muonium fraction remains significant for the powdered material and it is generally assumed that the majority is formed in the bulk of the particles via "bulk" processes as the specific surface area has little effect on muonium fraction. Additional surface effects account for discrepancies between bulk and powder results and appear to have some small temperature dependence which, if responsible for the drop in muon yield, suggests links with the time spent on the surface and the increasing probability of ionisation.

The state and location of the muon upon thermalisation is most easy to determine. Early results showed that the effect of introducing O_2 into the powder interstices was a linear increase in relaxation with O_2 concentration [3.2]. The powder was shown to act like very coarse moderator gas, with little muonium trapped in the grains, and gave a lower limit of

Table 3.2. Muonium measurments taken at 6K in various amorphous silica samples.

Material	Temp. (K)	Muonium Fraction (%)	TF Relaxation Rate (μs^{-1})
Bulk fused SiO2	6	79(3)	3.3(5) (a)
	295	79(3)	0.20 (a)
Cab-O-Sil® EH-5	6	-	2.49(14) (b)
	6	-	1.08(5) (c)
	6	38(4)	3.71(36) (d)
	300	50(2)	0.45(5) (d)

(a) Brewer [3.11]
(b) Harshmans' sample prepared at 110°C
(c) Harshmans' sample prepared at 600°C
(d) This work.

~97% of formed Mu escaping into the voids at room temperature. This also implied a diffusion constant of ~2-4×$10^{-7}$$cm^2$ s^{-1} if one may assume the Mu is formed in the centre of the grains. It was later shown that the majority of Mu resides on the grain surfaces or extragranular region at temperatures as low as 6 K, and that escape from the grains is probably not diffusion-controlled [3.10], unless the slowing muon causes some localised heating in the grains[§]. An alternative mechanism by which the bulk-formed muonium may escape the grains is via (temperature-independent) direct thermalisation, which requires a large negative muonium work function ($\Phi^{Mu} \sim -2$ eV).

Relaxation measurements to low temperature (see Figure 3.12) are characteristic of diffusion on the grain surfaces, and are explained as the result of motional narrowing (via surface diffusion from a low temperature maximum, where the Mu is essentially immobile at the adsorption site), followed by trapping peaks (when the Mu reaches less common depolarisation centres; related to surface impurities) in the range from 25 to 50 K (and

§ Mu is static in a bulk sample below ~50 K [3.11].

perhaps even up to 100 K). Harshmans' samples, prepared at two different bake-out temperatures to yield different surface hydroxyl concentrations, both displayed the same general behaviour with a clear reduction in relaxation accompanying the decrease in surface hydroxyl concentration, illustrating the strong influence of these OH groups.

Mu relaxation in the powder is decoupled by longitudinal fields of a few Gauss (recall Chapter 1, § 1.6.1), which indicates that the mechanism is caused by random local magnetic fields (RLMF), or random anisotropic hyperfine distortions (RAHD), or a combination of both.

RLMFs are expected by the proximity of hydroxyl protons and paramagnetic impurities. However, ZF measurements have proved to be inconsistent with a static Mu atom (which would display a recovery to $\frac{1}{3}$ of initial polarisation at long times), while LF measurements have shown inconsistencies with a dynamic Mu atom (which would display continuing relaxation to long times). RLMFs are therefore not the predominant cause of relaxation on the silica powder surface.

RAHD is the mechanism to which relaxation in bulk fused quartz is attributed (muonium is localised at the centre of the tetragonal "cage" of the micro-crystal structure and the anisotropic component of the hyperfine interaction is oriented along the randomly directed c-axis). The hyperfine interaction for muonium adsorbed onto a surface is by its very nature anisotropic, and Harshman developed a simplified RAHD model that accounted for all of the characteristics he observed.

The picture of the temperature dependence of muonium dynamics is supported and completed by studies of the isotropic component of the hyperfine frequency, A_μ, which maintains the vacuum value above ~100 K, appropriate to the inter-granular region. As the temperature is decreased there is an increasing reduction in A_μ (up to –0.6% at 17 K) as

Table 3.3. Properties of the gases used in this study.

Gas	Cylinder purity (%)	Ionisation energy (eV)	Melting point (K)	Boiling point (K)
He	99.995	24.59	0.95	4.22
Ar	99.999	15.76	83.8	87.3
Kr	99.99	14.00	115.79	119.93
Xe	99.993	12.13	161.4	165.1

muonium is apparently adsorbed onto the powder surface [3.12].

The addition of helium on to the surface of Harshmans' sample prepared at 110° C was accompanied by a strong reduction in the Mu asymmetry [3.7]. This showed that the cross section for charge-exchange is very significant at the silica-gas interface. However, the true origins of the entire muonium fraction remained ambiguous; a distinction could not be made between Mu formed at the surface, which is suppressed by the presence of the He gas, and Mu which is formed in the grains and diffuses to the surface, where its e^- may be captured by a He^+ ion produced in the ionisation track of the stopping μ^+. The systematic study of noble gases in this work allows the distinction of these processes as the possibility of stripping the e^- from the Mu atom is far less likely for the other noble gases (see Table 3.3), and indeed should not be allowed in the case of Xe. Mu has an ionisation energy very close to that of H.

The thermal properties of the gases are included in Table 3.3, as they are important for the controlled adsorption onto the powder surface, which is dealt with in § 3.5.

3.3 Preparation of the Powder Sample

An aluminium sample cell was provided by ISIS and attached to a sample stick placed in an Oxford Instruments cryostat with a temperature range of 5-350 K. The cell is shown in Figure 3.2 and consisted of a plate with a cylindrical sample cavity of diameter 24 mm and depth 5 mm, with a thin capillary linking the cavity to the gas system.

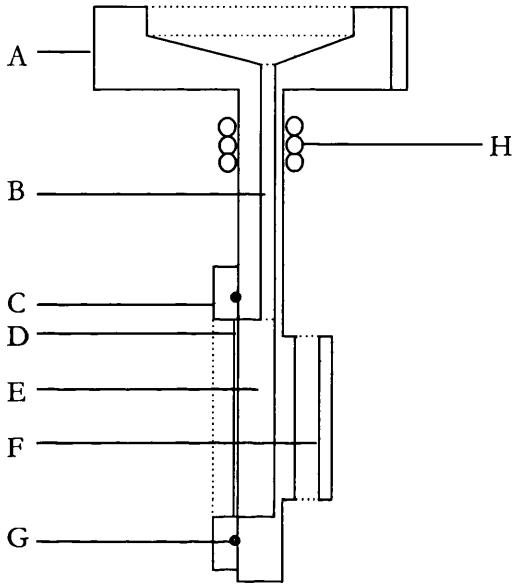

Figure 3.2. *Cross section of sample cell. The cell connected to the cryostat at flange A with the muon beam incident from the left. Gas reached the sample space via capillary B, which was packed with glass wool towards the lower end to prevent powder being 'sucked' out during evacuation. A stainless steel bezel, C, with a welded titanium window, D, was mounted with an indium seal, G, using brass screws. The temperature sensor was mounted in a block, F, behind the sample space, E (diameter 24 mm × depth 5 mm). Some resistive heating wire, H, was wrapped around the capillary section (and also the bottom section of the cryostat down-tube) to supply additional localised heating to prevent blockages.*

The tap density of Cab-O-Sil®, 40 mg cm^{-3} (Table 3.1), is equivalent to a muon range of about 3 cm, preventing the efficient stopping of muons within the sample cell. The powder was made both denser and more manageable by creating several pellets in a 6 mm diameter PTFE die with approximately 60 kg applied (i.e. a pressure of ~200 bar). The resulting

brittle pellets were then easily broken up to give a coarse powder with density 175(2) mg cm^{-3}, with an approximate stopping power in the 5 mm deep cell of 87 mg cm^{-2}. Three Ta foils were placed in front of the cell window (11 mg cm^{-2} each) to ensure the muon range was within the powder.

The compressed powder was then placed in a jar and baked in a vacuum oven (a few mbar at 150 °C) for 24 hours. A control sample was also evacuated overnight at 10^{-4} mbar without heating, in order to allow for a comparison. Both showed a loss in mass due to water vapour leaving the surface, at –12.5(1)% for the baked sample and –3.2(1)% for simple evacuation. The difference is taken to be the additional loss of hydroxyl groups in the baked sample, via the reversible dehydration mentioned earlier. We found that in the lab environment the baked powder could increase in mass at a rate of ~0.1% per min. Thus, our sample was handled in an argon atmosphere after the bakeout stage, during the transfer to the sample cell. The cell was then connected to the gas handling system and evacuated. This cell was loaded once and then used throughout this study, being kept sealed and evacuated for several months at a time between experimental periods.

Due to the difficulties of handling even this compacted powder, the initial loading resulted in powder contamination of the indium wire, preventing the formation of a good seal at the window. The extent of this 'leak' in the gas system (where close control of the constituents was crucial) required the cell to be opened, cleaned up, and re-sealed in the relatively humid laboratory atmosphere. The unavoidable exposure lasted only about half an hour but may have significantly increased the hydroxyl concentration (see § 3.6). In future this could be avoided by producing a compacted pellet of the correct dimensions. We suggest this could be achieved through two compression cycles – the first producing a fine manageable powder of the kind described above, followed by a second compression into the final pellet shape.

3.4 Gas Handling

The gas handling system was provided by ISIS, with the layout shown in Figure 3.3. Consisting of 4.6 and 1.8 mm inside-diameter stainless-steel tubing and standard Swagelok® components, it was equipped with two baratron pressure gauges in contact with the sample volume, covering 0 to 1000 mbar at 0.1 mbar resolution and 0 to 10 mbar at 0.01 mbar resolution. A turbo-molecular pump was used to evacuate the pipe-work and gas connections allowed up to two high purity gases to be connected simultaneously, although no gas mixing was performed for this work.

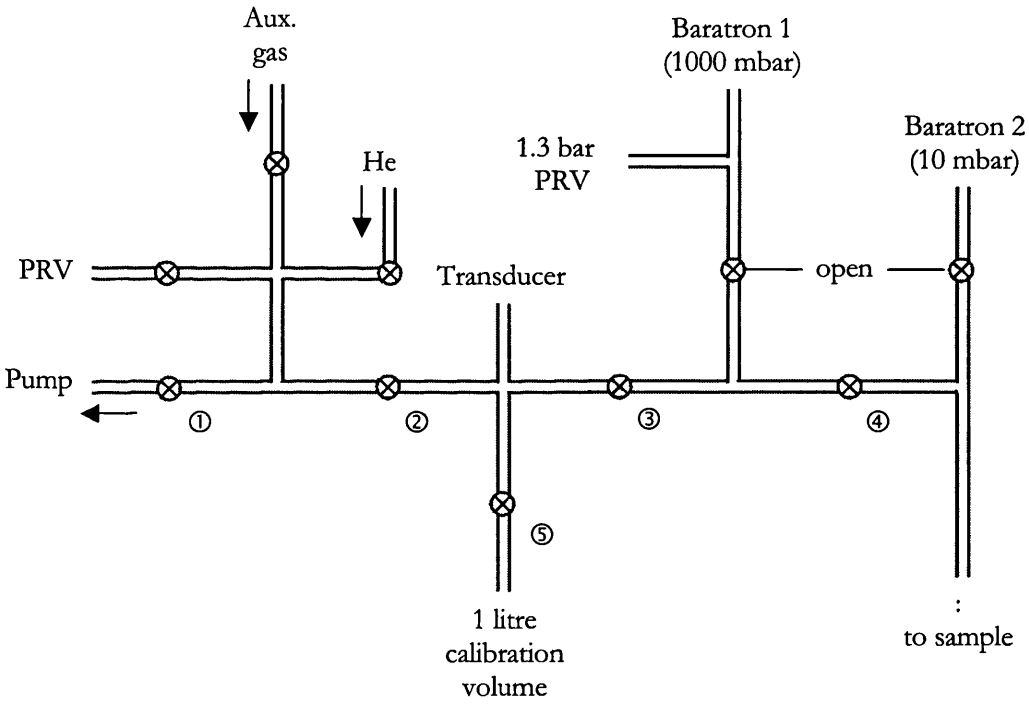

Figure 3.3. *Schematic of gas rig. Manual valves* ①-⑤ *were used to control most of the experiment – see text. Lecture bottles of the various gases were connected to the auxiliary port as required and the section of the line up to* ② *was purged in three cycles to avoid introduction of impurities. A thin flexible stainless steel line led to the sample. Pressure relief valves (PRVs) protect the system.*

Once the whole system had been connected and evacuated for over 24 hours, volumes were determined using helium, because no measurable volume of the gas would be

adsorbed. This was performed with the entire system at room temperature. For this discussion on calibration, and the following on the experimental procedure, the important volumes are denoted with subscript references to the containing valves in Figure 3.3, i.e. the volume between ① and ② is referred to as V_{12}.

Based on a known pressure in a 1 litre standard volume, the 'dose' volume V_{34} was determined to be 14.6(2) cm^3 and the total volume beyond ③, the sample contact volume V_S, was 49.6(6) cm^3. This sample volume includes several metres of flexible steel tubing leading from ④ to a valve at the cryostat (21.2(2) cm^3), and the cryostat down-tube and sample cell (13.8(3) cm^3).

When changing gases the regulator and entry section of the system tubing was purged in three cycles of pressurisation to about 1 bar followed by evacuation. This ensured that impurities entering the system remained negligible.

Since the experiment involved progressively adsorbing small fractions of a given gas onto the powder, each step required equilibrium to be reached for both uniformity of coverage and the simultaneous adsorption measurements (§ 3.5) themselves. The time required for this equilibrium condition (greater for lower coverage) in addition to the temperature changes between the relevant growth temperature of the gas and the 6 K measurement temperature, for each data point, made this a necessarily protracted experiment.

This is clear in a plot of the pressure logs**, Figure 3.4 and Figure 3.5, which also serve to illustrate the break-down of the stages repeated for each experimental measurement.

** Pressure logging was primarily implemented to give a visual representation of the approach to equilibrium, and proved an invaluable aid to timing the cooling and gas entry stages described in the text..

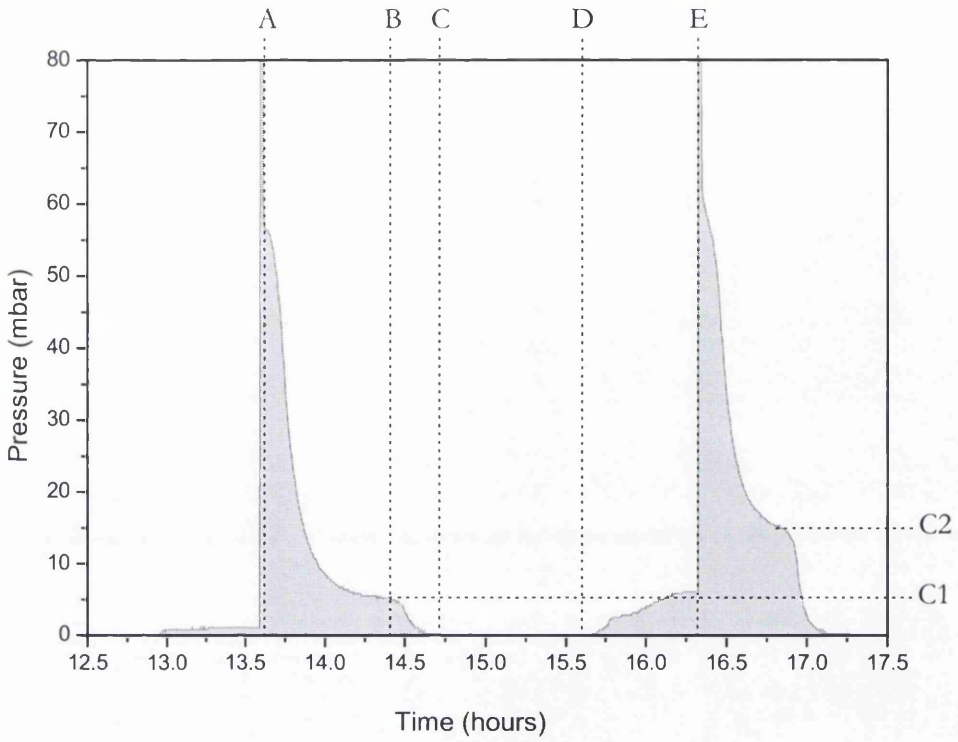

Figure 3.4. *A portion of the 'pressure log' recorded during one of the Xe experimental runs. A – E mark each of the five stages that are repeated throughout the measurements (see text for explanation).*

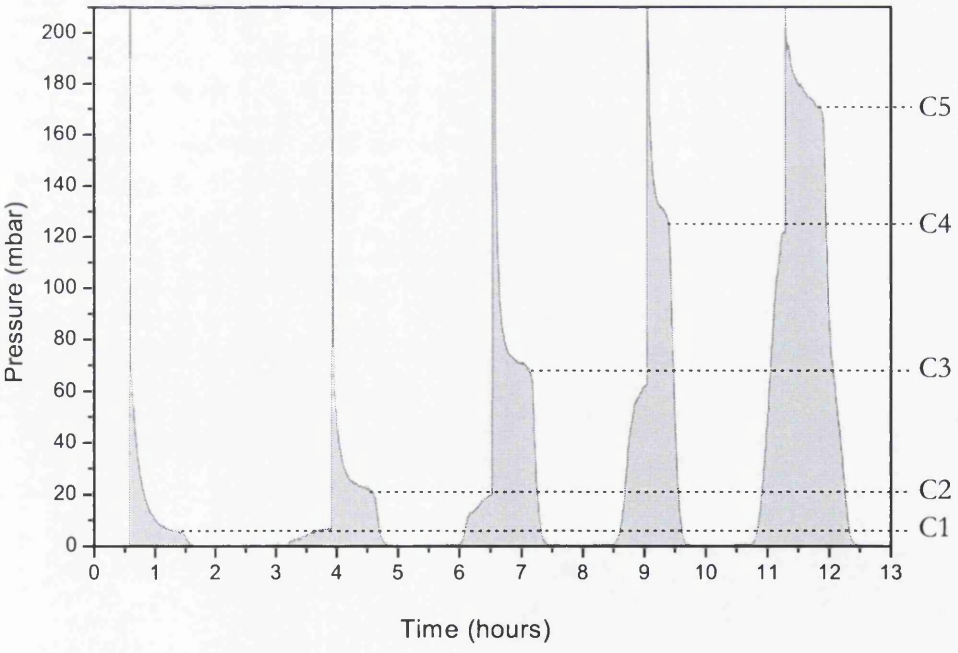

Figure 3.5. *Pressure logs for a series of measurements indicating the five increasing coverage pressures (C1-C5). This is a typical example of the time required for preparation between measurements. In this instance, approximately 13 hours are required for five measurements requiring an average of 40 minutes of beam time each.*

By letting in auxiliary gas up to valve ③ when required, a gas 'sink' is maintained at ~ 1 bar in V_{13} (measured at the transducer in Figure 3.3). Dose volumes[††] are then prepared by allowing the gas through ③ to a typical pressure in V_{34} of 100-500 mbar. We begin with the system in this 'start' condition and the temperature steady at the growth temperature, T_g. Valves ③ and ④ are closed and we proceed according to Table 3.4 at each of the times (A-E) indicated in Figure 3.4.

When coverage has been scanned as far as necessary, which may also be limited by the approach of the equilibration pressure to the saturation pressure of the liquid adsorbate (§ 3.5), the entire system is pumped and heated to remove the gas. The actual temperature for this gas removal was chosen to be suitably high and was applied with regard for the pressure changes seen in the baratron gauges. To remove argon, for example, a temperature of 170 K was applied for approximately 1 hour, within which time the pressure peaked early and then gradually reduced to negligible levels.

[††] It is conventional in adsorption studies (§ 3.5) to consider the specific volume of gas at STP.

Table 3.4. Stages of the experimental process for adsorbed gas measurements.

Time in Figure 3.4	*Actions Taken*
A	Valve ④ is opened and the pressure in V_{34} & V_S is left to equilibrate. This takes roughly 30-45 minutes, with shorter times at higher pressures.
B	When the system is within an acceptable range of equilibrium, pressure C1 (coverage 1) in this example, the temperature is set to the 6 K measurement temperature, freezing the system into its instantaneous state. The supplementary sample heater is turned off only when the read-back temperature at the cold-finger is significantly reduced – the temperature differential through the cryostat is then expected to ensure that most of the remaining gas does not contribute to surface coverage.
C	The system reaches 6 K and the measurement is started. These were typically TF measurements of 15-20 million events (Mevs), taking about 45 minutes.
D	Enough data has been collected. The run is stopped, the sample heater is turned on, and the cryostat temperature is set back to T_g. The pressure may then be left to return to C1; this was done several times to check the equilibrium value obtained, but certain circumstances leading to long equilibration times made this impossible to perform on each occasion. In the case of Figure 3.4, the particular timing of different heating elements has led to an overshoot in pressure.
E[#]	Valve ④ is now closed, pressure is recorded and an additional volume is prepared in V_{34} by allowing gas in from the 'sink', again typically to 100-500 mbar. Once prepared, the system is in the equivalent of the start state again and steps A – E are repeated to build up data at increased coverage, C2, and so on.

[#] Significant time can be saved by performing 'E' directly after the cryostat temperature is set in 'D', and this was done for some of these experiments – notably He. However, one must be aware that in some circumstances (particularly for the higher mass gases) the addition of large volumes of gas into the low temperature system can pose the risk of creating blockages in the tubing near the sample space, and can drastically increase equilibration time. The time was not available in this study to optimise these circumstances for all gases and the period D-E was kept to a reasonable 'cautious' duration.

3.5 Adsorption of Noble Gases

In order to quantify our results in terms of the amount of gas on the powder surface we need to have some understanding of the process of adsorption. Fortunately, adsorption has been studied since the 18th century, when charcoal was found to decolourise solutions by a surface mechanism, and there already exists some very sound and extensive theory on the subject.

3.5.1 Physisorption vs. Chemisorption

When we talk about adsorption (or condensation) of the noble gases (our *adsorbate*), we are referring to physical adsorption, or physisorption, which concerns the weak binding of atoms or molecules to a surface substrate (the *adsorbent*). Physisorption can be considered analogous to van der Waals bonding in solids, with the adatom subject to a dipole-dipole interaction with the surface. This attraction to the surface is weak but long-ranged and the energy released upon accommodation to the surface, i.e. the enthalpy of condensation, is characteristically of order 20 kJ mol^{-1} (~2 eV).

In contrast, chemisorption is ambiguously defined in terms of extra bonding strength (enthalpy of condensation is generally around 40 kJ mol^{-1} and above) but for the sake of this work may be considered simply analogous to chemical bonding.

3.5.2 Adsorption Isotherms

In a system at a given temperature, the free gas and the adsorbed gas are in dynamic equilibrium. The chemical potential of the bound adsorbate, dependent on the fractional coverage of the surface, is then equal to the chemical potential of the free adsorbate, dependent on the gas pressure. The variation of coverage, θ, with pressure, p, at a given temperature, T, is called the *adsorption isotherm.*

Several models have been developed to understand the process of adsorption and to obtain

information on factors such as specific surface area of porous materials, as well as the energetics involved in the capture and loss of various molecules at the surface. These are important properties for potential catalytic materials.

3.5.3 The Langmuir Isotherm

The simplest of isotherm models was developed by Langmuir in 1916-18 [3.13]. Its simplicity lies in the following assumptions:

I. All adsorption sites are equivalent and the surface is uniform.

II. The ability of a molecule/atom to adsorb is independent of the occupation of neighbouring sites.

III. The adsorption process cannot proceed beyond monolayer coverage.

This isotherm is most appropriate for chemisorption and some special cases of physisorption, but serves as a basis for our understanding.

For an adsorbate A on a free surface S, and with AS signifying the bound adsorbate, we consider the dynamic equilibrium

$$A(\text{gas}) + S(\text{surface}) \Leftrightarrow AS(\text{surface}). \tag{3.1}$$

Given that the fractional coverage is θ, then the total number of vacant sites is $N(1-\theta)$, where N is the total number of sites. The rate of adsorption is proportional to the partial pressure p of A(gas) and the number of sites available on the surface,

$$\frac{\mathrm{d}\theta}{\mathrm{d}t} = k_a pN(1-\theta). \tag{3.2}$$

The rate of desorption is proportional to the number of sites occupied,

$$\frac{\mathrm{d}\theta}{\mathrm{d}t} = -k_d N\theta, \tag{3.3}$$

where k_a and k_d are the constants of adsorption and desorption respectively. At equilibrium

we obtain the Langmuir equation,

$$\theta = \frac{\kappa p}{1+\kappa p} \qquad \text{where } \kappa = \frac{k_a}{k_d}. \tag{3.4}$$

In terms of measured values, we may write $\theta = \frac{V}{V_{mon}}$ where V is the volume of adsorbed atoms (measured at STP) and V_{mon} is the maximum uptake (i.e. one monolayer, also in terms of volume at STP)[§§]. With this substitution one may rearrange equation (3.4) and plot p/V vs. p according to

$$\frac{p}{V} = \frac{p}{V_{mon}} + \frac{1}{V_{mon}\kappa}, \tag{3.5}$$

to calculate the maximum uptake V_{mon} and ratio of coefficients κ from a straight line graph.

3.5.4 The BET Isotherm

The Langmuir isotherm is not strictly applicable to our noble gas/ silica powder systems, where the initial overlayer may act as a substrate for further physisorption, and the isotherm is expected to rise indefinitely instead of levelling off to a saturated value at high pressures. The BET isotherm, named after Brunauer, Emmett and Teller [3.14], accounts for further layers by building the following additional assumptions on to the Langmuir model:

III. Multiple layers form and the Langmuir model applies to each layer (i.e. assumptions I and II).

IV. Evaporation (desorption) only occurs from exposed surfaces.

V. Enthalpy of desorption ΔH_{des} for the first layer has a value determined by the properties of the surface and adsorbate and is independent of surface coverage.

VI. For all subsequent layers ΔH_{des} is equal to the enthalpy of vaporization, ΔH_{vap}.

---

§§ One could, of course, use the more direct value of atom numbers instead of volumes, but here we stick with the conventional terms.

With the possible existence of multiple layers, we may now define $\theta_0, \theta_1, \ldots, \theta_n$ = surface area covered by 0,1,…,*n* layers, such that the total surface area,

$$A = \sum_{i=0}^{\infty} \theta_i \,. \tag{3.6}$$

Considering first the free surface area, θ_0, we proceed as in the Langmuir derivation and look at the equilibrium case where θ_0 must remain constant. We must then balance the increase in θ_0, due to evaporation from the 1st layer, with the decrease in θ_0, due to condensation onto the free surface. This may be written as

$$k_{-1}\theta_1 = k_1 p \theta_0 , \tag{3.7}$$

where k_{-1} and k_1 are the constants of desorption and adsorption strictly appropriate to the 1st monolayer. This expression is equivalent to equating equations (3.2) and (3.3) in the Langmuir case, and is in line with assumption III.

We may apply the same considerations to θ_1, where the increase in θ_1 is due to evaporation from the 2nd layer *or* condensation onto the free surface, and the decrease in θ_1 is due to condensation onto the 1st layer *or* evaporation of the 1st layer. This follows from assumption IV and may be written as

$$k_1 p \theta_0 + k_{-2}\theta_2 = k_2 p \theta_1 + k_{-1}\theta_1 ,$$

thus from equation (3.7),

$$k_{-2}\theta_2 = k_2 p \theta_1 \,. \tag{3.8}$$

For all subsequent layers, similar arguments may be applied to give in general

$$k_{-i}\theta_i = k_i p\theta_{i-1}. \tag{3.9}$$

Now, from equation (3.7) we may write

$$\theta_1 = \left[\frac{k_1}{k_{-1}}p\right]\theta_0 = y\theta_0 \quad \text{where } y = \frac{k_1}{k_{-1}}p. \tag{3.10}$$

From assumptions V and VI we see that

$$\frac{k_{-2}}{k_2} = \frac{k_{-3}}{k_3} = \cdots = \frac{k_{-n}}{k_n} = g \text{ (constant)}. \tag{3.11}$$

Defining $z = \frac{p}{g}$ it can then be shown generally (for $i = 2$ to n) that

$$\theta_i = z\theta_{i-1} = z^{i-1}\theta_1 = z^{i-1}y\theta_0 = cz^i\theta_0 \qquad \text{where } c = \frac{y}{z}, \tag{3.12}$$

c is thus a constant which is large when the enthalpy of desorption is large compared with the enthalpy of vaporisation of the liquid adsorbate:

$$c = \frac{k_1/k_{-1}}{k_i/k_{-i}} \propto e^{(\Delta H_{des} - \Delta H_{vap})/RT}, \tag{3.13}$$

where R is the molar gas constant and T is temperature.

We may now define the total volume adsorbed

$$V = V_0 \sum_{i=0}^{\infty} i\theta_i, \tag{3.14}$$

where V_0 is the volume of gas required to cover unit area with a thickness of one

monolayer.

Expressing the volume of adsorbed gas as a fraction (denoted θ as in the Langmuir case) of the volume required to totally cover the free surface, using definitions given in equations (3.6) and (3.14),

$$\theta = \frac{V}{V_{mon}} = \frac{V}{AV_0} = \frac{\sum_{i=0}^{\infty} i\theta_i}{\sum_{i=0}^{\infty} \theta_i}. \tag{3.15}$$

Since $$\sum_{i=0}^{\infty} i\theta_i = c\theta_0 \sum_{i=1}^{\infty} iz^i = c\theta_0 z \frac{d}{dz} \sum_{i=1}^{\infty} z^i, \tag{3.16}$$

and $$\sum_{i=0}^{\infty} \theta_i = \theta_0 \left(1 + c \sum_{i=1}^{\infty} z^i \right), \tag{3.17}$$

and the sum of an infinite geometric progression may be written as $\sum_{i=1}^{\infty} x^i = \frac{x}{1-x}$, we may manipulate equation (3.15) to arrive at the BET isotherm described by the equation

$$\theta = \frac{V}{V_{mon}} = \frac{cz}{(1-z)(1-z+cz)} \qquad \text{where } z = \frac{p}{p_{vap}}. \tag{3.18}$$

In order to allow an infinite number of adsorbate layers, g has been set equal to p_{vap}, where p_{vap} is the vapour pressure above a layer of adsorbate that is more than one layer thick and resembles a pure bulk liquid (i.e. the saturation pressure).

For $p << p_{vap}$ equation (3.18) reduces to

$$\theta = \frac{cz}{1+cz}, \tag{3.19}$$

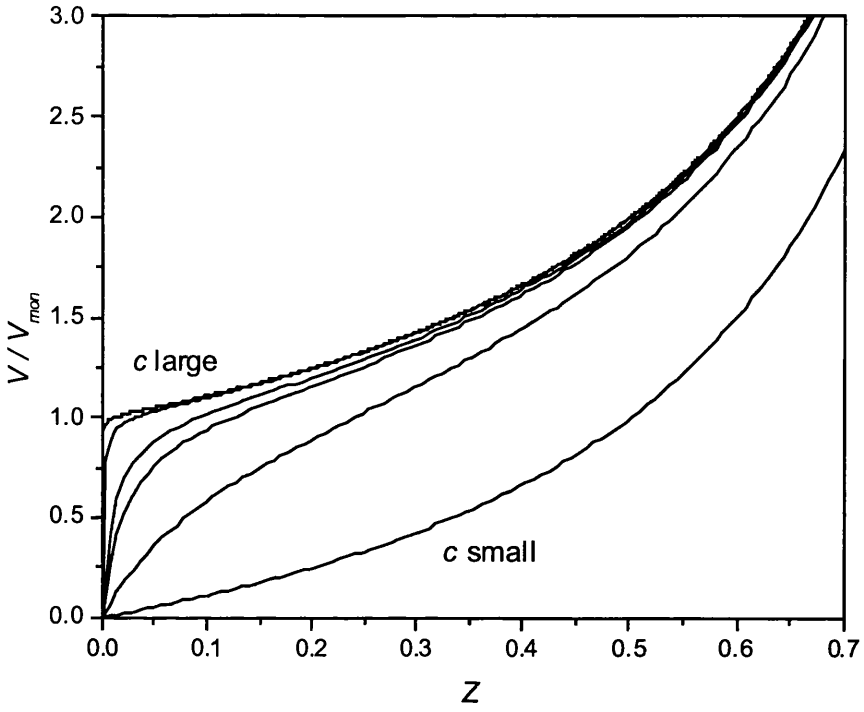

Figure 3.6. *The form of the BET isotherm. Values of c from right to left are: 1,10,50,10^2,10^3,10^4. For very large c, $\theta \approx 1/(1-z)$. Further explanation of the c-parameter is given in § 3.5.5.*

which is a special form of the Langmuir equation. At higher pressures, V (i.e. θ) becomes large and the curve becomes convex to the pressure axis. The form of this isotherm for various c values is illustrated in Figure 3.6.

As was the case with the Langmuir isotherm, a straight-line graph can be created by reorganising equation (3.18) into

$$\frac{z}{(1-z)V} = \frac{(c-1)z}{cV_{mon}} + \frac{1}{cV_{mon}}, \tag{3.20}$$

and the parameters V_{mon} and c may be calculated from the slope and intercept when the expression on the left is plotted against z.

3.5.5 Gas Coverage Calibration: He, Ar, Kr and Xe on Cab-O-Sil®

Isotherm measurements for each gas were taken with the gas handling system set up on the experimental beam line. Ideally these would have been performed exhaustively off-line, but limited access to the system meant that only preliminary tests could be made and that the bulk of these data were collected during the muon beam time. The basic thermodynamic properties of the gases are given in Table 3.3 and this information was used in conjunction with the vapour pressure curves, and simple trial-and-error measurements, in order to establish appropriate gas coverage and measurement conditions.

Helium is the most "well behaved" of the gases studied. It has high vapour pressure even at the very low measurement temperature of 5-6 K and coverage of more than one monolayer is not expected, it nevertheless adsorbs readily onto SiO_2 (as is evident from the clear step structure of the raw isotherm in Figure 3.8). Helium on SiO_2 consequently has a high c value of 3500(500) under these conditions, and all of the measurements were completed at very low z, meaning that the isotherm obtained is almost Langmuir-like.

For the more massive gases, their high sensitivity to growth temperature means greater difficulty in finding a balance that most closely matches the assumptions of the isotherm model[***]; if the temperature is too low there is no distinction at monolayer coverage (the gas sticks to itself readily allowing additional layers to form before the first is complete); if it is too high only a small fraction of the gas is adsorbed (the isotherm then tells us little about the condition of the surfaces when cooled to the measurement temperature).

There are distinct modes of growth for film layers on an adsorbent. The two extreme forms relevant at very low coverage are Frank-van der Merwe, or layer-by-layer growth, dominated by the adsorbate-substrate interaction, and Vollmer-Weber, or island growth,

[***] In a real system, of course, one should remember that c probably has some coverage dependence since the enthalpy of desorption may change if all sites are not equivalent and the adatoms occupy energetically favourable sites first.

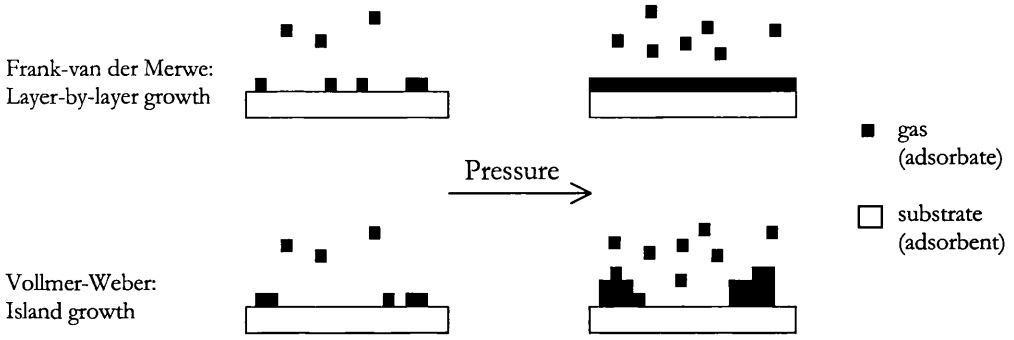

Figure 3.7. *Model of growth modes for film layers on an adsorbent.*

dominated by the adsorbate-adsorbate interaction. These growth modes are shown schematically in Figure 3.7. They are often referred to as *wetting* and *non-wetting* of the substrate and represent respectively the liquid and solid phases of the adsorbate on the powder surface. Ideally one wishes to maximise the fraction of introduced gas adsorbed onto the powder where the growth mode follows the process of complete wetting, which leads to an isotherm with an optimal value of c[†††].

As mentioned, the choice of isotherm/growth temperature used for each gas is to some degree a matter of trial and error. Vapour pressure curves (Appendix I) were used to select a temperature giving a vapour pressure of the order of 1000 mbar as a starting point, and the success of the temperatures used in this study may be gauged from the fits of Figure 3.9 and Figure 3.11, where the data is displayed in the most relevant format.

The adsorption measurements are shown in various forms in the figures that follow. Figure 3.8 shows the measurements for each gas in their 'raw' form with the ordinate giving the pressure in the dose volume; this is not linearly related to the adsorbed volume, which has an additional dependence on the equilibrium pressure.

††† The extent of wetting is indicated by the value of the c parameter in the BET isotherm, where lower c values indicate increasing Vollmer-Weber type growth.

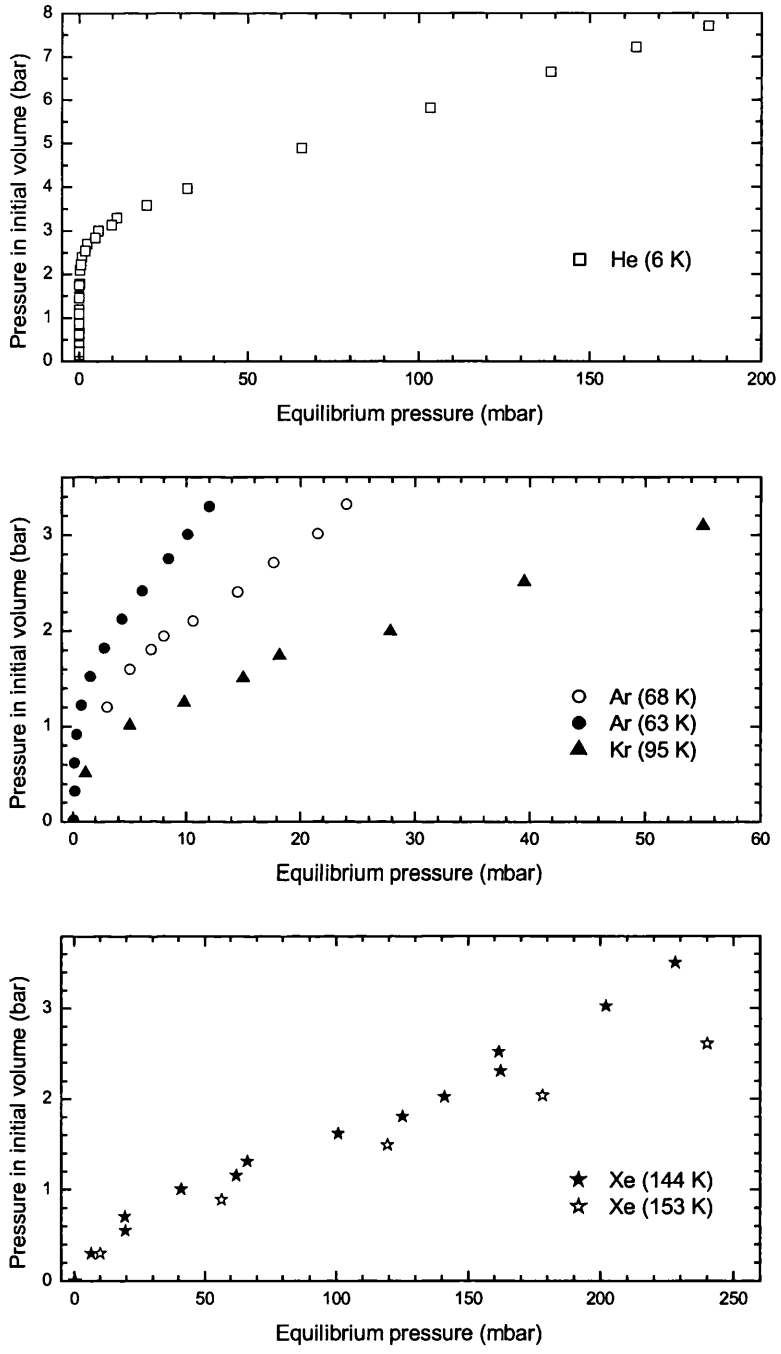

Figure 3.8. *Measured isotherm data for each gas; He (squares); Ar (circles); Kr (triangles); Xe (stars). Open and closed symbols show multiple datasets taken for the same gas at different temperatures. Discontinuities in the 144 K Xe dataset are attributed to an increase in temperature of a few K during the experimental run.*

The sensitivity to temperature is quite clear from the graphs of Ar and Xe, which show multiple isotherms – The 144 K isotherm for Xe also contains a discontinuity, which was tracked down to a temperature increase of a few degrees during some of the intermediate measurements. The faint data points for Ar at 68 K are measurements where equilibrium was not reached due to the need to take muon data. This introduced negligible error in the desired surface coverage but the isotherm (of secondary importance) was strongly affected and these points have been left out of the analysis.

Figure 3.9 show these data re-plotted once the adsorbed volume has been calculated assuming ideal gas conditions and using

$$V_{ads} = \frac{n_{ads} kT}{p} \text{ at S.T.P., where } n_{ads} = \frac{p_0 V_0}{kT_0} - \frac{p_{eq}}{k}\left(\frac{V_{RT}}{T_{RT}} + \frac{V_{GT}}{T_{GT}}\right). \qquad (3.21)$$

The '0' subscript indicates a property of the total dose volume (V_0 = 14.6(3) cm^3) at each point, 'RT' and 'GT' subscripts refer to division of the sample space into an effective room temperature and growth temperature volume respectively. Estimates for these relative sample spaces are based primarily on the He data as it becomes almost linear in Figure 3.8, where adsorption is assumed to cease, meaning that additional gas contributes only to pressure. This implies values of V_{RT} = 43.2(10) cm^3 and V_{GT} = 6.4(10) cm^3, and over-estimates in the error are made for the other gases based on the cryostat down-tube (approximately 7 cm^3) being at base temperature rather than room temperature, meaning less gas adsorbed on the powder than is apparent. These possible systematic errors are included on the fitting graphs (Figure 3.9) and are only significant for Kr and particularly Xe due to the higher growth temperatures. These data have been fitted using the full expansion of the BET equation (3.18) to allow adjustment of V_{mon} and p_{vap}. Multiple data sets proved very useful in determining p_{vap} values as V_{mon} is a common parameter,

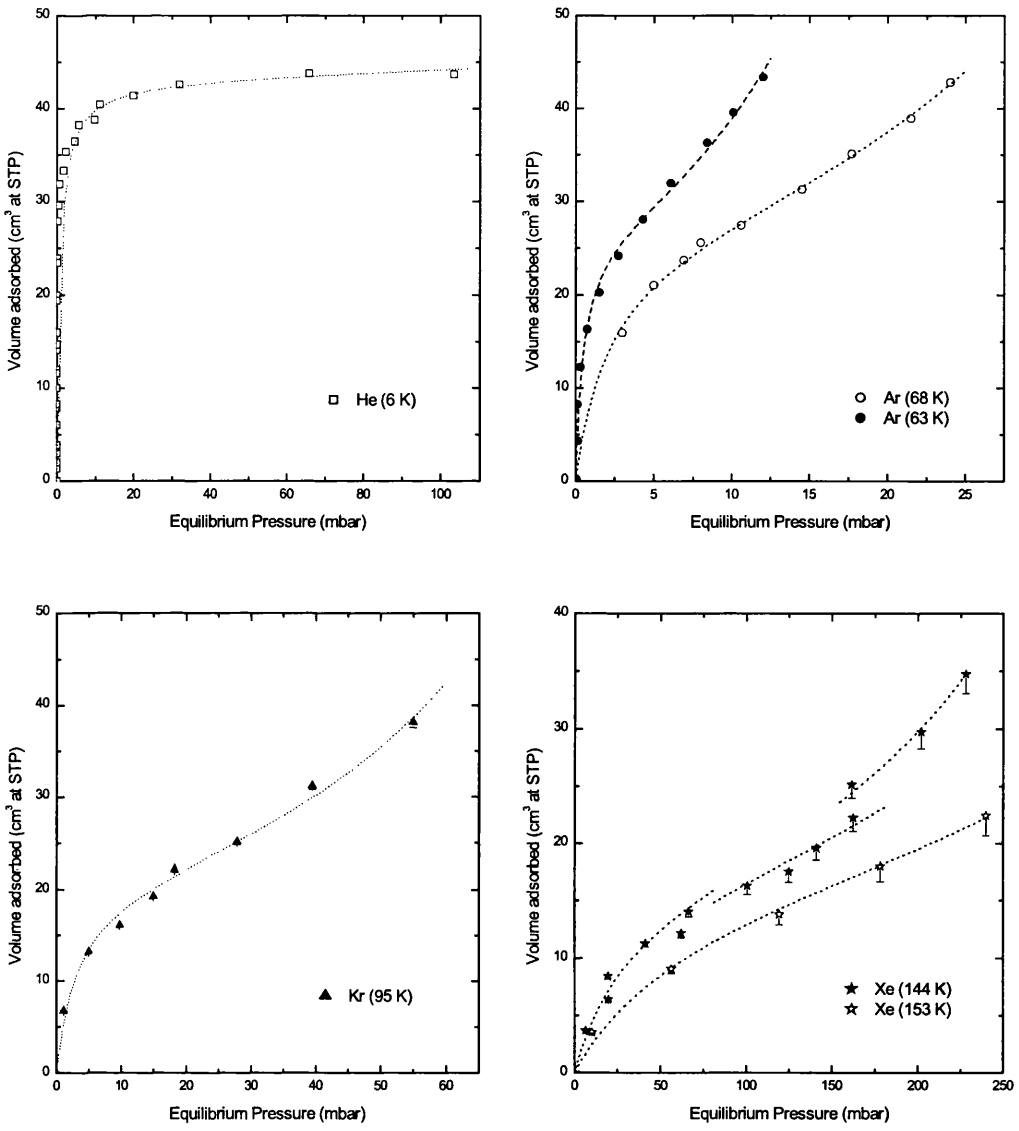

Figure 3.9. *Measured data of Figure 3.8 adjusted to adsorbed volume using equation* (3.21). *Curves show the best fits to the data based on the BET theory, equation* (3.18), *giving the parameters in Table 3.5. Fitting was carried out simultaneously where multiple datasets existed for a given gas.*

independent of temperature. The temperature increase during the 144 K Xe run is quite clearly defined.

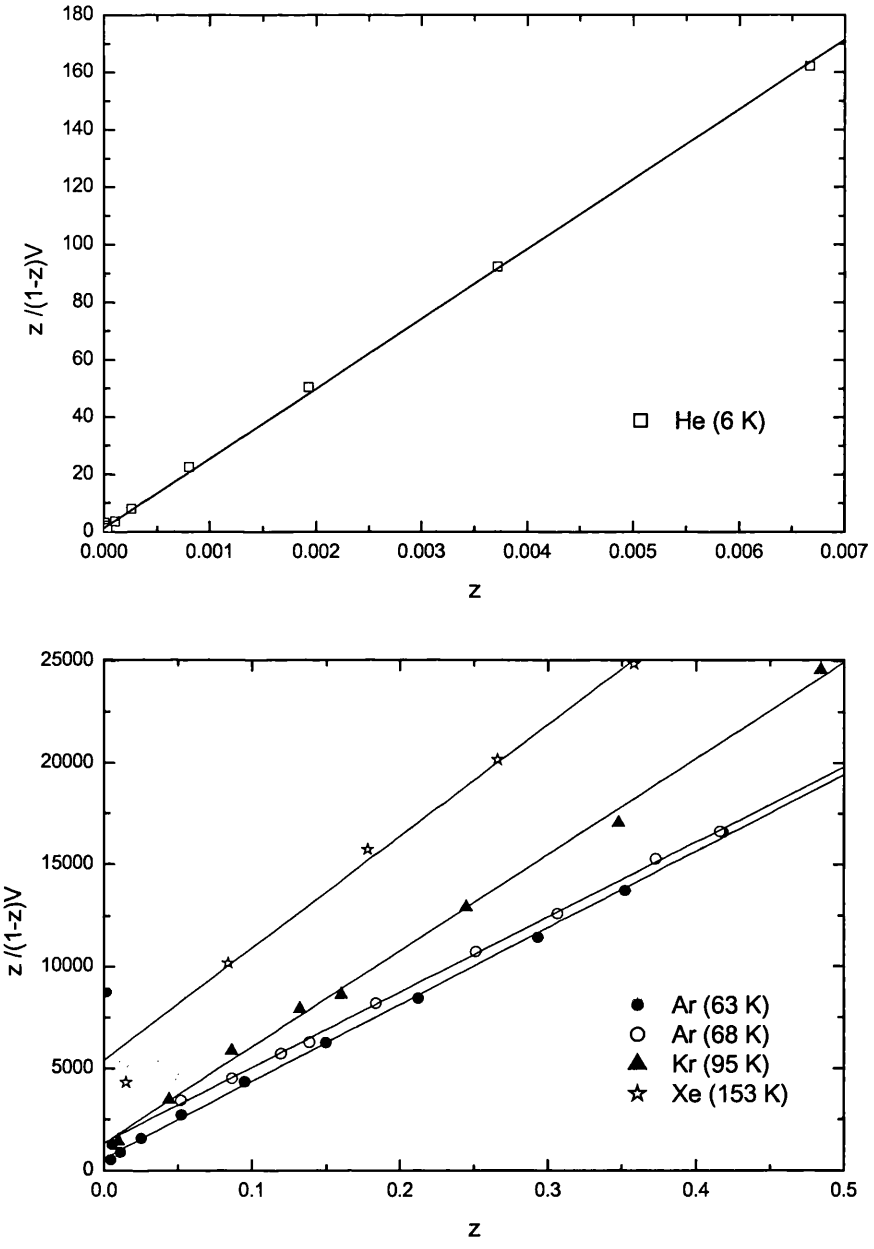

Figure 3.10. *BET analysis plots for all four gases; He (squares); Ar (circles); Kr (triangles); Xe (stars). Both Ar datasets are shown. Only one Xe data set shown for clarity. This is the typical analysis method for fewer unknowns. The close linear fit for all datasets is a sign of the accuracy of all three fit parameters.*

The results of the isotherm fits were verified against conventional linear BET analysis plots (Figure 3.10) with the straight lines given by inserting the fit parameters into

Table 3.5. Fit parameters obtained from BET analysis. Uncertainties are shown only where the attributes were free parameters in the model.

Gas	Temp (K)	p_{vap} (mbar)	c	V_{mon} (cm^3 at S.T.P.)	atoms/nm^2*
He	6	3000	3500(489)	43(4)	6.5(8)
Ar	63 68	28.7(18) 58(3)	62(6) 28(4)	26.1(9)	3.9(4)
Kr	95	114(8)	36(7)	20.6(12)	3.1(3)
Xe	144 153	414(25) 670(70)	14(3) 11.1(19)	16.6(11)	2.5(3)

*based on powder sample with a total area of 175(15) m^2.

equation (3.20). It is notable that there are several anomalies at low z – again a result of the isotherm measurements taking second priority – errors are avoided by concentrating on the accurate fits to the isotherm curves. The points towards higher z, where its rate of change with surface coverage is smaller, do exhibit a very good linear fit for all gases. The fit parameters are summarised in Table 3.5.

The nominal area of the powder is taken to be 175(15) m^2, using the specific surface area of Cab-O-Sil® given in Table 3.1. One may then examine the increase in the comparable area of coverage per atom as the atomic dimensions are increased. An understanding of the 2-D gas structure would be beneficial, but is beyond the scope of this work. Nevertheless, commensurate layers are perhaps unexpected on an amorphous surface, and we might expect the atomic distances to be of order of crystal unit cell. Table 3.6 shows such a comparison, based on gas atoms arranged in a hexagonal close-packed layer, and illustrates a remarkable agreement with lattice dimensions of the cubic close-packed bulk. We take this as both confirmation of the assumed distribution and endorsement of our calculated results for the V_{mon} of each gas.

Table 3.6. Relationship of the calculated interatomic spacing for 2-D gases on Cab-O-Sil® to the lattice constant of the bulk RGS.

Gas	Interatomic spacing, d* (nm)	Lattice constant, a** (nm)	d/a
He	0.42(3)	0.424	0.99(6)
Ar	0.54(3)	0.526	1.04(5)
Kr	0.61(3)	0.571	1.07(5)
Xe	0.68(3)	0.620	1.10(4)

* assuming a hexagonal close-packed arrangement, so that the area occupied by 1 atom = $d^2 \frac{\sqrt{3}}{2}$.

** cubic close packed structure in bulk solid from [3.15].

Finally the results are collected together in Figure 3.11 where the adsorbed volume is normalised with V_{mon} to give the fractional surface coverage. V_{mon} is used in this way to calibrate the surface coverage for all the following gas-coverage-dependent muon results.

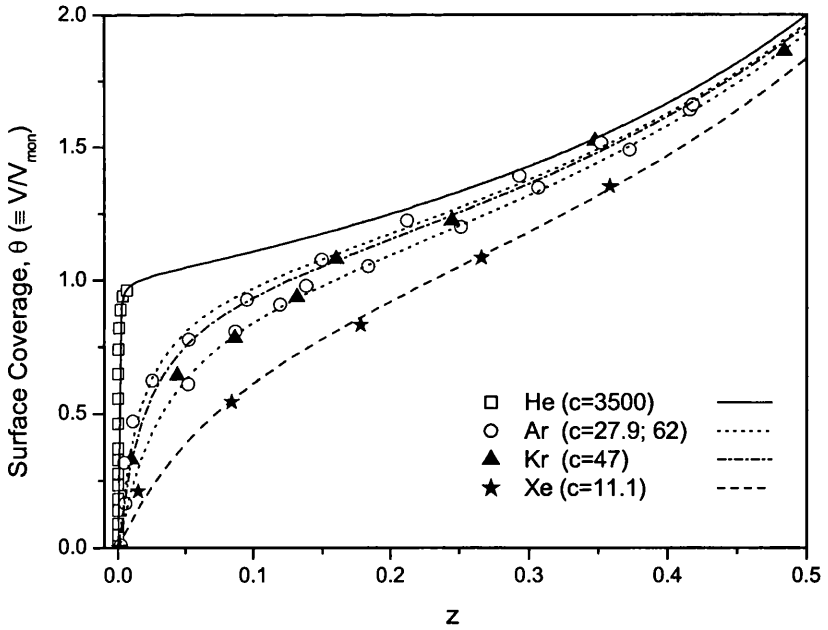

Figure 3.11. *Classic BET isotherm (cf. Figure 3.6) containing data for all of the gases. Lines are drawn at the respective c values gained from analysis.*

3.6 Muon Results & Discussion

As a guide to the integrity of the sample, Figure 3.12.a shows the temperature dependent relaxation rate of the compacted Cab-O-Sil® under vacuum compared with Harshmans' measurements for samples baked at 110 °C and 600 °C (to give different hydroxyl concentrations). It is clear that our sample has higher relaxation rate at low temperatures, but does not contain the obvious 'trapping peak' of Harshmans' samples. This appears to follow the trend of Harshmans' data towards higher hydroxyl concentrations. Harshman notes that relaxation at the trap site is completely neutralised by a small platinum loading (~0.01% Pt), which is responsible for a significant quantity of atomic hydrogen, dissociated by the catalyst during the production of the loaded samples. He therefore suggested that the traps be attributed to the presence of paramagnetic Fe^{3+} ions in the nominally pure sample, which are reduced to metallic iron by the atomic hydrogen (i.e. H atoms occupy the traps).

In Figure 3.12.b we expand the studied temperature range, by including data for a similar sample in a "sealed" cell from a related, unpublished study [3.16], and discover a feature that has not been previously noted. The gas cell results are shown as solid circles and appear to follow simple motional narrowing towards high temperatures. The sealed cell results, however, display a clear peak around 100 K with width ~25 K in a region not investigated (between the 64 and 153 K growth temperatures for Ar and Xe) with the gas cell. It is not possible without further investigation to either exclude the peak as a peculiar artefact of the sealed cell sample (and its impurities), or include it as a feature of the temperature dependence of Mu relaxation in bare Cab-O-Sil®. In any case, it implies that Mu still has very significant contact with the powder surface at 100 K. It is worth noting that the sealed cell results also show no sign of the lower-temperature 'trapping' peaks seen in Harshmans' work at around 25 K.

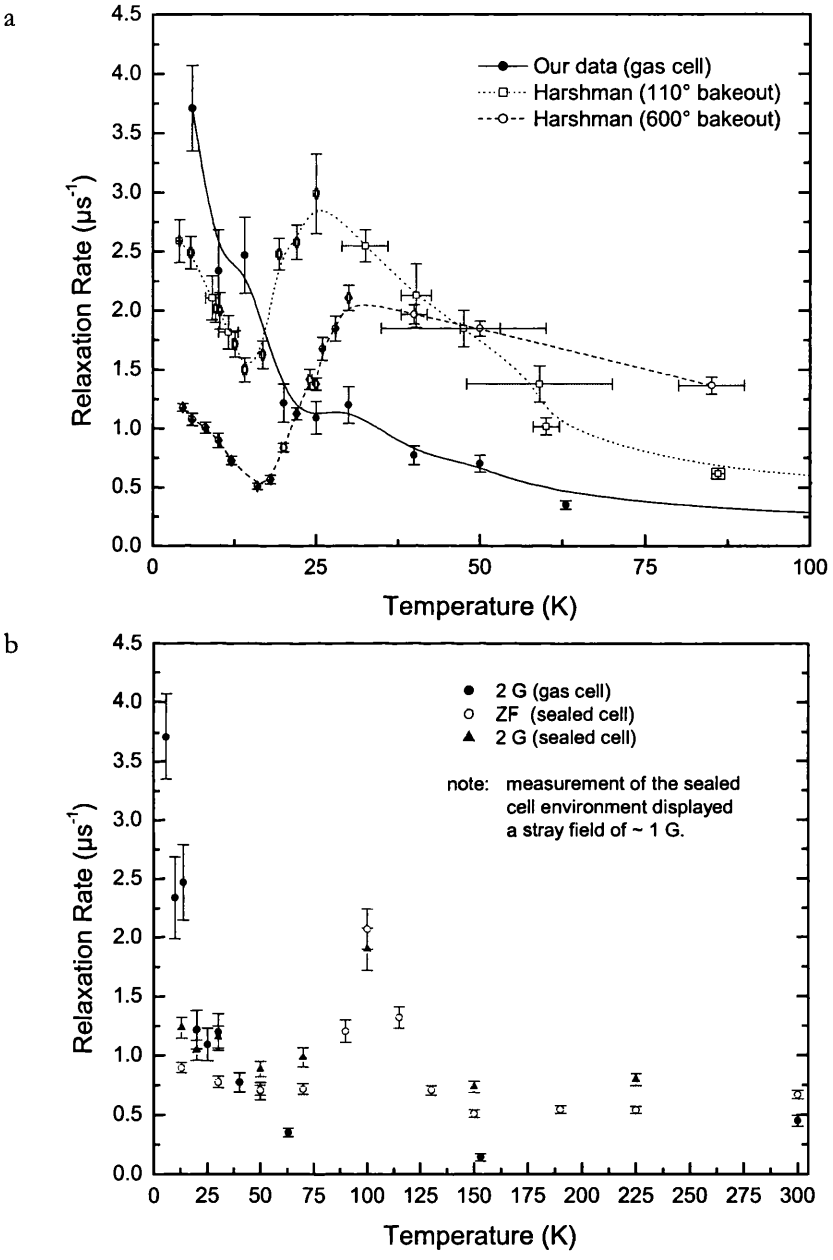

Figure 3.12. *Temperature dependent relaxation rate of muonium in the bare Cab-O-Sil® sample under vacuum.* a. *Comparison between Harshmans' samples and our own. Lines are shown to guide the eye and distinguish datasets.* b. *Extended temperature scale showing relaxation peak around 100 K.*

a

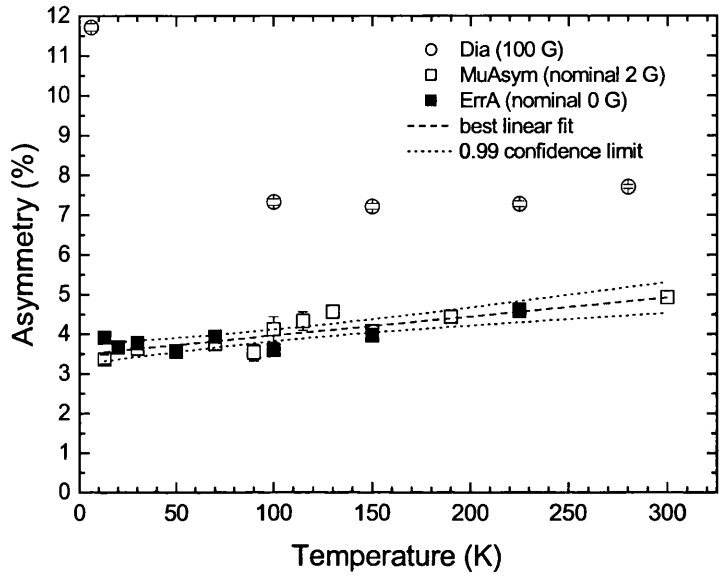

b

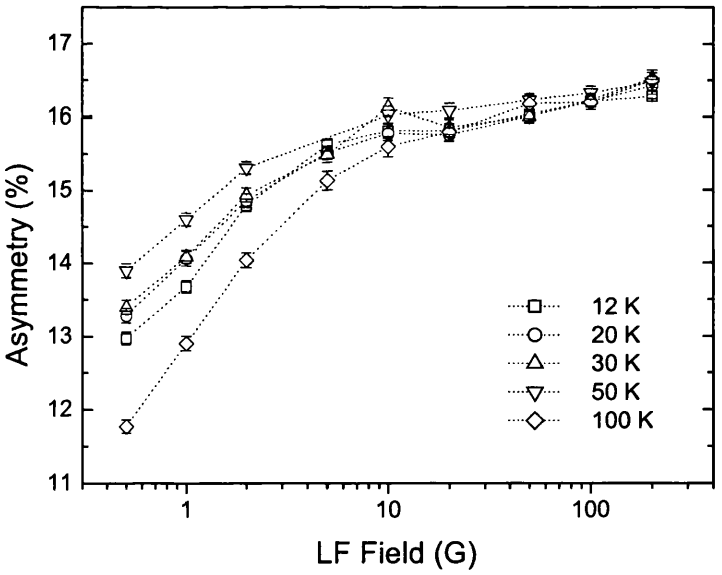

Figure 3.13.a. *Temperature dependence of the diamagnetic and paramagnetic TF asymmetry for the bare Cab-O-Sil® powder. Ag calibration asymmetry = 20.24 %.* b. *Low-field repolarisation curves (LF) for bare Cab-O-Sil® at a variety of temperatures. The drop in asymmetry as the applied field is reduced is indicative of an asymmetric hyperfine interaction, which leads to lifting of the degeneracy of the muonium spin-states at zero field.*

Figure 3.13.a shows TF diamagnetic and paramagnetic asymmetry across the temperature range, and a family of low LF repolarisation curves at different temperatures; all "sealed cell" data from the unpublished study. At 6 K all muons in the sample are accounted for in the diamagnetic and paramagnetic signals; corresponding to ~40% muonium fraction and ~60% μ^+. By 100 K, and above, there is a missing fraction of ~25%, as muons are lost in the diamagnetic signal. The muonium fraction, meanwhile, appears to increase monotonically by about 5-10% over the temperature range.

The low-field repolarisation (Figure 3.13.b) is characteristic of an asymmetric hyperfine interaction [3.17], when the zero-field degeneracy of the muonium spin-states is lifted (see for example Figure 4.3). There is a clear reduction in asymmetry[##] as the temperature is increased and muonium begins to leave the surface, with a dramatic reverse to maximum asymmetry corresponding to the peak in relaxation rate at 100 K.

As mentioned in § 3.2.2, these temperature dependent muonium results indicate that formation cross-section is at least partly reliant on the surface dynamics of the muon (and possibly also the dynamics of any active sites/impurities).

We now turn our discussion to changes in the μSR characteristics with the addition of noble gas adsorbates. These measurements are all taken at low temperature, where the muons are assumed static on the powder surface, and there is no missing fraction. Figure 3.14 shows the relaxation rate as a function of gas coverage for all four gases. Each gas causes a significant drop in rate from an initial value of ~3.5 μs^{-1} to values typically below 0.5 μs^{-1} for coverages approaching 1 monolayer. In the case of helium, the rate drops as low as 0.05 μs^{-1}. In the case of Xe, significant relaxation is still present. We attribute this to the nuclear moments of Xe, which are known to contribute to

[##] It is difficult to draw quantitative conclusions here as repolarisation curves for the orientationally averaged hyperfine interaction (for a powder sample) must be calculated numerically, and would also be complicated by fast spin relaxation and/or the presence of nuclear moments.

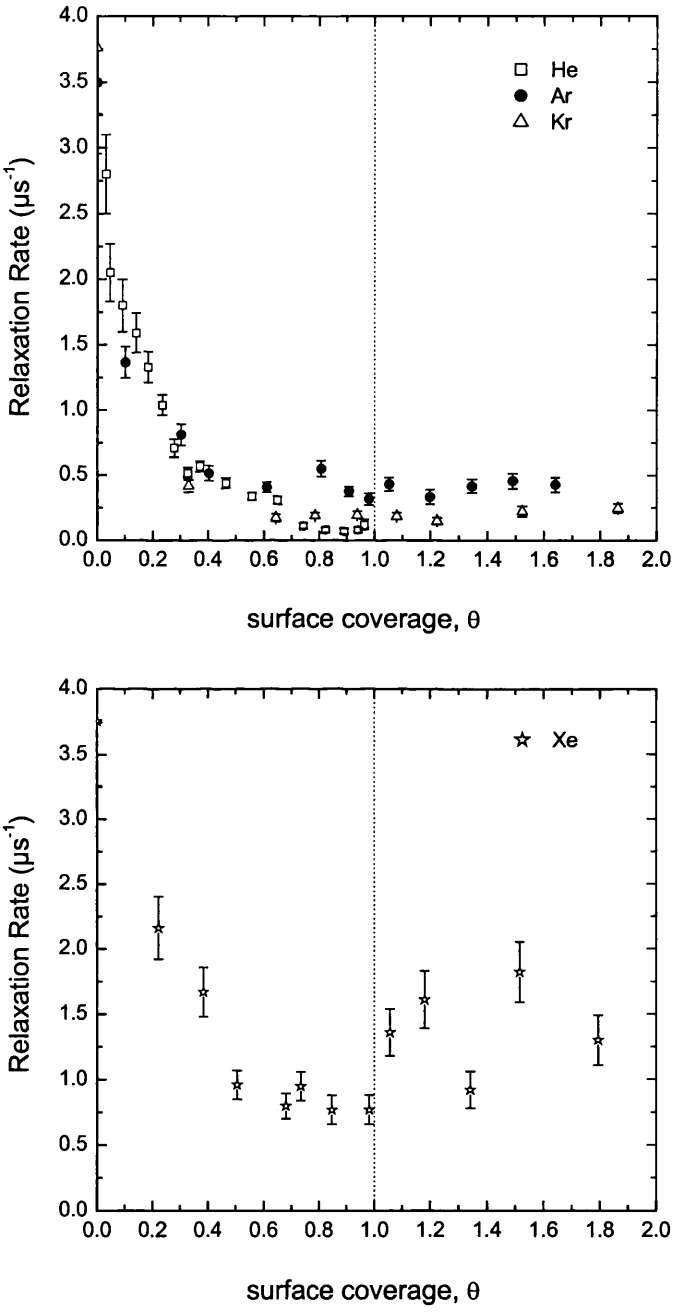

Figure 3.14. *Relaxation rates for all four gas adsorbates on Cab-O-Sil® as a function of coverage.*

depolarisation; the relaxation rate has been shown to be 19(2) μs^{-1} in solid Xe and 2.1(2) μs^{-1} in liquid Xe [3.18]. The general trend in relaxation is a decrease with increasing gas coverage as the probability of a muonium atom interacting with the bare powder surface is reduced.

As the muonium relaxation rate in bulk SiO_2 is known to be 3.3 μs [3.11], the relaxation rate with gas present allows a limit to be established for time spent *within* the powder grains - i.e. the minimum fractional relaxation rate, $\lambda_{gas}/\lambda_{bulk}$ (for *any* coverage at a given temperature), may be interpreted as the maximum fractional time spent by Mu within the bulk. In order to make inferences on the nature of the pure powder (i.e. extending to zero coverage) like this, there is an implicit assumption here that the addition of a noble gas adsorbate serves only to alter the nature of depolarisation centres, rather than the muon dynamics between bulk and surface and the relative muonium fractions therein.

Accordingly, the relaxation rate at high coverage (particularly when looking at He results) implies a maximum of a few percent of time spent by muonium in the bulk. In addition, low coverage results imply significant time spent in contact with either the surface or the bulk of the material, i.e. it does not escape to the extragranular region. These results confirm that muonium spends most of its life on the surface of the powder at this temperature; the "coincidence" in the amplitude of the relaxation rates for bulk SiO_2 and pure Cab-O-Sil® at 6 K appears to be just that. This means that the relaxation rate at zero coverage may be a combination of the depolarising action of the RAHD, in the vicinity of the hydroxyl protons (as discussed in § 3.2.2), and a consequence of the muonium formation process.

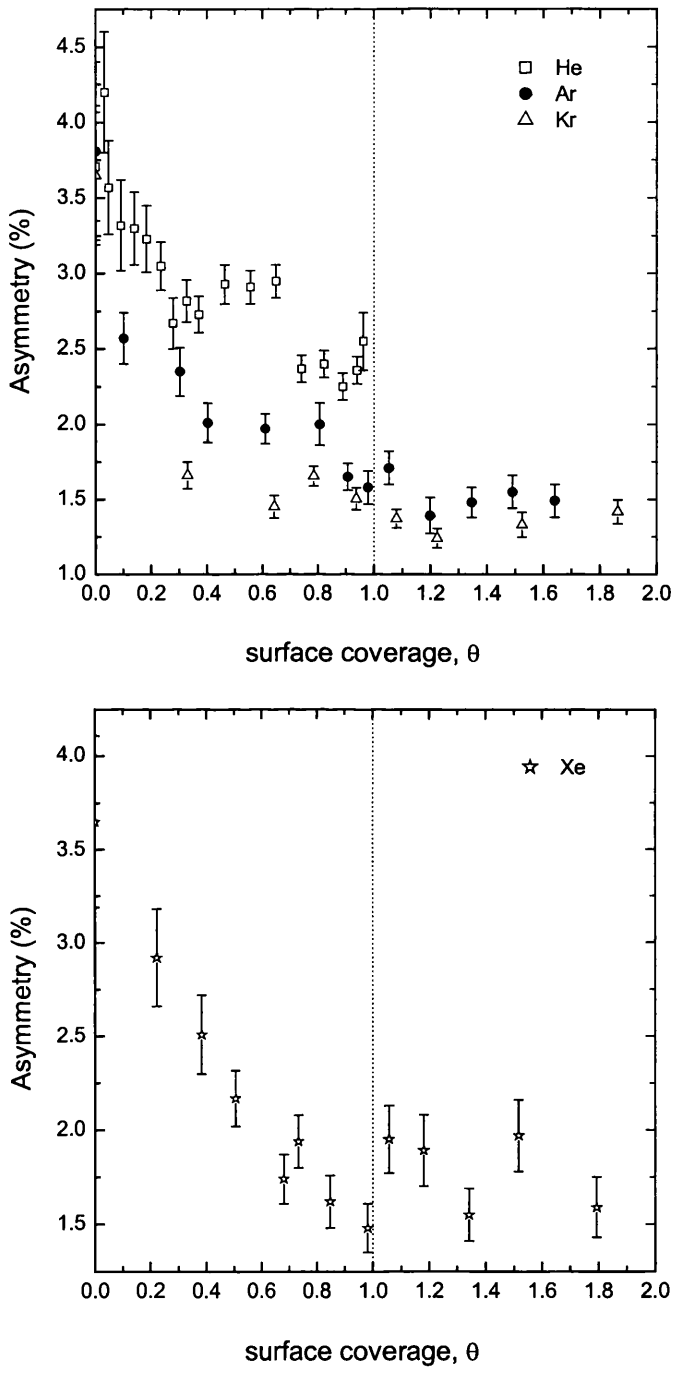

Figure 3.15. *Paramagnetic asymmetry for all four gas adsorbates on Cab-O-Sil® as a function of coverage.*

We examine the concurrent asymmetry results (Figure 3.15) in terms of the effect on the muonium fraction expected as a result of the surface formation mechanisms suggested by Harshman's work (§ 3.2.2). We wish to distinguish between a passive interaction, where the gas atoms simply cover up the surface, impairing formation, and a more active interaction, where gas ions might capture the electrons of newly formed muonium atoms.

Immediately, the similar fall in asymmetry due to coverage between He and Xe contradicts the e^- scavenging/stripping hypothesis, which does not allow a drop in the Xe data (due to its low electron affinity) and should also yield lower drops in the mid-range gases. We instead interpret the fall as a response to coverage of the sites at which Mu is formed on the surface. The faster than linear drop-off with coverage then indicates that the gas coverage occurs preferentially at sites where the Mu is formed.

The diamagnetic fraction was also measured as a function of the He coverage (Figure 3.16). It shows no increase (corresponding to the decrease in paramagnetic asymmetry) until the helium approaches monolayer coverage, and therefore reveals a large missing fraction in the mid-coverage region. As a characteristic of delayed muonium formation, this is in line with the passive model.

Combining these results, our knowledge of the system is as follows:

A finite muonium fraction (approximately $\frac{1}{3}$ of the paramagnetic asymmetry of the bare powder) remains at all coverages, for all gases investigated. This may represent muonium that is formed within the bulk of the powder grains, and is unaffected by surface conditions.

As the coverage is increased from zero, the missing fraction indicates that muons take longer to reach an active site and so the component of muonium formed at the surface

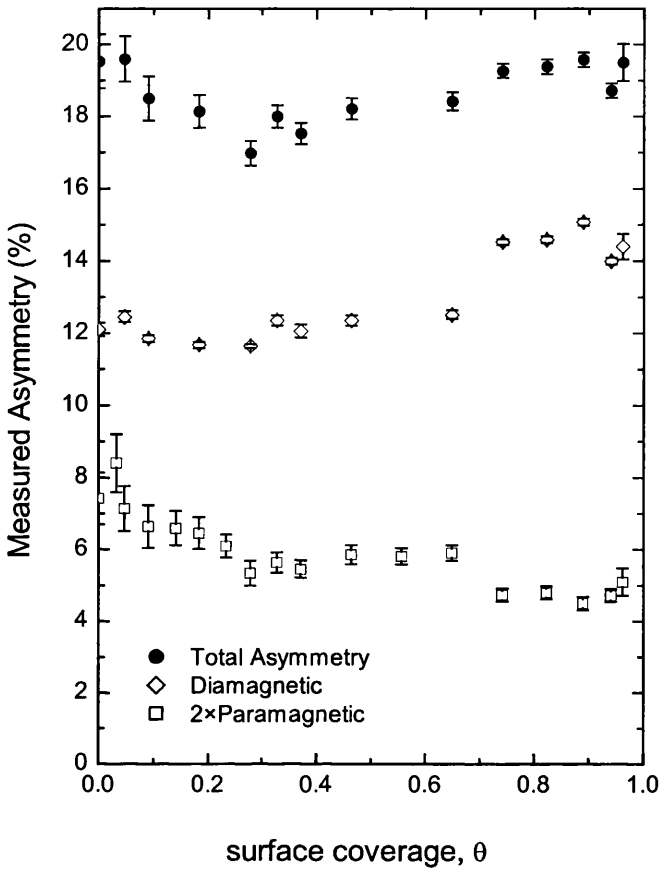

Figure 3.16. *Combined asymmetries for He on Cab-O-Sil® as a function of coverage.*

does so increasingly out of phase. For low to medium coverages, muonium is still formed swiftly enough that it does not contribute to the diamagnetic signal. Towards monolayer coverage the surface mechanism is frustrated as formation times (which we assume should be inversely proportional to the amount of free active sites) approach infinity, and this fraction is recovered in the diamagnetic asymmetry.

It is difficult to account for the double step structure (particularly visible for He, but also seen in Ar and, arguably, in Kr) within the asymmetry data according to this simple model of delayed surface formation. The form of these graphs suggests instead that there may be an additional, independent, mechanism superimposed. A sketch of possible components is given in Figure 3.17.

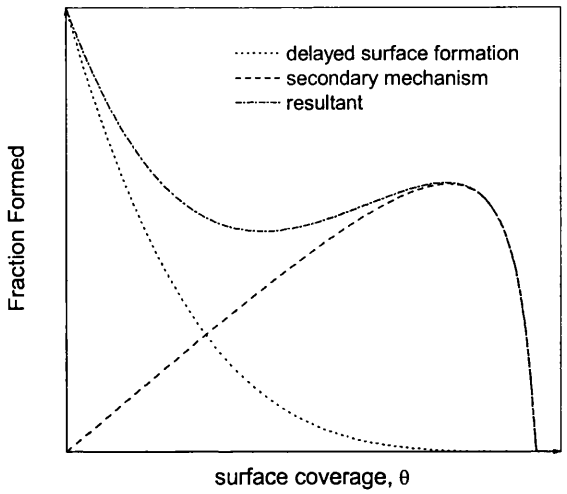

Figure 3.17. *Sketch of the suggested component mechanisms resulting in the observed Mu asymmetry.*

The form of the proposed 'secondary' (gas-related) mechanism dictates a formation process that increases with the addition of gas atoms, but is suppressed as the monolayer is completed. We suggest that this may involve an unexpected (new) mechanism for muonium formation/thermalisation involving *recoil* with the loosely bound surface gas atoms: At low coverage the recoil cross-section is proportional to the number of gas atoms, and the resulting muonium fraction increases almost linearly. This mechanism then gets frustrated, to some degree, when a monolayer forms; as the atoms become more confined on the surface and lose some degrees of freedom. Heavier atoms cannot participate as easily as He, making the effect less pronounced.

To resolve these two mechanisms further, we suggest that the gas coverage dependence of the delayed surface process be given by the preliminary expression

$$a + b(1-\theta)^n, \tag{3.22}$$

where a is a baseline component (the fraction of muonium attributed to bulk, or other

Table 3.7. Parameters obtained for delayed surface Mu formation mechanism.

Parameter	Fit to Kr data	Representative Mu fraction
a	1.34(4)	14(1)%
b	2.3(2)	24(3)%
n	4.8(16)	

non-surface-dependent, formation); *b* is the fraction of muonium formed via this surface process; and *n* is a parameter representing the degree to which formation sites are 'de-activated' by the presence of noble gas atoms.

If these parameters are independent of the type of covering gas, an upper limit for *n* may be obtained by fitting equation (3.22) to the lowest data-points in Figure 3.15. This can be done simply by fitting to the Kr data, taking the data above one monolayer to signify the baseline, *a*. The results of this analysis are shown in Figure 3.18.a.

The remainder, the fraction we attribute to the proposed recoil mechanism, is shown in Figure 3.18.b. This data does appear to roughly follow the expected form with He accounting for up to an additional 16(1)% to the muonium fraction. The helium recoil asymmetry is not completely suppressed as the coverage approaches one monolayer due to the very fluid nature of the layer at 6 K. Argon and Krypton on the other hand, both show a much lower yield via this mechanism, which is entirely suppressed at monolayer coverage.

If this description is qualitatively correct, an examination of the coverage dependence of the diamagnetic fraction for the other gases studied should reveal similar behaviour to helium. An explanation of the fine features of the relaxation data has yet to be included in the recoil model.

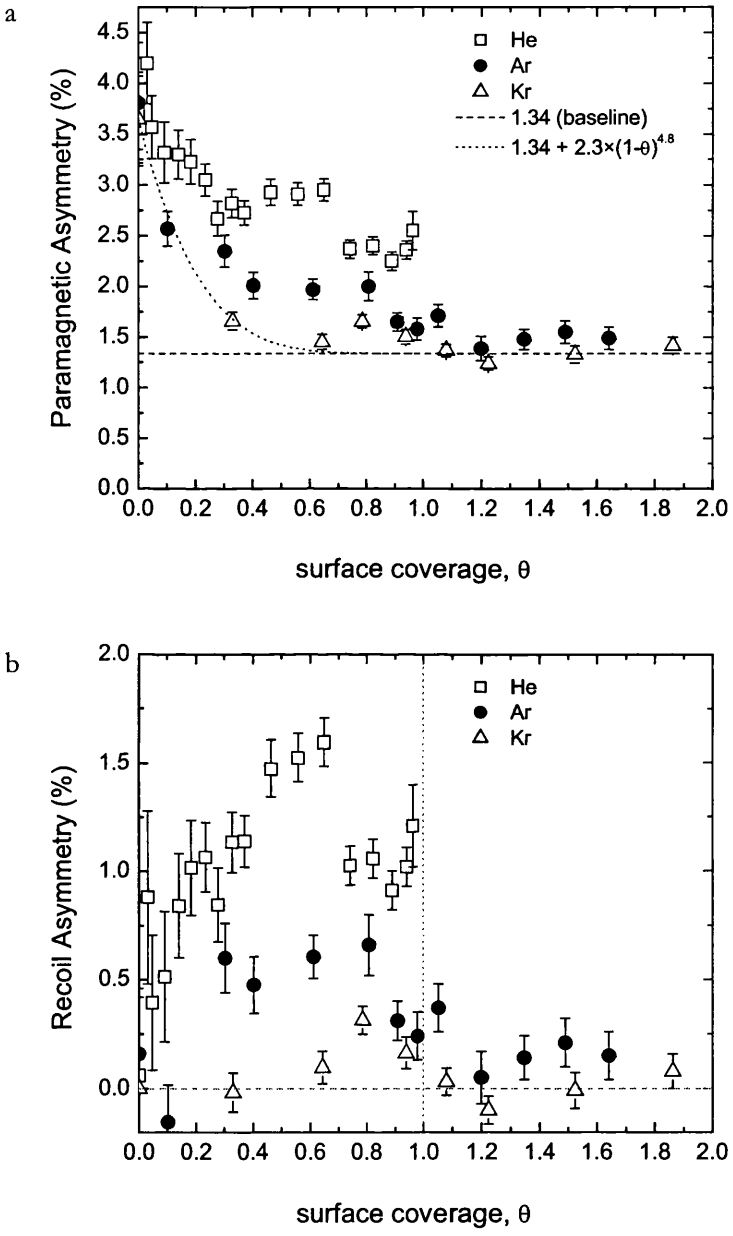

Figure 3.18.a. *Paramagnetic asymmetry data showing the results of a fit to equation (3.22) performed on the Kr data. The baseline value is obtained from a fit to the points beyond 1 monolayer coverage.* b. *Calculated "recoil" asymmetry; the result of subtracting the fit in* a *from each dataset.*

4 MUONIUM DYNAMICS IN SILICON AT HIGH TEMPERATURE

4.1 Hydrogen in Semiconductors

Hydrogen is unavoidably introduced into semiconductors during the production process and has a strong influence on their electronic properties, involving passivation of dopant sites, activation of some impurities and also formation of its own electrically active levels. To understand H activity where it is technologically both beneficial and detrimental is therefore of considerable industrial importance. While much theoretical work has been aimed in this area (conceptually the simplest of defect centres, but surprisingly complex in practice) it is very difficult to study *isolated* H directly, with the exception of some innovative experimental methods [see e.g. 4.1 and 4.2]. The problem is that conventional methods require high concentrations of H for sensitivity, whereupon it quickly diffuses and interacts with itself or other impurities to form hydrogen complexes. It is also complicated by the fact that H is considered to be a negative-*U* centre*, in which case the neutral state is only metastable. Muons on the other hand are introduced in small concentrations (one at a time in the case of a DC source) and almost never react with each other. Most of the experimental information over the past two decades has therefore come from μSR. A comprehensive review, concentrating on the early *static* spectroscopy, was given by Patterson [4.3] in 1988, and several more up-to-date papers are available [e.g. in 4.4].

In this chapter, muon and muonium dynamics are studied in high temperature (300-800K) Si, in a regime involving fast thermally activated cycles between crystallographic sites and charge states. In particular, we directly measure the fraction of time spent in the neutral

* For a negative-*U* centre, a more favourable energy configuration results from a negative and a positive centre than that of two neutral centres.

state as a function of temperature for this intermittent scheme and attempt to fit the results within a framework of corresponding transition and relaxation rates. A consistent theory is important for a more complete understanding of the interstitial location of hydrogen, its electronic structure and its diffusivity.

A brief overview of the muonium centres in intrinsic Si is given here first, explaining the expected dynamics and relaxation processes affecting the μSR signal. The principle behind our direct measurement of the *muonium fraction* is then explained, followed by our experimental results. We then set forward the models applied in our attempts to corroborate available data on transitions and relaxation rate.

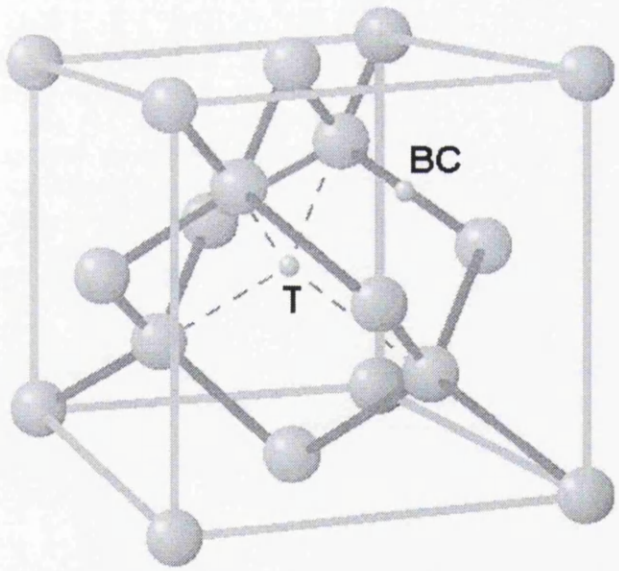

Figure 4.1. *Interstitial muonium sites in the Si crystal lattice. This shows the bond-centred (BC) sites,* Mu^0_{BC} *(and* Mu^+_{BC}*) and the tetrahedral (T) or cage-centred site,* Mu^0_T *(and* Mu^-_T*).*

4.2 Muonium Centres in Si

At low temperatures in semiconductors such as Si and Ge with the diamond lattice structure, Figure 4.1, the muon is known to exist in three distinct centres – two neutral paramagnetic centres at the tetrahedral site (*normal* Mu – here referred to as Mu_T^0)† and the bond-centred site (*anomalous* muonium, Mu* - here referred to as Mu_{BC}^0), and a third diamagnetic centre, Mu^D, which theory suggests is most likely to be either the positive charge state at the BC site, Mu_{BC}^+, or the negative charge state at the T site, Mu_T^-, or even a bound state with another impurity; this being difficult to establish experimentally due to the lack of an unpaired spin and associated hyperfine interactions.

The Mu_T^0 centre has an isotropic electron-muon hyperfine parameter, A_μ, and is known to be highly mobile. Mu_{BC}^0, established as the ground state [4.5], is held more firmly at a potential minimum within a stretched Si-Si bond. The unpaired electron occupies a non-bonding orbital with a node at the muon position and its hyperfine interaction is consequently axially symmetric about the <111> axis. Comparisons of muon avoided level crossing resonance (μALCR) results with parameters from electron paramagnetic resonance (EPR) measurements on bond-centred hydrogen, denoted the AA9 centre, have demonstrated the electronic equivalence of Mu_{BC}^0 and H_{BC}^0 [4.6].

Both of the paramagnetic states exist at low temperatures for the lifetime of the muon, together accounting for 97.8(80)% of the total measurable asymmetry. This is a remarkable example of metastability of a defect centre; density functional calculations have shown Mu_{BC}^0 to be the preferred site from energy considerations [4.7], but the potential barrier between the cage-centre and the bond-centre clearly prevent Mu_T^0 from reaching its true

† Throughout the chapter we adopt this notation with the superscript denoting the muonium charge state and the subscript the site information (relating to Figure 4.1).

ground state. This barrier is representative of the energy required to distort the Si-Si bond.

The extended wavefunction and weak binding of the bond-centre lead to a BC(+/0) electronic level near the conduction-band edge, but deeper than a typical shallow donor. T(0/–) is also expected to occur in the upper half of the band gap as evidence for it occurs only in highly doped n-type samples [4.8]; if it falls lower than BC(+/0) then it constitutes a negative-U centre. Figure 4.2 illustrates these energy levels; the value and sign of Δ has yet to be experimentally verified. Due to the significant ionisation energy of Mu_T^0, T(+/0) should fall within the valence band, while BC(0/–) lies well up in the conduction band due to the energetic cost of putting a second electron into the non-bonding orbital.

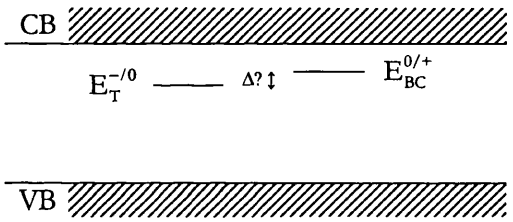

Figure 4.2. *Schematic energy levels within the gap for muonium in Si.*

As the temperature is increased above ~140 K, Mu_{BC}^0 is the first of these low-temperature states to be ionised, with no associated precession observed above 165 K. This is followed above ~220 K by ionisation of the Mu_T^0 site, leading to the detection of only a diamagnetic muon signal by ~300 K [4.3]. Both ionisation processes occur with activation energies of the order of a few tenths of an eV.

At yet higher temperatures, as the intrinsic concentration of conduction electrons increases, muonium may be formed intermittently by electron capture followed by rapid ionisation. This is evidenced by strong longitudinal field, $1/T_1$, relaxation which sets in above ~400 K [4.9]. Although this implies that the muon once again spends some time in the

neutral charge state, this charge-exchange is so rapid that the muon spin precession in Si, at all measured temperatures beyond the ionisation of Mu_T^0, occurs with a frequency at or near the μ^+ Larmor frequency.

4.2.1 Adaptation of the Vacuum Mu Spin Hamiltonian for Mu in Si

As we are concerned with the spin dynamics of muonium undergoing fast exchange between charge states, it is appropriate to examine the effects of the medium on the energy levels of the muonium system. In general the spin Hamiltonian in matter differs from the vacuum expression (chapter 1, § 1.6.1) by the addition of interactions with i neighbouring nuclei, such that

$$\begin{aligned} H &= A_\mu h\mathbf{S}\cdot\mathbf{I} + \tilde{\gamma}_e h\mathbf{S}\cdot\mathbf{B} - \tilde{\gamma}_\mu h\mathbf{I}\cdot\mathbf{B} \\ &+ \sum_i h\left[A_i\mathbf{S}\cdot\mathbf{J}^i + D_i\mathbf{I}\cdot\mathbf{J}^i + Q_i\mathbf{J}^i\cdot\mathbf{J}^i + \tilde{\gamma}_n^i\mathbf{J}^i\cdot\mathbf{B}\right], \end{aligned} \qquad (4.1)$$

where $\mathbf{J}^i$ is the spin operator of the ith nucleus; A_i and D_i are components of the hyperfine and dipolar tensors between the muon and the ith neighbouring nucleus; and Q_i is a component of the quadrupole tensor for nucleus i. However, Si has three naturally occurring isotopes of which only ^{29}Si (4.7% natural abundance) has non-zero nuclear spin $\mathbf{J} = ½$ [4.10]. This ensures that there are no quadrupole interactions and there will be dipole interactions with only a small fraction of the neighbouring nuclei. It is therefore appropriate to use the following simplified form of the spin Hamiltonian:

$$H = \tilde{\gamma}_e hS_z B - \tilde{\gamma}_\mu hI_z B + A_\parallel hS_{z'}I_{z'} + A_\perp h(S_{x'}I_{x'} + S_{y'}I_{y'}). \qquad (4.2)$$

The magnetic field is assumed to be directed along $\hat{z}$. The last two terms represent an anisotropic, axially symmetric hyperfine interaction described by two parameters, $A_\parallel$ and $A_\perp$, parallel and perpendicular to the symmetry axis $\hat{z}'$, which is given by the muon-

nucleus direction at the Mu_{BC}^{0} site. Since $\hat{z}'$ is tilted at an angle θ from $\hat{z}$,

$$\begin{aligned} I_{x'} &= I_x \cos\theta - I_z \sin\theta, \\ I_y &= I_y, \\ I_{z'} &= I_x \sin\theta - I_z \cos\theta, \end{aligned} \tag{4.3}$$

and similarly for **S**. For isotropic muonium $A_{\parallel} = A_{\perp} = A_{\mu}$ and the Hamiltonian is equivalent to the vacuum expression, with an appropriate amplitude for A_{μ}, leading to the familiar form of the energy levels in the Breit-Rabi diagram, Figure 4.3. For the anisotropic bond-centred site the resulting energy eigenvalues are dependent on orientation and the relative amplitudes of $A_{\parallel}$ and $A_{\perp}$, which are more than an order of magnitude smaller than

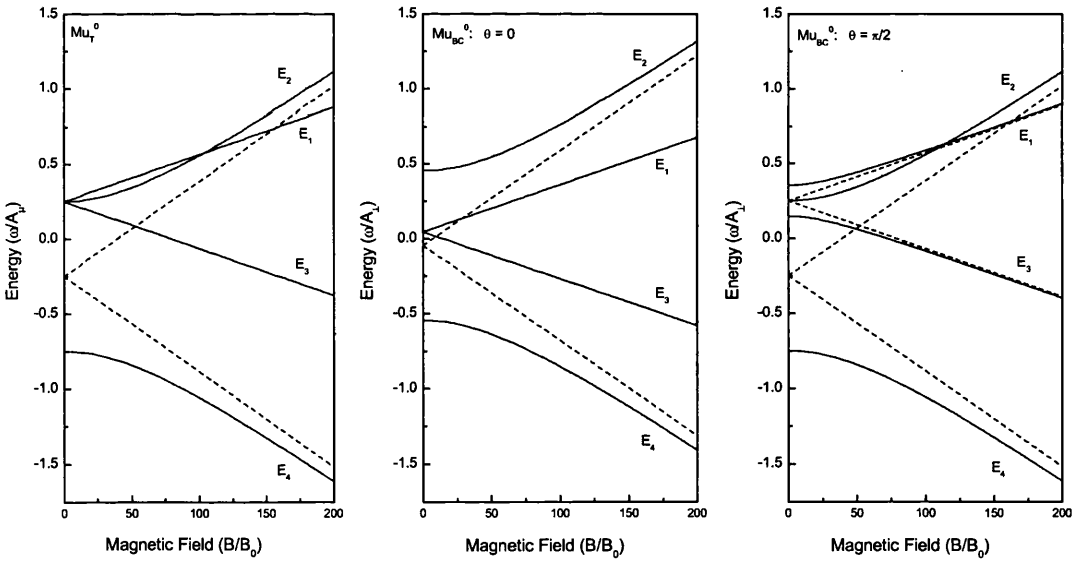

Figure 4.3. *Energy-level diagrams for isotropic muonium and two orientations (w.r.t <111> symmetry axis) of applied field for anisotropic muonium. The value of (γ_e + γ_μ) has been modified by a factor of 2 to exaggerate the field dependence of the eigenvectors for clarity. The diagram for* Mu_T^0 *in Si is identical to vacuum state Mu on the same normalised axes ($\nu_{12} \rightarrow 0$ for both vacuum Mu and* Mu_T^0 *at ~16.4 T and ~7.4 T respectively). The diagrams for* Mu_{BC}^0 *demonstrate the lifting of degeneracy for the anisotropic hyperfine coupling. Dashed lines are the high field asymptotes.*

Table 4.1. Hyperfine parameters for muonium in Si. From [4.11]

Centre	Hyperfine Parameters (MHz)
Mu_T^0	A_μ = 2006.3
Mu_{BC}^0	$A_\parallel$ = –16.82 $A_\perp$ = –92.59

A_μ, and are given in Table 4.1. Energy-level diagrams are shown in Figure 4.3 for Mu_{BC}^0 in two orientations, $\theta = 0$ and $\pi/2$.

4.2.2 *Spin Dynamics & Relaxation in a Longitudinal Field: 2-State Model.*

A model for the high temperature spin dynamics of muons in Si was developed by Chow *et al* [4.9]. The muon is considered static at the tetrahedral site, with cyclic "charge-exchange" (CE) commencing when the number of free carriers in the system becomes sufficient for the muon to begin alternately capturing and losing an electron.

The initial asymmetry is unity thanks to the fully polarised nature of the incident 'surface' muon. During the subsequent periods spent in the neutral paramagnetic state, the muon spin polarisation oscillates at the field-dependent frequency, ω_{24}, but in the diamagnetic state the polarisation ceases to evolve with time as the spin is "locked" along the field direction. We denote the average lifetime in the neutral state as τ_0, and the average time to cycle through both states as τ_{cycle}. In the fast exchange limit, $\tau_0\omega_{24} << 1$, the neutral state exists for only a fraction of one period of oscillation before the polarisation is locked once again. By contrast, in the slow exchange limit, $\tau_0\omega_{24} >> 1$, the spin undergoes many oscillations at ω_{24} during the time spent in the neutral state, as demonstrated in Figure 4.4.

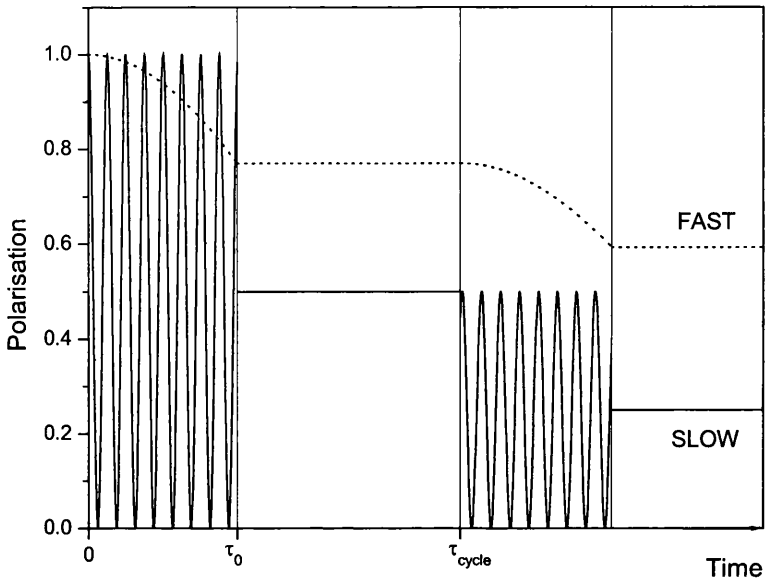

Figure 4.4. *Propagation of the muon spin in the charge-exchange regime. Time is shown in units proportional to the paramagnetic lifetime, τ_0, for clarity of the process, which leads to an expanded time scale for the fast limit (in reality ω_{24} is constant for a given temperature and field strength). In the slow limit the polarisation is averaged over many oscillations, as described in the text. The amplitude shown is appropriate to the process occurring in zero magnetic field.*

If $Q_z^i(t)$ is the time evolution of the polarisation of charge state *i*, the isotropic case may be completely described by the z-component, where

$$Q_z^{Mu}(t) = \frac{1+2x^2}{2(1+x^2)} + \frac{1}{2(1+x^2)}\cos(\omega_{24}t) \quad \text{for Mu}^{\ddagger}\text{, and} \tag{4.4}$$

$$Q_z^{\mu}(t) = 1 \quad \text{for } \mu^+. \tag{4.5}$$

Mu and μ^+ are then assumed to switch states randomly with average ionisation rate, $W_{Mu}\left(=\frac{1}{\tau_0}\right)$, and electron capture rate, $W_{\mu}\left(=\frac{1}{\tau_{cycle}-\tau_0}\right)$, respectively.

Chow [4.11] describes the CE process within a "strong collision" approach according to

‡ Equation (1.19) from chapter 1, where x is defined as the normalised field.

the following coupled integrals:

$$G_z^{Mu}(t) = P_{Mu}(0)Q_z^{Mu}(t)e^{-W_{Mu}t} + W_\mu \int_0^t G_z^{\mu}(\tau)Q_z^{Mu}(t-\tau)e^{-W_{Mu}(t-\tau)}d\tau \text{, and} \qquad (4.6)$$

$$G_z^{\mu}(t) = P_{\mu}(0)Q_z^{\mu}(t)e^{-W_{\mu}t} + W_{Mu} \int_0^t G_z^{Mu}(\tau)Q_z^{\mu}(t-\tau)e^{-W_{\mu}(t-\tau)}d\tau . \qquad (4.7)$$

Here $P_{Mu}(0)$ and $P_{\mu}(0)$ are the initial Mu and μ fractions respectively, and $G_z^{Mu}(t)$ and $G_z^{\mu}(t)$ describe the LF polarisation of the superscripted state ensemble at time *t*. In both (4.6) and (4.7) the first term corresponds to the decay of the muon polarisation formed promptly in that state (i.e. at $t = 0$). The second term is the "amount" of polarisation entering from the other state at time τ, which consequently evolves in the new state from τ to *t*. This is integrated over the elapsed time. The solution [4.11] leads to an expression for the time-dependence of the total polarisation, $G_z^{tot}(t)$, of the form $a\exp(-t/T_1)$ with

$$\frac{1}{T_1} \approx \frac{W_\mu W_{Mu}}{W_\mu + W_{Mu}} \times \left(\frac{1}{2} \frac{\omega_0^2}{W_{Mu}^2 + \omega_{24}^2} \right) . \qquad (4.8)$$

$$(\approx \text{ cycle rate} \times \text{loss of polarisation per cycle})$$

Here, ω_0 denotes the hyperfine frequency, $2\pi A_\mu$. This expression is equivalent to an expression derived by Senba [4.12] using a stochastic time-ordered method to describe the alternative dynamical process of "spin exchange" (SE) scattering, where stable muonium may interact with a conduction electron causing repeated flipping of the muonium electron between its $m_s = +½$ and $m_s = -½$ states. SE is more relevant if the temperature is below the muonium ionisation threshold and there are nevertheless a large number of free carriers in the system; in low temperature n-type Si, for example.

Assuming CE occurring at thermal equilibrium, whereby detailed balance is applicable, the

probability that the muon is in the neutral Mu_T^0 state (i.e. the occupancy of the Mu-electronic level in the band gap) may be written in terms of the transition rates as

$$p_0 = \frac{W_\mu}{W_\mu + W_{Mu}} = \frac{1}{1+\frac{1}{2}e^{(E_\mu - E_F)/k_B T}}. \qquad (4.9)$$

E_μ is the muon energy level in the band gap and E_F is the Fermi energy.

Assuming the capture rate to be of the form $W_\mu = \sigma \upsilon n$ (where σ is an average free electron capture cross section, n is the free electron concentration and υ is the average thermal velocity of the electron), Chow *et al* fit the results of both field and temperature dependent relaxation measurements, using equations (4.8) and (4.9), to obtain three parameters; σ, E_μ and $A_\mu(T)$. E_F was assumed to be located at mid-gap (at 800 K the material is essentially intrinsic) and no temperature dependence was included for the band gap.

The values obtained for A_μ were of the order of 2000 MHz, and were compatible with a linear extrapolation from direct measurements of A_μ for Mu_T^0 below 300 K [4.11]. σ was determined to be $2.8(3)\times10^{-15}$ cm^2 and the Mu(+/0) level placed at 0.34(1) eV below the conduction band edge (the uncertainty given in each case are purely statistical). These results imply a neutral fraction, p_0, via equation (4.9), which rises to a value of about 6% at 800 K.

The assumption of an isotropic system appears to be justified by the values obtained for A_μ and observations that $1/T_1$ is independent of sample orientation. The magnetic field dependence of $1/T_1$ was also characteristic of an isotropic hyperfine interaction. This is in accord with non-adiabatic behaviour preventing full relaxation of the lattice around the BC

site at high temperatures [4.13], which would then allow a large isotropic hyperfine interaction for a significant fraction of the muonium lifetime, p_0.

4.2.3 Larmor Frequency Shift

As mentioned previously, the charge-exchange occurs so rapidly at these elevated temperatures that the TF μSR signal corresponds to simple precession at or near the muon Larmor frequency. The persistence of this signal with the onset of CE cycling is a consequence of a form of motional narrowing, where the effect of the electronic "motion" is to cause the system to jump at random between a finite number of neighbouring frequencies. Figure 4.5 illustrates the result for the simple case of a system jumping between two signals at $\nu_\mu \pm \nu_0/2$ (where ν_μ = 80 MHz and ν_0 = 2000 MHz) at a selection of average hopping frequencies Ω. As Ω is increased the magnitude of the two signals is

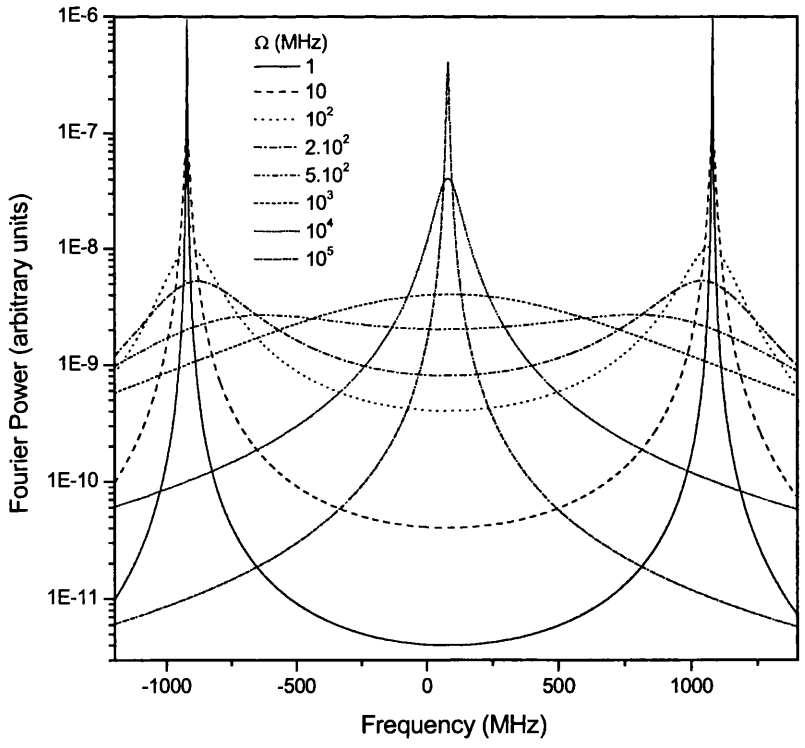

Figure 4.5. *Theoretical spectra of a system with two frequencies $\nu_\mu \pm \nu_0/2$, jumping from one to the other with average hopping frequency Ω. The values used here are ν_μ = 80 MHz and ν_0 = 2000 MHz, to represent approximately isotropic muonium in Si in a 6 kG magnetic field.*

reduced and is replaced, at hopping rates above about ν_0, by a single virtual signal of increasing magnitude midway between the two. The solutions shown correspond to the mixing of two identical signals described by delta functions, but is equally valid for signals of finite width causing only a related modification of the resultant linewidth.

These spectra are described according to standard magnetic resonance principles [4.14] and may be extended to more complicated situations with more than two frequencies and different jumping probabilities. In the two-state model described previously the hopping frequency Ω is equivalent to W_{Mu}.

In the presence of a large external magnetic field the two high frequency muonium signals ν_{14} and ν_{23} are essentially forbidden and only ν_{12} and ν_{34} remain with significant intensity. These two frequencies correspond to the neutral state with either parallel ($\uparrow$) or antiparallel ($\downarrow$) electron spin, and to first order are equal to $\nu_\mu - \frac{A_\mu}{2}$ and $\nu_\mu + \frac{A_\mu}{2}$ respectively[§]. As long as the hopping rate, W_{Mu}, is fast with respect to the time resolution of the μSR apparatus, the observed frequency is a weighted sum of the two significant muonium frequencies and the diamagnetic frequency, ν_μ.

Under these conditions, if γ is the fraction of time spent in the diamagnetic charge state, μ^+, and α & β are the fractions of time spent in each neutral spin configuration, $\uparrow$ and $\downarrow$ respectively, then $\alpha + \beta = p_0$ is the fraction of time spent in the neutral charge state (the *neutral fraction*). In addition the electron polarisation is, by definition, $P_e = \frac{\alpha - \beta}{\alpha + \beta}$, and the observed frequency, ν_{obs}, is then

§ This is strictly only true at high fields where $x >> 1$.

$$\nu_{obs} = \gamma\nu_\mu + (\alpha+\beta)\nu_\mu + (\alpha-\beta)\frac{A_\mu}{2}. \tag{4.10}$$

Since $\alpha + \beta + \gamma = 1$ and substituting for p_0 and P_e, we get

$$\nu_{obs} = \nu_\mu + p_0 P_e \frac{A_\mu}{2}. \tag{4.11}$$

In an unpolarised medium the two paramagnetic frequencies cancel and only the frequency of the bare muon is observed. In a polarised medium the neutral fraction may be directly extracted from measurements of the proportional shift of the muon Larmor frequency $\Delta\nu/\nu_\mu$ via the relationship

$$\frac{\Delta\nu}{\nu_\mu} \approx \frac{hA_\mu}{4k_BT}\frac{\tilde{\gamma}_e}{\tilde{\gamma}_\mu} p_0. \tag{4.12}$$

We take the electron polarisation to be given by Curies Law,

$$P_e = \frac{1-e^{-h\tilde{\gamma}_e B/k_BT}}{1+e^{-h\tilde{\gamma}_e B/k_BT}} \approx \frac{h\tilde{\gamma}_e B}{2k_BT}, \tag{4.13}$$

approximated to a linear dependence with magnetic field strength at the comparatively low fields used in this work.

4.3 Experimental Details

These experiments were performed on the GPS instrument at PSI (see § 1.5.2) on a sample of TopSil** silicon. This is a near intrinsic sample of crystalline Si with a net p-type carrier concentration at room temperature of ~10^{11} cm^{-3}, from the same batch as was used by Chow *et al* [4.9] for their LF measurements of muon spin relaxation. It is also the material denoted 'P11' in the RF muon spin resonance experiments of Kreitzman *et al* [4.8] and Hitti *et al* [4.15], whose dynamical parameters are described in § 4.5.1.

The measurements were made in high magnetic fields, 6 kG and 3 kG, stable to several ppm and reproducible in several temperature sweeps. The "Zürich" oven was used to cover a range between room temperature and 800 K. At no point within this temperature range does the conduction electron density increase to sufficient levels to prevent the formation of muonium by charge screening. The Si was held in a Ta foil 'packet' to act as a diffusion barrier between the copper of the sample block and the Si. This was then wired to the sample holder for good thermal contact, which was important at the lower temperatures where conduction is the main form of heat transport (the sample block is attached to a "warm" finger and operated in vacuum).

A rotation of the incoming muon spin direction by approximately 45° at the GPS electrostatic separator allowed the collection of LF relaxation data in the F and B detectors simultaneously with TF frequency data in the U and D detectors. This meant a small reduction in the maximum asymmetry and count rate for each geometry, but ensured identical conditions.

** TopSil Semiconductor Materials A/S, Frederikssund, Denmark.

4.4 Results

Figure 4.6 shows the temperature dependence of the muon precession frequency measured for the TopSil Si sample. Considering the magnitude and sign of the hyperfine parameters in Table 4.1, the small negative shift between about 350 and 500 K may represent a contribution from Mu^0_{BC}, but the main feature is the striking rise in frequency above 500 K, with a shift as great as 0.7% by 650 K. The statistical uncertainty, increasing dramatically above 400 K, are a consequence of the high TF relaxation (Figure 4.7) at elevated temperatures which, as mentioned in § 4.2, is also a signature of the onset of charge exchange. The broad peak in TF relaxation rate between 500 K and 600 K is therefore indicative of a hop rate (W_{Mu}) of the order of the hyperfine frequency, ω_0.

Figure 4.8 shows the corresponding values of neutral fraction p_0 inferred from equation (4.12), using a high temperature extrapolation for A_μ which is appropriate within the

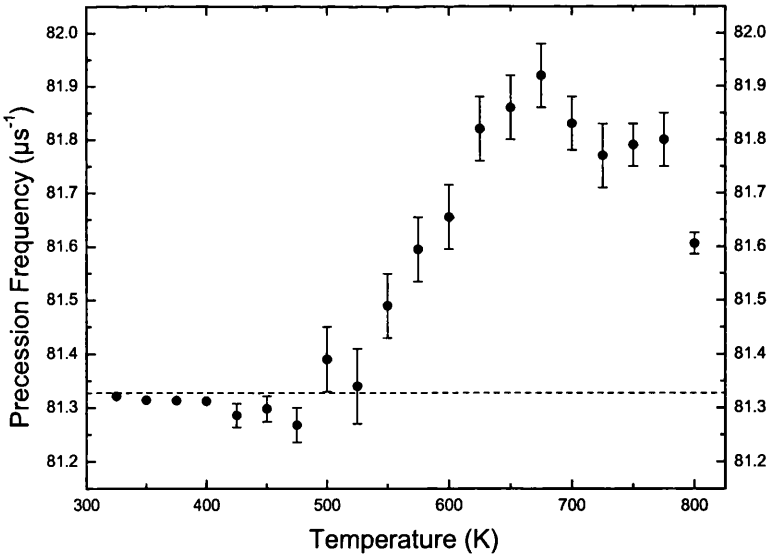

Figure 4.6. *Frequency shift in Si measured at 6 kG. The dashed line is the muon Larmor frequency in the same field (=81.3271 MHz; measured in Ag and corrected for Knight shift ††).*

†† See chapter 5 for an explanation of the Knight shift.

temperature range studied: $A_\mu(T) = 2046 - 0.37T$ MHz (see e.g. [4.11]). According to that model, the value of p_0 reaches unity by 650 K, in stark contrast to the values predicted by

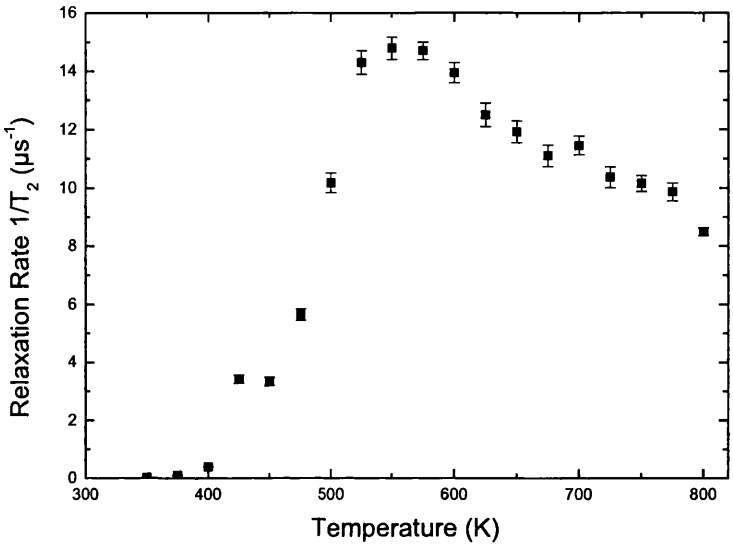

Figure 4.7. *Transverse field ($1/T_2$) relaxation rate as a function of temperature for Si measured at 6 kG.*

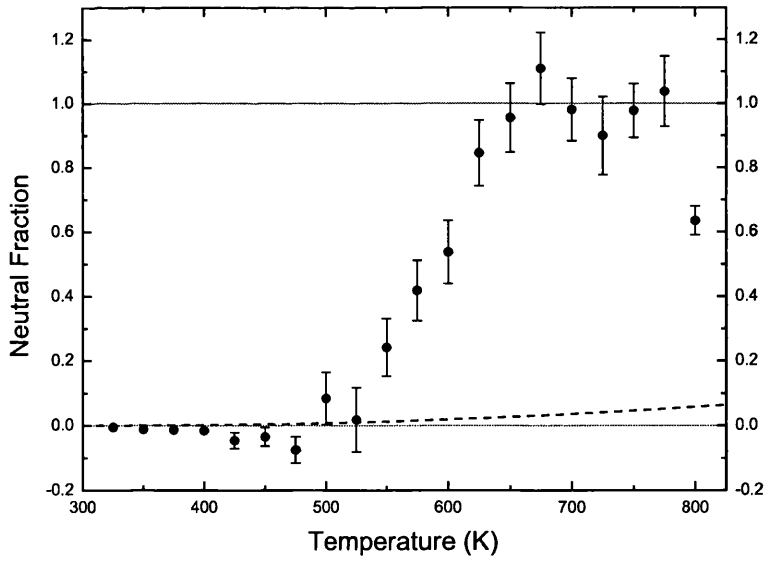

Figure 4.8. *Neutral fraction, p_0, obtained by applying equation (4.12) to the data of Figure 4.6. The dashed line indicates the temperature dependence of p_0 implied by the low field relaxation data of Chow et al.*

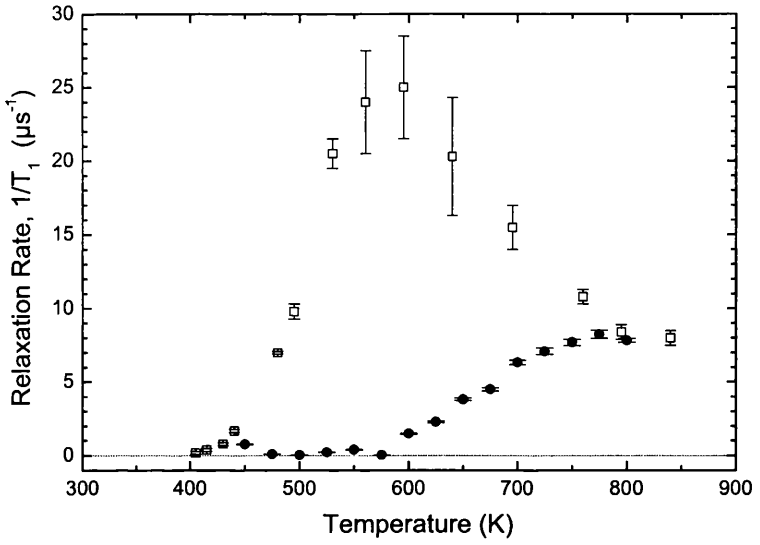

Figure 4.9. *LF ($1/T_1$) Relaxation rate as a function of temperature for several applied magnetic fields. Chow's data (150-400 G) are marked with open squares; our own data for 6 kG are marked with closed circles.*

equation (4.9) indicated by the dashed line in the figure. This is not only surprising but also rather fortunate as, with hindsight, the predicted values (although they are within the timing resolution at PSI) would have proved difficult to measure at the concomitant high TF relaxation rate.

LF relaxation data are shown in Figure 4.9, where the low field data of Chow *et al* are also included. Each dataset shows clearly the onset of CE, which in the slow exchange limit is governed by the increasing cycle rate. The peak marks the crossover between the slow and fast regimes, where the polarisation lost per cycle becomes limited by the duration in the depolarising state. Increasing the applied magnetic field extends the slow regime to higher temperatures, and reduces the amplitude of the oscillating component[#], decreasing the relaxation rate maxima.

Recall the repolarisation curve, which shows the amplitude of the electron-muon flip-flop frequency ω_{24} to be $1/(1+x^2)$.

4.5 Discussion

Although the LF relaxation is apparently well described by equation (4.8), it is impossible to simultaneously account for the neutral fraction implied by the frequency shift. In fact, the expression derived for p_0 within the two state model, equation (4.9), forbids values above 50%. In this section, we extend the existing models and examine some of their shortcomings in an effort to resolve these inconsistencies.

4.5.1 The Dynamical Model

For site and charge transitions we adopt the more complete model of Kreitzman *et al* [4.8] and concentrate on conversions between the Mu_T^0 , Mu_{BC}^0 and Mu_{BC}^+ states discussed above. We also include Mu_T^- for a more complete model in conditions of increased conduction electron density at high temperature. We consider paths between the states, which we label i,j = 1-4 for simplicity, to be dependent upon energy barriers E_{ij} which are combined with appropriate prefactors to formulate transition rates, denoted W_{ij}. Figure 4.10 illustrates the relevant transitions, which are detailed below. The physical interpretation of these state changes, and indeed our notation, becomes clearer when

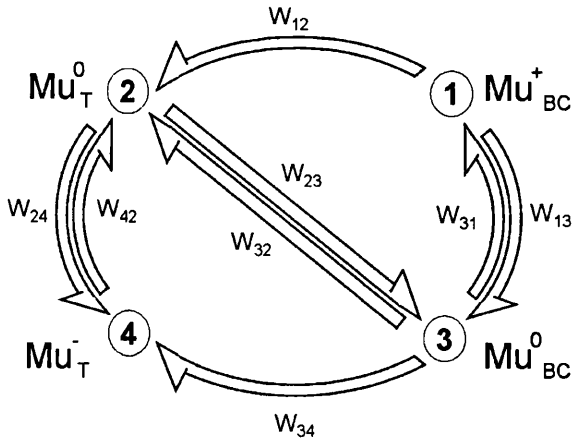

Figure 4.10. *Site- and charge-state transitions and the labels used in this work. Transitions between 1 and 4 are second order in terms of capture cross section.*

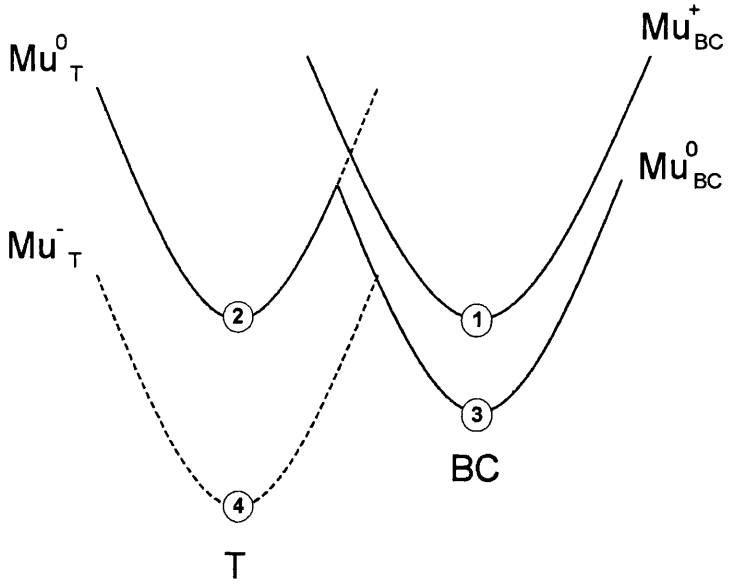

Figure 4.11. *A schematic configuration-coordinate diagram based on a system containing a muon and two electrons. The electrons are assumed to occupy levels at the bottom of the conduction band when dissociated from the muon. Here the diagram is not to scale and is only used as a guide to relative energy levels and the barriers to site and charge exchange. It should also be noted that this is an idealised picture which makes no attempt to understand the true shape of the energy barriers – the reader is referred to theoretical works for examples of more realistic potentials.*

represented in a configuration-coordinate diagram such as Figure 4.11.

The transition denoted W_{21} is expected to be precluded by site change from Mu^0_T to Mu^0_{BC} (possibly followed by rapid ionisation), and likewise W_{43} should be precluded by loss of e^- at the Mu^0_T site, followed by site change. We ignore hole capture relevant only to p-type samples. The transitions that we are concerned with instead involve the two straightforward electron capture and ionisation processes, as well as simple site change and activated processes (simultaneous site and charge change). The transitions are summarised in Table 4.2.

Table 4.2. Transitions for muonium in Si. The initial dynamic parameters shown are those derived by Hitti *et al* [4.15] from rf-μSR data§§, and were used as starting values in our models.

Mu transitions		Parametric transition rates	Initial parameter values	Fitted values
Electron Capture processes				
W_{13}	$Mu^{+}_{BC} + e^{-} \rightarrow Mu^{0}_{BC}$	$n\upsilon\sigma_{13}$	$\sigma_{13} = 3300$	
W_{24}	$Mu^{0}_{T} + e^{-} \rightarrow Mu^{-}_{T}$	$n\upsilon\sigma_{24}$	$\sigma_{24} = 8$	
Simple site changes between the two neutral states				
W_{23}	$Mu^{0}_{T} \rightarrow Mu^{0}_{BC}$	$\rho_{23}e^{-E_{23}/kT}$	$\rho_{23} = 4.1 \cdot 10^{12}$ $E_{23} = 0.38$	$\rho_{23} = 1.5 \cdot 10^{14}$ $E_{23} = 0.46$
W_{32}	$Mu^{0}_{BC} \rightarrow Mu^{0}_{T}$	$\rho_{32}e^{-E_{32}/kT}$	$\rho_{32} = 0$ $E_{32} = 0$	$\rho_{32} = 1.3(40) \cdot 10^{17}$ $E_{32} = 0.66(16)$
Activated electron capture				
W_{12}	$Mu^{+}_{BC} + e^{-} \rightarrow Mu^{0}_{T}$	$n\upsilon\kappa_{12}e^{-E_{12}/kT}$	$\kappa_{12} = 2.3 \cdot 10^{-10}$ $E_{12} = 0.40$	$\kappa_{12} = 1.5(64) \cdot 10^{-8}$ $E_{12} = 0.56(21)$
W_{34}	$Mu^{0}_{BC} + e^{-} \rightarrow Mu^{-}_{T}$	$n\upsilon\kappa_{34}e^{-E_{34}/kT}$	$\kappa_{34} = 8.4 \cdot 10^{-9}$ $E_{34} = 0.31$	
And ionisation (equivalent to hole capture in p-type samples)				
W_{31}	$Mu^{0}_{BC} \rightarrow Mu^{+}_{BC} + e^{-}$	$\rho_{31}e^{-E_{31}/kT}$	$\rho_{31} = 2.7 \cdot 10^{13}$ $E_{31} = 0.21$	
W_{42}	$Mu^{-}_{T} \rightarrow Mu^{0}_{T} + e^{-}$	$\rho_{42}e^{-E_{42}/kT}$	$\rho_{42} = 2.0 \cdot 10^{13}$ $E_{42} = 0.56$	

σ – capture cross-section (Å^2)
ρ – vibrational prefactor (s^{-1})
E – energy barrier (eV)
κ – composite site-change-electron-capture cross-section (cm^2)

Direct ionisation of Mu^{0}_{T} is not included as this branch of the energy surface in the configuration-coordinate diagram is supposedly inaccessible. Therefore, comparison of the parameter values shows that site change (W_{23}) is the rate-limiting factor for electron loss.

§§ The rf-μSR results were sensitive to the charge-cycle onset region, with parameters gained by the analysis of resonance conditions as paramagnetic states convert to diamagnetic states through ionisation or doping. They are measured at low temperature and not necessarily assumed to hold over the full temperature range studied.

The conduction electron density, n, ignoring the slight temperature dependence of the band gap, is taken to be

$$n = n_0\left(\frac{T}{300}\right)^{3/2} e^{-E_g/2kT}$$, where $n_0 = 1.64\times10^{20}$ cm^{-3}, and $E_g = 1.2$ eV.

For the electron thermal velocity, υ, we use

$$\upsilon = \upsilon_0\left(\frac{T}{300}\right)^{1/2}$$, where $\upsilon_0 = 2.03\times10^{7}$ cm s^{-1}.

For reference, these values are plotted in Figure 4.12.

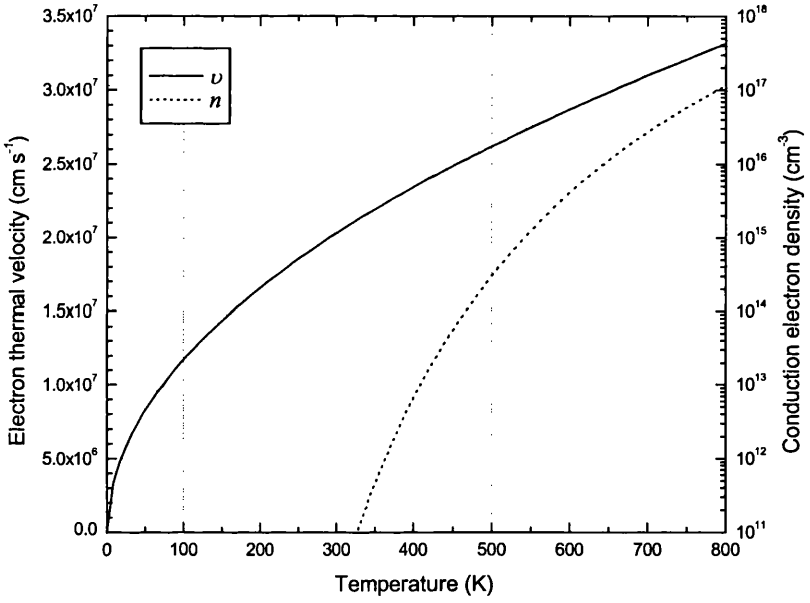

Figure 4.12. *Values used for conduction electron density and thermal velocity (shown on separate axes).*

4.5.2 Three- and Four-State Implementation

By once again assuming thermal equilibrium conditions, detailed balance arguments may be applied to obtain expressions for the neutral fraction. Ignoring state 4 (Mu_T^-) and regarding only transitions between the more likely states; 1, 2 and 3, we get

$$p_0 = \frac{W_{13}W_{32} + W_{12}\left(W_{31} + W_{32}\right)}{W_{23}W_{31} + W_{13}\left(W_{23} + W_{32}\right) + W_{12}\left(W_{23} + W_{31} + W_{32}\right)}. \qquad (4.14)$$

If we include the negative ion, the equivalent expression is

$$p_0 = \frac{(W_{13}(W_{32}+W_{34})+W_{12}(W_{31}+W_{32}+W_{34}))W_{42}}{W_{23}W_{31}W_{42}+W_{13}(W_{24}(W_{32}+W_{34})+W_{23}W_{34}+W_{42}(W_{23}+W_{32}+W_{34}))+ W_{12}(W_{24}(W_{32}+W_{34})+W_{23}W_{34}+W_{42}(W_{23}+W_{32}+W_{34})+W_{31}(W_{24}+W_{42}))}, \quad (4.15)$$

which has very quickly become quite cumbersome. p_0 is again defined here as the fraction of time spent in the neutral state at the tetrahedral site (state 2, or Mu_T^0)***. For comparison with the measured results both of these functions are plotted in Figure 4.13, using the parameters from Table 4.2 (the 'Hitti' parameters). Comparing the values of the transition rates across the temperature range (Figure 4.14) one can see that, in terms of the 3-state

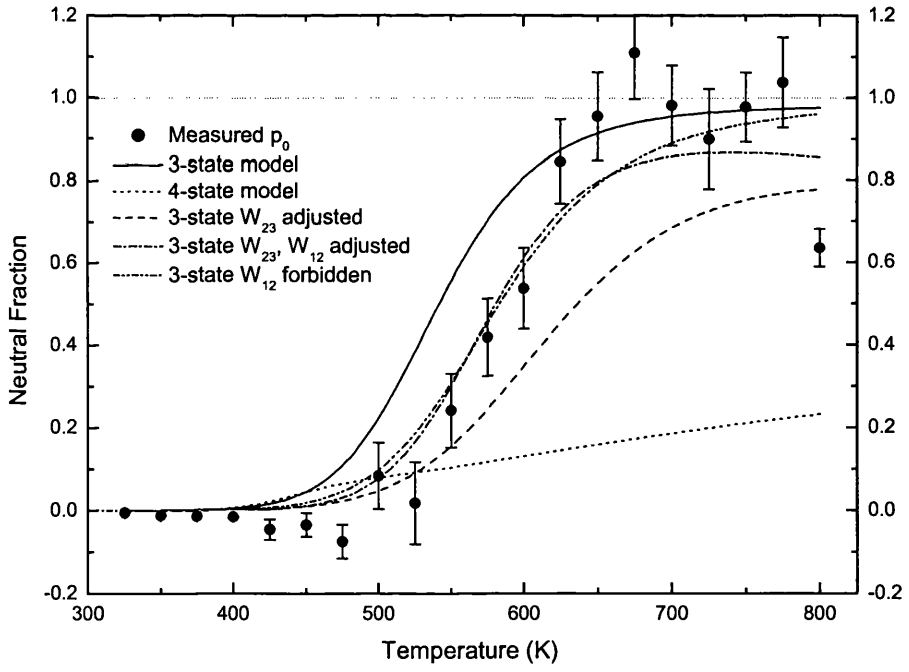

Figure 4.13. *Comparison of modelled values of neutral fraction with directly measured results. The three-state model requires only a small adjustment of parameters to give good correspondence. The four-state model requires alterations that are more severe but may be necessary to account for the decrease in neutral fraction at high temperature. The additional fitted curves are described in the text.*

*** For a complete picture, one should of course also take into account the effects of time spent by the muon in the other states. In Appendix III similar expressions for the corresponding occupation of the other levels are developed from the same principles.

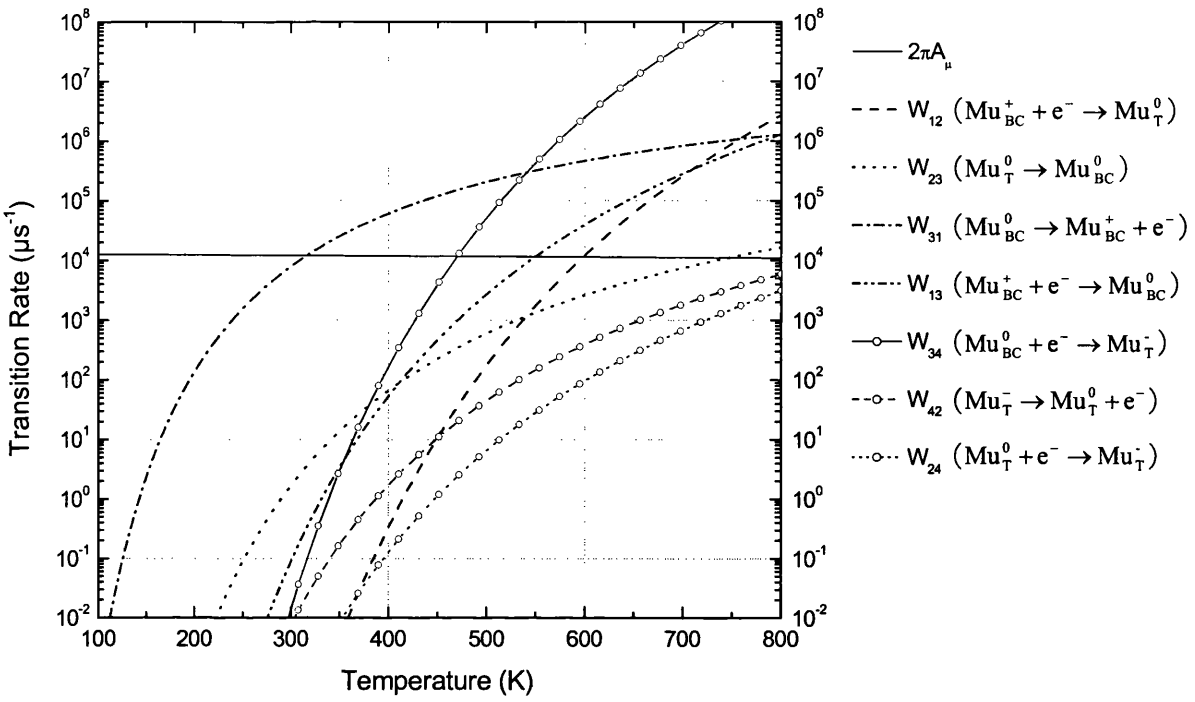

Figure 4.14. *Rates of each transition across the studied temperature range, produced using the initial parameters given in Table 4.2. This serves to highlight the competition between the states, which controls the outcome of the models. The hyperfine frequency is also included as a guide to its role in the features of the relaxation data. Transisitions withing the 4-state model are distinguished here by the addition of circles.*

model, the neutral fraction begins to ascend as electron capture at the BC site becomes faster than site-change from T to BC, rises through 50% as the activated electron capture into and site change out of the T site become equal, and approaches a maximum near unity as this activated electron capture to T overtakes capture to BC. This three-state expression appears to model the data quite convincingly. It gives initial values close to the data, though apparently shifted to slightly lower temperatures[†††], and can be made to fit well with small refinement of some of the parameters.

The neutral fraction is reduced in the four-state model. It may be (with reference to Figure 4.14 and Appendix III) that the occupation of the Mu_T^- site is exaggerated, by the

††† This shift of ~50° causes one to question the temperature calibration of the experiment, but repeated measurements have confirmed our data to be reliable.

Hitti parameters, beyond a level which may be appropriate for our slightly p-type material. However, the data may still be modelled with quite large changes to the parameter set. We do not proceed any further with the four-state model in this work, but note that inclusion of the negative ion may be necessary to account for the decrease in p_0 at high temperatures – the beginning of which can be seen from the final data point at 800 K (the high temperature limit of the Zürich oven at PSI).

Both the three- and four-state models are sensitive to the majority of the parameters (most parameters can be adjusted to improve the fit equally), and therefore care must be taken in establishing an unambiguous fit. To achieve this, we attempt to simultaneously fit data taken at different applied magnetic fields (using Chow's low-field data), and also examine the influence of parameter changes on the implied relaxation rate.

Extension of the two-state relaxation rate expression requires only the adjustment of the appropriate ionisation rate. We may re-write equation (4.8) in a more general form as

$$\frac{1}{T_1} = \lambda \approx p_0 W \times \left(\frac{1}{2} \frac{\omega_0^2}{W^2 + \omega_{24}^2} \right) \times \frac{1}{\alpha}. \qquad (4.16)$$

Here the cycle rate (1st term on r.h.s.) is portrayed explicitly in terms of average occupancy in- and rate of exit from Mu_T^0. As we are including the occupation of the T-site only, although the cycles involve both neutrals, this expression should set a lower limit for the relaxation. However, the limited occupation of the BC-site (see Appendix III) and its lower hyperfine parameters, mean that any additional effects are expected to be very small.

The third term, α^{-1}, is a parameter that we have been forced to introduce in our attempts to satisfy both the neutral fraction and relaxation rate data with a single set of transitions.

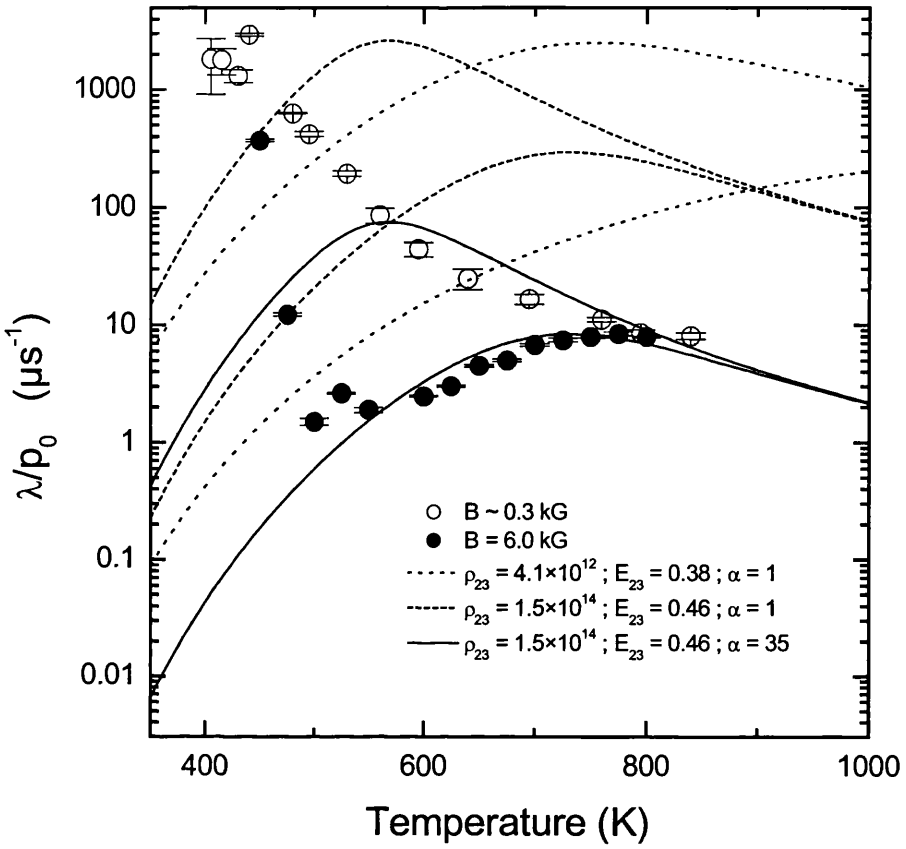

Figure 4.15. *The quantity λ/p_0 used to obtain fitted parameter values for the* $Mu_T^0 \rightarrow Mu_{BC}^0$ *transition, W_{23}. The solid lines show the simultaneous best fits to the two data sets, achieved following the introduction of an α value of 35. The dotted and dashed lines are not fitted curves, but illustrate respectively the initial values (Hitti parameters) and the fitted result in the absence of an α parameter. The analysis is performed only on the data at 550 K and above, as division by very small p_0 values below this temperature made the calculation of λ/p_0 less reliable (the error bars reflect only those errors in λ).*

It is clear from equation (4.16) that the quantity λ/p_0 is sensitive to W ($=W_{23}$) only, and therefore this is the most appropriate transition rate to adjust first. It is here that the need for the α parameter becomes clear. The fitted curves are shown in Figure 4.15, where they are compared to the initial values and the fitted values with this *scaling* factor removed. It proved impossible to model the data at all without values of α in the range 35-50.

To calculate λ/p_0, the relaxation data was divided by a functional form of p_0 that had been

created by fitting the data most accurately without particular regard for physical parameters. As a consequence, the λ data below ~550 K is divided by increasingly small numbers and it is not clear how reliable the adjusted data is. The fit has been adjusted by sight, with emphasis on the high temperature region. The resulting p_0 is shown as a dashed line in Figure 4.13. This new set of parameters is then used as a basis for fitting p_0, varying only the W_{12} transition, to give the dash-dot line in the same figure.

Finally, we have briefly explored a variation of the three-state dynamical scheme where we "turn off" the W_{12} transition and "turn on" the reverse site change transition W_{32} (hence the inclusion of W_{32} in the models, although Hitti *et al* give no dynamical parameters for this transition). This scheme forbids activated electron capture, and assumes that electron capture precedes site change. In principle, this could determine the site-change energy between Mu^0_{BC} and Mu^0_T, via the difference in activation energies of W_{32} and W_{23}; thus ordering the donor and acceptor levels for muonium in silicon and answering the "negative-*U*?" question.

The altered parameters, from the λ/p_0 fit (W_{23}), the subsequent fit to p_0 (W_{12}) and the alternative scheme (W_{32}), are given in Table 4.2, and the transition rates are re-drawn in Figure 4.17. It is important to note the imprecision of the fitted values, which makes it difficult to draw any definite conclusions, at this time, with regard to energy levels. The corresponding p_0 functions are included in Figure 4.13[‡‡‡], and the values for the two closest fits are used in Figure 4.16 to plot the relaxation rate predicted by equation (4.16) as a result.

Physically, the scale factor we have introduced implies, at least in the slow limit[§§§], that the

The fit corresponding to inclusion of W_{32} also includes the revised values of W_{23}.
§§§ Where an increase in cycle duration does not affect the polarisation lost during the cycle.

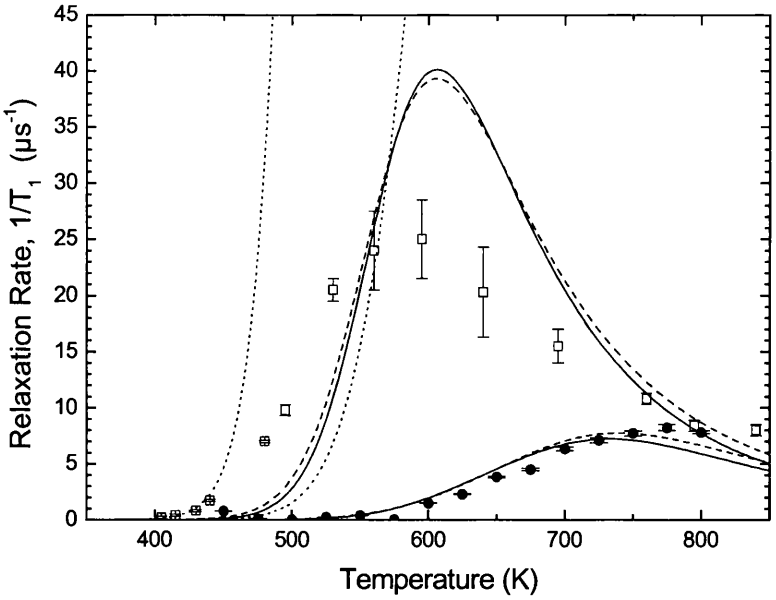

Figure 4.16. *Temperature dependent LF relaxation rates for low- and high-field data. The lines represent the corresponding low- and high-field predictions of equation (4.16), using the transition-rate parameters that give the best fit to* p_0. *Two sets correspond to the adjustment of* W_{12} *&* W_{23}*; the solid lines correspond to* $\alpha = 35$*, while the dotted lines correspond to* $\alpha = 1$ *(low field left, high field right). The adjustment of* W_{32} *(forbidding* W_{12}*), with* $\alpha = 35$*, forms the dashed set.*

μ^+ may have a high probability of re-capturing the same e^- lost in the preceding ionisation. In the fast limit, the change in the relaxation rate is more complex than simply scaling the expression to represent an *effective* cycle rate. If this intriguing notion of correlation between the muon and electron (which brings to mind an exciton-like delocalised state) is realistic, it is also possible that the scale factor is temperature dependent. Our static α appears to over-compensate at low temperatures, and under-compensate at higher temperatures. Interestingly, schemes that include the reverse site change transition, W_{32}, have an effective temperature dependent α built into the ratio W_{32}/W_{31} (the probability of Mu returning to the T site rather than ionising at BC). While this may offer an opportunity to account for the neutral fraction and relaxation rate simultaneously, it seems unlikely that ionisation at the bond centre should be slower than site change by a significant amount.

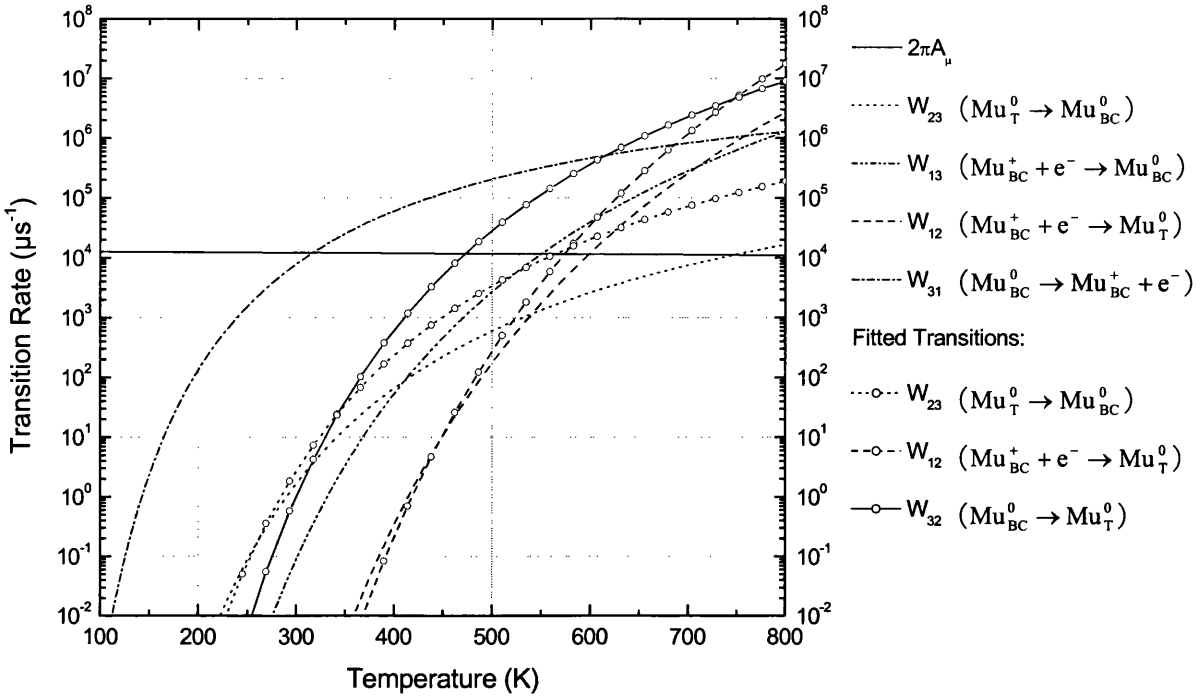

Figure 4.17. *Rates of each transition from the 3-state model. The three additional curves, distinguished here by the addition of circles, are produced using the fitted parameters given in Table 4.2.*

In conclusion, it is clear that the dominant neutral fraction, implied by the significant frequency shift, at high temperatures requires a more complex model than that previously used to describe LF relaxation rates alone. The 3-state configuration-coordinate model describes the behaviour of the neutral fraction well but, in its current form, fails to simultaneously account for observed relaxation rates.

The introduction of the inverse site-change transition to the model may be key to determining the order of electrically active levels in the band gap for muonium (and therefore H) in Si. However, a consistent model appears to require a more complete picture, possibly including the involvement of the BC site, and additional contributions, such as electron spin-exchange, to the muon spin relaxation.

5 ENHANCED MUON RELAXATION IN SEMIMETALS & METALS

5.1 Overview and Motivation

The sets of experiments reported in this chapter developed out of an investigation of exfoliated graphite (GRAFOIL®*), in 1997 [5.2], which was a preliminary to studying (slow) muons on surfaces. The LF relaxation rate, $1/T_1$, for the GRAFOIL® sample was found to be significantly larger than the values expected due to the Korringa mechanism (§ 5.2) expected in a diamagnetic material. The results can be seen in Figure 5.1 along with subsequent measurements of bulk HOPG† graphite, which also exhibits a departure from Korringa values above room temperature.

Although we now believe an additional mechanism (involving a molecular radical) responsible for the observed relaxation in graphite (§ 5.5), these early results prompted an interest in materials like graphite, whose diamagnetic nature is not simply distinguished due to their low conduction electron density. This led naturally to an investigation of semimetals which strike an intriguing balance between insulators/ semiconductors, where Mu^0 is commonly formed, and metals, where the diamagnetic bare μ^+ signal is maintained due to the electrostatic screening effect of the large number of conduction electrons.

This chapter therefore brings together results for a collection of metallic and semimetallic elements including graphite, C; As; Sb; Bi; and Pb. As the expected Korringa relaxation is closely linked to Knight shift (§ 5.2), other metals were included in this study; Cd, for its

---

* GRAFOIL® is produced by a process involving chemical exfoliation of natural graphite flakes into a vermicular form, which are then pressed or calendered into sheet form. The compression results in many interconnecting paths consisting of crushed "worms", which are nevertheless aligned well enough that the plane of the sheet reflects the stronger bonding within the graphene layers of the graphite crystallites [5.1]. Typical density of a GRAFOIL® sheet is about 1.5 g/cm^3.

† Highly Oriented Pyrolytic Graphite, density around 2.3 g/cm^3.

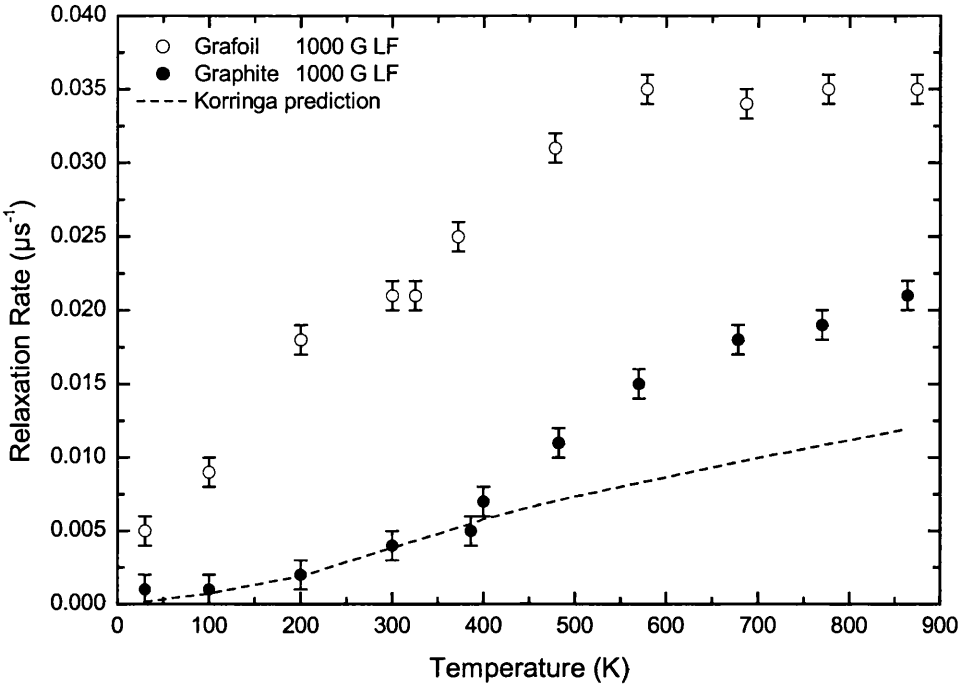

Figure 5.1 *Temperature dependent relaxation rates in GRAFOIL® and graphite. The dotted line indicates the prediction of the Korringa model using graphite Knight shift values measured at TRIUMF [5.4] across the full temperature range.*

'enhanced' muon Knight shift values; and Hg where, notably, the muon Knight shift has a relatively flat temperature dependence with a marked discontinuity through the melting point [5.3]. In addition Cu was doped with various levels of Fe (100ppm, 10ppm and nominally 0ppm) to check for possible false effects arising from trapping of the muon at magnetic impurities.

Knight shifts and Korringa relaxation are introduced briefly here as background material, followed by a description of the results obtained for the systems under investigation., and the conclusions that can be drawn. A brief account is also given of the treatment of graphite, as currently understood.

5.2 The Muon Knight Shift, Korringa Relaxation and Carrier Densities

The conventional Knight shift usually refers to metallic nuclei [5.5], where the magnetic

susceptibility is associated with the conduction electrons. It describes a contribution to the magnetic environment at the nucleus measured in a nuclear magnetic resonance (NMR) experiment. The contribution, arising from the conduction electron spin, is averaged over all electron states as different electrons interact with the nucleus in turn. This "averaging" alters the paramagnetic susceptibility, such that in zero applied field the electron spins cancel out and there is no effect, but in an applied static field there is a small shift, $\Delta\omega$, in the NMR frequency, proportional to both conduction electron polarisation (the Pauli spin susceptibility) and conduction electron density at the nucleus. For the case of the interstitial muon, an equivalent 'muon Knight shift' K_μ is apparent in the muon spin-precession frequency, where it is often considered a shift in the effective field,

$$K_\mu = \frac{\Delta\omega}{\omega} = \frac{\Delta B}{B_0}. \tag{5.1}$$

We have already seen a similar effect in the previous chapter in a form that is specific to high temperature semiconductors undergoing fast charge exchange. Knight shift could be thought of as the hyperfine interaction analogue of a chemical shift; in this case resulting from the distortion of the electron wave function by the surrounding nuclei. For the systems discussed here it is proportional to the density of states at the Fermi level.

If the Knight shift is the static average of the contact hyperfine interactions, then the fluctuations about this average give rise to a form of depolarisation known as Korringa relaxation [5.6]. The LF ($1/T_1$) relaxation is dominated by spin flip scattering of the conduction electrons and is described by the formula

$$\frac{1}{T_1} = \frac{4\pi k_B T}{\hbar}\left(\frac{\gamma_n}{\gamma_e}\right)^2 K_\mu^2. \tag{5.2}$$

An alternative derivation of muon relaxation, in terms of spin-density fluctuations [5.7],

yields the same $K_\mu^2 T$ proportionality for simple metals, only for the case of non-interacting electrons.

In normal metals, the large conduction electron density is conventionally understood to allow the formation of a screening "cloud"[‡], which reduces the Coulomb potential to the extent that the muon bound state cannot be formed. If the paramagnetic state exists it is expected to occur in the form of a Kondo impurity, with spin-flip scattering between the free electrons and the local moment of the impurity forming a spin-polarised electron cloud around it. In this case, the strong exchange interaction between the bound electron on the muon and electrons in the conduction band means that the paramagnetic state would still be difficult to distinguish directly. In general, the Kondo effect takes place below a characteristic temperature, T_K, and bestows a temperature-independent local magnetic susceptibility at the muon. Above T_K the screening cloud is "shaken off" by thermal motion and the magnetic susceptibility falls as $\frac{1}{T+T_K}$. The Knight shift is closely related to the local (Pauli) spin susceptibility and therefore provides a potential link to the existence of such states, and the measured relaxation.

Semimetals have carrier concentrations typical of a heavily doped semiconductor, although they have well-defined (but much reduced) Fermi surfaces at low temperatures[§]. Antimony has a large muon Knight shift and exhibits the qualitative behaviour of a Kondo impurity up to about 100 K, bismuth and arsenic on the other hand show no unusually large Knight shift [5.8]. It is clear that carrier density is not solely responsible for the formation of bound states in these materials. In fact, muon behaviour in semimetals is far from being understood, and the experiments in this chapter were intended as an exploration of general

‡ a region of enhanced electron density.
§ Bi was the first element to exhibit clear de Haas-van Alphen oscillations for this reason.

departures from these basic models at elevated temperatures; gathering more data on these systems for analysis based on probable charge- and spin- exchange interactions.

5.3 Experimental Details

The measurements were all performed on the EMU spectrometer at ISIS, where the spectrometer is optimised for LF studies (§ 1.5.1). The instrument furnace, covering the range 300 K to 1000 K, was used for these studies aimed at the high temperature regime. In practice, the upper temperature boundary was determined by the melting point of the sample. Lower temperatures, for the Hg, Pb and graphite samples, were achieved using a closed-cycle refrigerator (CCR) with a range of 12 K to 340 K.

Details of the samples are given in Table 5.1. They were the purest available [5.9] and took a variety of forms, which dictated whether they were simply wired directly to the sample mount or wrapped first in tantalum foil "packets". Containment of Hg, an exceptional case, is described in § 5.4. Sample orientation was not a consideration for any of these

Table 5.1. Experimental samples used in high-temperature enhanced relaxation studies

Element	Type	Purity (%)	Melting point (K)	Details
As	Semimetal	99.9999	886 (subl.)	Lumps 
Bi	Semimetal	99.9999	544	Broken ingot 
C (graphite)	Metal		3823	Several small blocks
Cd	Metal	99.999	593	foil (1mm thick)
Hg	Metal	99.9999	234	Liquid 
Pb	Metal	99.9999	601	Shot (lumps) 
Sb	Semimetal	99.9999	903	Lumps 

 - harmful

 - toxic

 - corrosive

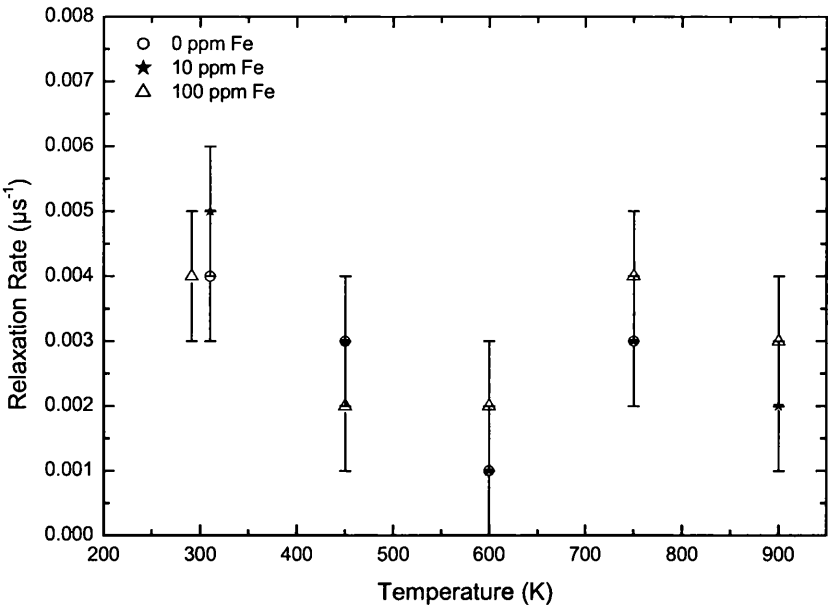

Figure 5.2 *Temperature-dependent muon relaxation rates for iron-doped copper samples were measured to gauge the possible effects of paramagnetic impurities on relaxation rate results. The various levels of Fe gave statistically identical results across the temperature range.*

experiments** (most samples were small lumps, a few mm in diameter, randomly oriented).

To exclude the possibility that our relaxation data could be falsified by muon trapping at magnetic impurities, control samples of Cu (99.9999% pure) doped with 10 and 100 ppm Fe were compared with an undoped sample. The instrument and sample environment was the same as that used for the experimental samples.

The doped copper results are shown in Figure 5.2. The results at each Fe concentration are identical, within statistical errors, and exhibit no significant variation across the temperature range. As our experimental samples were the purest available, and should not contain impurities exceeding a few ppm, these results indicate that impurity effects can be reasonably discounted in the following results.

** The muon Knight shift is assumed to be isotropic.

5.4 Results

The temperature dependent LF relaxation rates are shown in Figure 5.3 and Figure 5.4 for the semimetallic and metallic samples respectively (all are shown on axes starting at zero to allow visual comparison with an "expected" linear absolute temperature dependence). The full Korringa relaxation predictions, given by inserting available Knight shift values into equation (5.2), are also included. Apart from cadmium, K_μ values are not

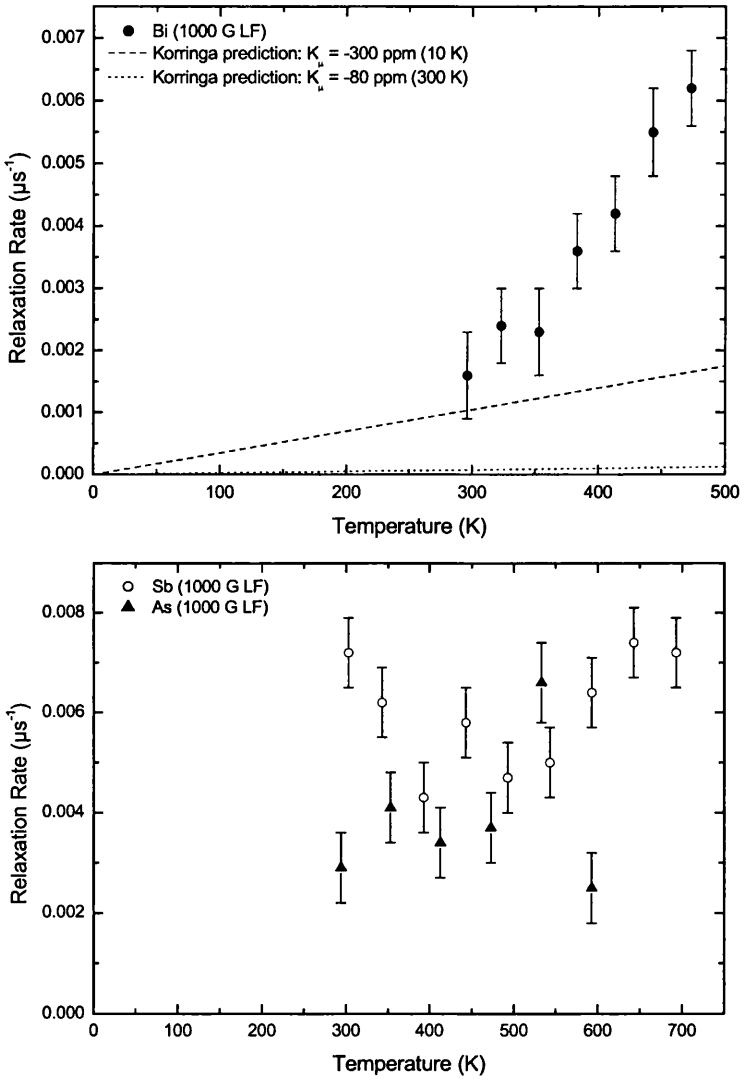

Figure 5.3 *Muon relaxation rates for the pentavalent semimetals. The Knight shift given for Bi at each temp is ±25 depending on orientation. Measurement temperatures for the Knight shift values are given in brackets.*

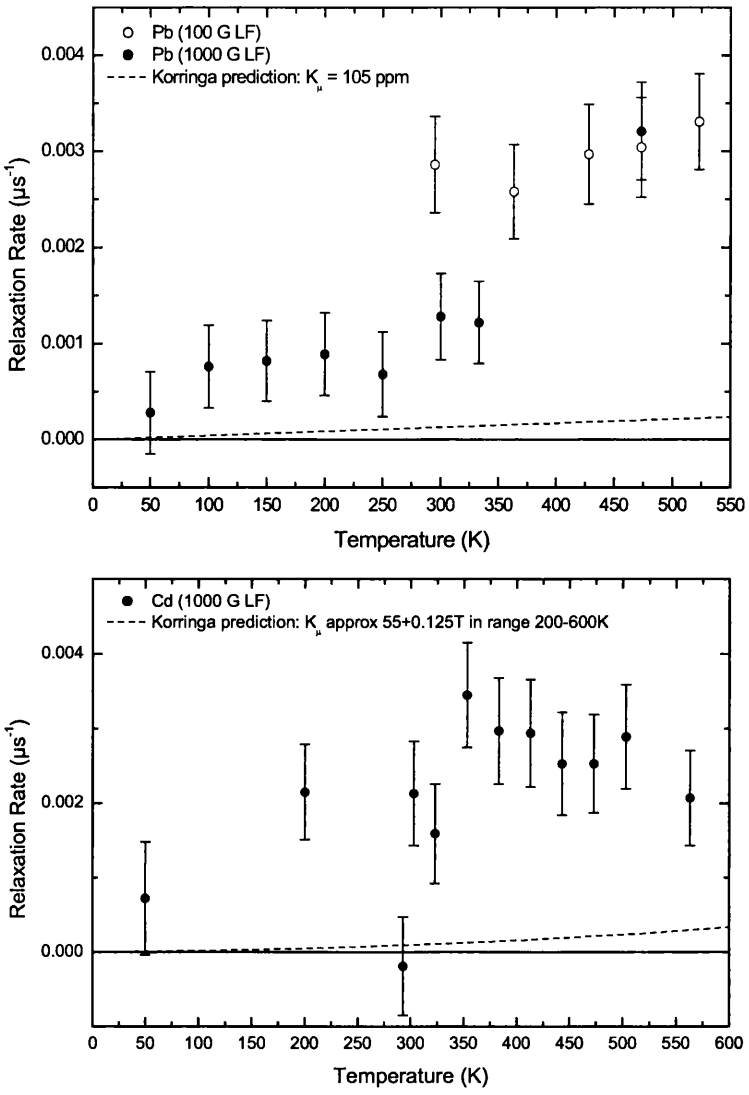

Figure 5.4 *Muon relaxation rates for the metals Pb and Cd, nearby the semimetals in the Periodic table. For the temperature dependence of the Muon relaxation rate in cadmium, the Korringa prediction is based on the known Knight shift across the entire measurement range.*

known across the full temperature range, so the predictions represent an assumed temperature-independent K_μ in these cases.

All the data are quite close to the limit of relaxation rate measurement at the ISIS pulsed source (§ 1.5)[††], making it difficult to define trends unambiguously. However, it is clear that

[††] The reason why significant relaxation rates had not been reported previously for these materials.

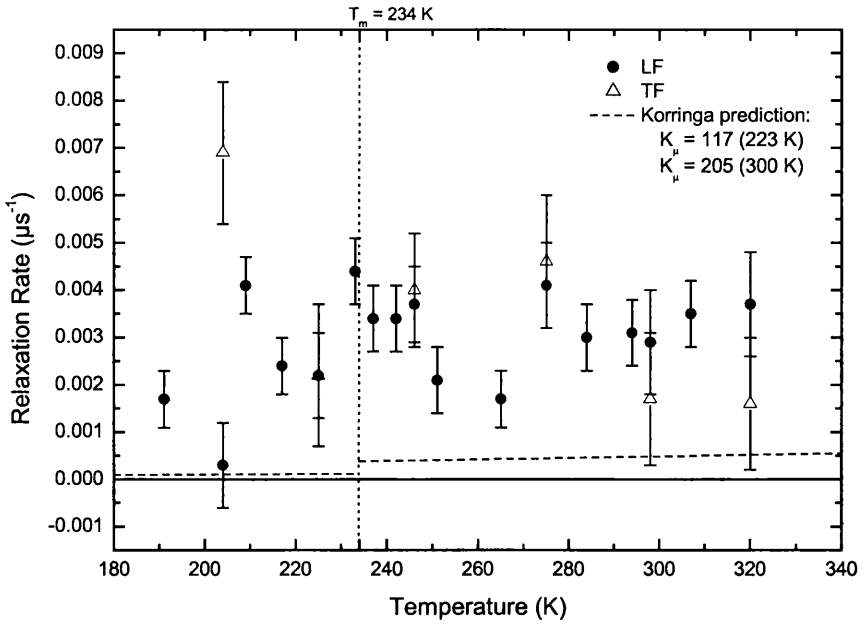

Figure 5.5 *Temperature dependence of the Muon relaxation rate across the melting point of Mercury. Measurement temperatures for the Knight shift values are given in brackets.*

relaxation rates exceed the Korringa prediction for all samples above room temperature.

Mercury posed a particular problem due to measurements through its phase transition. A welded titanium cell was used, with a small, convex piece of polystyrene taped firmly over the window to keep it in the concave position, against the pressure gradient, when the chamber around the cell was evacuated. Outward distortion of the window would cause redistribution of the sample in the liquid phase, and changes in its interaction with the muon beam, which could give rise to misleading results. Polystyrene was found to have sufficient strength to maintain the shape of the window, and was sufficiently porous to retain its integrity, under vacuum conditions.

Within the precision of the measurements (Figure 5.5), it is difficult to see if the relaxation rate is affected by the change of phase. In fact, there appears to be no statistically significant change in relaxation rate across the full temperature range studied.

5.5 Discussion

Where Knight shift data were available, all samples exhibited relaxation rates in excess of the predictions made according to the Korringa picture for simple metals. Of course, the exchange in energy during spin-flip scattering with the conduction electrons is very small, and means that only electrons within kT of the Fermi surface can take part. The direct proportionality between the $1/T_1$ and K_μ in equation (5.2) is therefore not expected to extend to very high temperatures, or to apply where there is a strong variation in the density of states at the Fermi surface – one of the characteristics of semimetals.

Arsenic and antimony both appear to show effects of these variations in their LF relaxation rates, although the results are difficult to interpret precisely, given the low rates and the relatively large statistical errors.

Several of the samples, most distinctly in Bi above room temperature, do however exhibit a linear increase in relaxation with temperature, and so are consistent with a form of Korringa relaxation.

By analogy with the semiconductor experiments detailed in Chapter 4, it may also prove useful to include mechanisms related to intermittent muonium formation. Bound states are expected to appear for electron densities lower than about $3\times10^{22}\,cm^{-3}$ [5.10], so for materials such as bismuth (which has a much lower electron density of $3\times10^{17}\,cm^{-3}$) it is very likely that muonium-like states will be involved; in which case the relaxation is expected to be enhanced by the same rapid charge- and/or spin- exchange mechanisms seen in semiconductors.

Ironically (since initial investigations of graphite prompted the research reviewed in this chapter), the existence of a completely different state has been identified as responsible for particular features of muon relaxation in graphite [5.11 and 5.12]. Theoretical calculations

[5.13] for muonium reacting with a single "graphene" fragment predict that the muonium (or hydrogen) atom bonds to one carbon, with the majority of the spin density on the six neighbouring carbons. It is likely that a similar molecular radical exists in graphite, although of course the muonium would be packed between two graphitic layers.

However, the consequences of this molecular radical model in interpreting the muon data are still ambiguous. One approach is, once again, to consider hot-semiconductor-like charge cycling; in the fast exchange limit for graphite, the appropriate expression is (recall equation (4.16))

$$\frac{1}{T_1} \approx \frac{2p_0\left(\pi A_\mu\right)^2}{W} \tag{5.3}$$

Given the theoretically calculated [5.11] hyperfine constant $A_\mu \approx 200$ MHz (due to the reduced spin density at the muon), and using frequency shift data of Chakhalian *et al* [5.4], one can derive a paramagnetic fraction, p_0, using the relation given in equation (4.12), which rises from approximately 1% near 100 K to a value close to unity at 800 K. The transition rate may then be calculated from equation (5.3). This is almost constant above room temperature and gives a lifetime of ~ 0.025 ps, and is most likely due to equilibrium with a positive ion. However, these results are quite preliminary as the C-Mu bond length and corresponding hyperfine constant will both increase with temperature.

The alternative model takes advantage of such structural changes to account for the temperature dependence of the muon Knight shift. A decrease in K_μ above about 500 K [5.4] is then in line with a Kondo impurity model appropriate to the molecular radical. However, in this model, the complexity in the energy dependence of the density of states must still be invoked to explain the anomalous muon relaxation rate.

6 CONCLUDING REMARKS AND FUTURE DIRECTIONS

The successful development of a pulsed low energy muon beam line at ISIS has been shown to allow accurate μSR depth-profiling to be carried out on multi-layer systems. Experiments also uniquely afforded the opportunity to directly measure the energy profile of moderated muons, providing further insight into the role of the band-gap of the rare gas solids. Details of optimal running conditions for this apparatus have been described and the experimental set-up has been critically evaluated.

Thin films and multilayers continue to be of scientific and technological importance, and the uniquely favourable qualities of the muon, with the addition of nanometer depth resolution, for which the pulsed approach is particularly effective, makes muon moderation a very desirable technique. The greater intensity promised of next-generation pulsed muon sources, such as the ESS, will allow all the advantages of conventional pulsed μSR to be brought to this field. The sample handling apparatus described here is independent of source type, based instead on generic requirements of surface investigation, and would add equal value to experiments running on a DC beam. With improved data rate, the experimental time gained via careful sample management will become increasingly significant.

The investigations of muons in Cab-O-Sil® have provided a clear distinction between different mechanisms of muonium production in fine silica powders. In this work, 16% of incident muons are found to form muonium via a mechanism apparently unrelated to the surface conditions; the most likely explanation is bulk formation. The further 24% of

muonium detected in the bare Cab-O-Sil® is shown to be formed at active sites on the bare powder surface, and is reduced by coverage of small amounts of noble gases. This is true irrespective of the gas used, and has allowed us to discount the hypothesis that muonium is stripped of its electron at the surface of the powder, in favour of this active surface production mechanism – inhibited *preferentially* by the gas atoms. Regardless of its formation mechanism, muonium spends almost its entire lifetime on the surface of the powder at 6 K.

In addition, we have identified a novel mechanism whereby muonium may be formed by recoil with the gas atoms. The yield of muonium, due to this recoil mechanism, increases with increasing gas coverage, and is responsible for up to a further 16% in muonium yield in the case of helium.

Similar investigations of paramagnetic asymmetry using neon will serve to confirm if this model is correct, as it should give results somewhere between those of helium and argon. Concurrent measurements of diamagnetic asymmetry will also allow the missing fraction to be investigated, and provide further confirmation and additional information on the delayed surface-formed component.

Direct measurements of the high temperature frequency shift in (near-intrinsic) silicon have shown the neutral muonium fraction, during rapid charge-exchange cycling, to be experimentally accessible. These measurements have also demonstrated that a simple 2-state model, based at the tetrahedral site, is insufficient in accounting for the muonium dynamics within this system. Inclusion of the bond-centred site with experimentally measured transition parameters immediately gave results more in line with our experimentally implied neutral fraction in this high-field approximation. Parametric state

populations have been generated for all expected states, based on equilibrium transition rates.

It is likely that the full 4-state model will be required to describe the dynamics of the system, and inclusion of the effects of time spent in Mu^0_{BC} on the precession frequency. Questions remain as to the full role of the negative charge state at the T site, and the problems associated with attempting to interpret the high temperature data in terms of the low temperature states. The ultimate resolution of these questions, in terms of a consistent set of parameters for electron capture and loss rates, accounting for both the frequency shift and spin relaxation rates, will provide a valuable model for the electrical activity of a hydrogen impurity at high temperature.

A series of muon spin relaxation measurements in semimetals and metals, close to the lower limit of resolution, have demonstrated a form of Korringa relaxation in which the hyperfine interaction between the muons and the conduction electrons plays a dominant role. The muon offers a further probe of conduction electron encounter at an interstitial site within these systems; linking the topic to the nature of defect screening in metals, to relaxation by spin-density fluctuations in magnetic materials and to spin- and charge-exchange on paramagnetic muonium centres in semiconductors. This opportunity is exclusive to μSR given the various difficulties associated with NMR studies of hydrogen in metals.

REFERENCES

1. Introduction

1.1 T Yamazaki, K Nagamine, S Nagamiya, O Hashimoto, K Sugimoto, K Nakai and S Kobayashi (1975). Negative muon spin rotation. *Physica Scripta*, **11** 133.

1.2 D C Walker, (1983). *Muon and Muonium Chemistry.* (CUP).

1.3 L Willmann and K Jungmann, (1997). The muonium atom as a probe of physics beyond the standard model. *Atomic Physics Methods in Modern Research, Lecture Notes in Physics* **499** 43.

1.4 C Caso *et al.*, (1998). Review of Particle Physics. *The European Physical Journal* C3.

1.5 S F J Cox, (1987). Implanted muon studies in condensed matter science. *J. Phys. C*, **20** 3187-3319.

1.6 A Schenck, (1985). *Muon Spin Rotation Spectroscopy.* (Hilger, Bristol).

1.7 J H Brewer, (1994). Muon Spin Rotation/ Relaxation/ Resonance. *Encyclopaedia Of Applied Physics*, **11** 23-53.

1.8 P Z Kunze, (1933). *Z. Phys.*, **83** 1.

1.9 S H Neddermeyer and C D Anderson, (1937). Note on the nature of cosmic-ray particles. *Phys. Rev.*, **51** 884.

1.10 K Tanikawa, S Sakata and T Inoue, (1946). *Prog. Theor. Phys.*, **1** 143.

1.11 C M G Lattes, H Muirhead, G P S Occhialini and C F Powell, (1947). Processes involving charged mesons. *Nature*, **159** 694.

1.12 T D Lee and C N Yang, (1956). Question of parity conservation in weak interactions. Phys. Rev., **104**, 1 254-258.

1.13 R L Garwin, L M Lederman and M Weinrich, (1957). Observations of the failure of conservation of parity and charge conjugation in meson decays: the magnetic moment of the free muon. Phys. Rev., **105** 1415-7.

1.14 G H Eaton, (1998). *Muon Facilities and Experiments.* (RAL Reports), RAL-TR-1998-019.

1.15 G Alexander *et al.*, (1967). *Phys. Rev.*, **154** 1284.

1.16 A E Piper, T Bowen and K R Kendal, (1976). *Nucl. Inst. Meth.*, **135** 39.

1.17 D Griffiths, (1987). *Introduction to Elementary Particles.* (John Wiley and Sons).

1.18 J Friedman and V L Telegdi, (1957). Nuclear Emulsion Evidence for Parity Nonconservation in the Decay Chain $\pi^+ - \mu^+ - e^+$. *Phys. Rev.*, **105** 1681.

1.19 J Orear, G Harris and E Bierman, (1957). *Phys. Rev.*, **107** 322-3.

1.20 G Schatz and A Weidinger, (1992). *Nukleare Festkörperphysik.* (B G Teubner)

1.21 D R Harshman (1986). The Interactions of Muonium with Silica Surfaces. PhD Thesis, The University of British Columbia.

1.22 K H Chow, (1994). Spin dynamics and electronic structure of muonium and its charged states in silicon and gallium arsenide. PhD Thesis, The University of British Columbia.

1.23 E Roduner and H Fischer, (1981). *Chem. Phys.*, **54** 261.

1.24 E Holzschuh, W Kündig and B D Patterson, (1981). Direct measurement of the muonium hyperfine frequencies in quartz. *Helv. Phys. Act.*, **54** 552-560.

2. Slow muons

2.1 Workshop on applications of low energy muons to solid state phenomena, PSI, 1999 (unpublished).

2.2 J Brewer – comments made at Workshop on applications of low energy muons to solid state phenomena, PSI, 1999.

2.3 J F Zeigler, (1996). *The stopping and range of ions in solids.* (Pergamon Press, New York).

2.4 C Bucci, (1998) – private communication.

2.5 S L Lee, S H Kilcoyne and R Cywinski, (1999). *Muon Science: Muons in Physics, Chemistry and Materials.* (SUSSP & IOP Publishing).

2.6 K Träger, (1999). Doctoral thesis. Heidelberg University.

2.7 J Merkel, (1998). Doctoral thesis. Heidelberg University.

2.8 K Nagamine, Y Miyake, K Shimomura, P Birrer, J P Marangos, M Iwasaki, P Strasser and T Kuga, (1995). Ultraslow positive-muon generation by laser ionisation of thermal muonium from hot tungsten at primary proton beam. *Phys. Rev. Lett.*, **74** (24) 4811-4814.

2.9 K Träger, (1998) – private communication.

2.10 E M Gullikson and A P Mills, Jr., (1986). *Phys. Rev. Lett.*, **57** 376.

2.11 J Jääskeläinen, T Laine, K Fallström, K Saarinen and P Hautojärvi, (1997). Optimized growth conditions for solid Ar and Kr moderators in slow positron beam. *Appl. Surf. Sci.*, **116** 73.

2.12 E Morenzoni, F Kottmann, D Maden, B Matthias, M Meyberg, Th Prokscha, Th Wutzke and U Zimmermann, (1994). Generation of Very Slow Polarised Positive Muons. *Phys. Rev. Lett.*, **72** 2793.

2.13 E Morenzoni, Th Prokscha, A Hofer, B Matthias, M Meyberg, Th Wutzke, H Glückler, M Birke, J Litterst, Ch Neidermayer and G Schatz, (1997). Characteristics of condensed gas moderators for the generation of very slow polarized muons. *J. Appl. Phys.*, **81** (8) 3340.

2.14 E Morenzoni, (1998). *Physics and Applications of Low Energy Muons.* (PSI Publication), PSI-PR-98-23.

2.15 T Prokscha, E Morenzoni, C David, A Hofer, H Glückler and L Scandella, (2001). Moderator gratings for the generation of epithermal positive muons. *Appl. Surf. Sci.*, **172** 235-244.

2.16 J A Venables and B L Smith, (1977). *Rare Gas Solids, Vol. 2.* M L Klein and J A Venables (ed.). (Academic Press, NY) 609.

2.17 T Prokscha, (1994). PhD Thesis. Heidelberg University. Cited in [2.6].

2.18 A Breitrück, (1998). Diploma Thesis. Heidelberg University.

2.19 M P Petkov, K G Lynn, L O Roellig and T D Troev, (1997). An investigation of positrons interacting with solid argon, krypton and xenon. *Appl. Surf. Sci.*, **116** 13-18.

2.20 Y Nakai, T Shirai, T Tabata and R Ito, (1987). *At. Data Nucl. Data Tables*, **37** 69.

2.21 U Rössler, (1977). *Rare Gas Solids, Vol. 1.* M L Klein and J A Venables (ed.). (Academic Press, NY) 505. – cited in [2.6]

2.22 E M Gullikson and A P Mills Jr., (1990). *Phys. Rev.*, **70** 1098. – cited in [2.6]

2.23 R C Weast (ed.), (1988). *Handbook Of Chemistry And Physics.* (CRC Press)

2.24 Gresham Scientific Instruments. Gresham Lion House, Filedhouse Lane, Marlow, Buckinghamshire, SL7 1TB, UK.

2.25 C Bucci, (1998) – private communication.

2.26 R Scheuermann, (1998) – private communication.

2.27 C Bucci, (1998) – private communication.

2.28 Caburn-MDC Limited, The Old Dairy, The Street, Glynde, East Sussex BN8 6SJ UK. http://www.caburn.co.uk/

2.29 Pfeiffer Vacuum Technology AG, Berliner Str. 43, 35614 Asslar, Germany. http://www.pfeiffer-vacuum.de/

2.30 Oxford Instruments PLC, Tubney Woods, Abingdon, Oxon OX13 5QX, UK http://www.oxinst.com/

2.31 B Pachl, (1998) – private communication.

2.32 ESS developments may be tracked at http://www.ess-europe.de/.

2.33 F Foroughi, E Morenzoni, T Prokscha, M Daum, K Deiters, D George, D Herlach, C Petitjean, D Renker and V Vrankovic, (2002). Upgrading the PSI Muon Facility. *Hyp. Int.*, to be published.

2.34 E Morenzoni, E M Forgan, H Glückler, T J Jackson, H Luetkens, Ch Niedermayer, T Prokscha, T M Riseman, M Birke, A Hofer, J Litterst, M Pleines, and G Schatz, (2001). Muon spin rotation and relaxation experiments on thin films, *Hyp. Int.* **133** 179-195.

2.35 A Schenck – comments made at Workshop on applications of low energy muons to solid state phenomena, PSI, 1999.

3. Cab-O-Sil®

3.1 D R Harshman, (1986). Doctoral Thesis. University of British Columbia.

3.2 G M Marshall, J B Warren, D M Garner, G S Clark, J H Brewer and D G Fleming, (1978). Production of thermal muonium in the vacuum between the grains of fine silica powders. *Phys. Lett.*, **65A** (4) 351-353.

3.3 Cabot GmbH. Postfach 90 11 20, D-63420 Hanau. http://www.cabot-corp.com/

3.4 M Heming and E Roduner, (1987). Formation and dynamics of a SiO_2-adsorbed radical observed by muon spin rotation. *Surf. Sci.*, **189/190** 535-542.

3.5 I D Reid, T Azuma and E Roduner, (1990). Probing the behaviour of surface-adsorbed free radicals using ALC μSR. *Hyp. Int.*, **65** 879-890.

3.6 *Cab-O-Sil® Untreated Fumed Silica Properties and Functions*, (1993). Brochure courtesy of the Cabot Corporation [3.3].

3.7 D R Harshman, (1986). Muon/Muonium surface interactions. *Hyp. Int.*, **32** 847-863.

3.8 R E Turner and M Senba, (1984). Proceedings of the Yamada Conference VII, Muon Spin Rotation, Shimoda, Japan. *Hyp. Int.*, **17-19** 697.

3.9 Y Ito, B W Ng, Y C Jean and D C Walker, (1981) *Hyp. Int.*, **8** 355. Cited in [3.1]

3.10 R F Kiefl, J B Warren, C J Oram, G M Marshall, J H Brewer, D R Harshman, and C W Clawson, (1982). Surface interactions of muonium in oxide powders at low temperatures. *Phys. Rev. B*, **26** (5) 2432-2441.

3.11 J H Brewer, (1981). *Hyp. Int.*, **8** 375. cited in [3.10].

3.12 R F Kiefl, B D Patterson, E Holzschuh, W Odermatt, and D R Harshman, (1983). Hyperfine splitting of muonium in SiO_2 powder. *Hyp. Int.*, **17-19** 563-566.

3.13 I Langmuir, (1918). The Adsorption of Gases on Plane surfaces of Glass, Mica and Platinum. *J. Am. Chem. Soc.*, **40** 1361-1404.

3.14 S Brunauer, P H Emmett, E Teller, (1938). Adsorption of gases in multimolecular layers. *J. Am. Chem. Soc.*, **60** 309.

3.15 R C Weast (ed.), (1988). *Handbook Of Chemistry And Physics.* (CRC Press)

3.16 M Charlton, S F J Cox, P A Donnelly and E Roduner, (2001). *Muonium studies of hydrogen spillover on heterogeneous catalysts.* (Isis Experimental Report), RB11945.

3.17 F L Pratt, (1997). Repolarisation of anisotropic muonium in orientationally disordered solids. *Phil. Mag. Lett.*, **75** (6) 371-379.

3.18 R F Kiefl, J B Warren, G M Marshall, C J Oram and C W Clawson, (1981). Muonium in the condensed phases of Ar, Kr, and Xe. *J. Chem. Phys.*, **74** (1) 308-313.

4. Semiconductors

4.1 B Bech Nielsen, (1997). *Phys. Rev. Lett.*, **79** 1507.

4.2 J Schüth, P-D Eversheim, P Herzog, K Maier, G Majer, P Meyer, E Roduner, (2000). Replacing muons by protons: polarised beam NMR. *Physica B*, **289-290** 672-675.

4.3 B D Patterson, (1988). Muonium states in semiconductors. *Rev. Mod. Phys*, **60** 69-159.

4.4 E Roduner, A Schenck, G Solt, (2000). μSR '99: Proceedings of the 8th International Conference on Muon Spin Rotation, Relaxation and Resonance. (Elsevier Science) Section 5.

4.5 S F J Cox and M C R Symons, (1986). *Chem. Phys. Lett.*, **126** 516.

4.6 B Bech Nielsen, K Bond Nielsen and J R Byberg, (1994). Charge and site-change dynamics of muonium (hydrogen) in Si. *Materials Science Forum*, **143-147** 909.

4.7 C G Van de Walle, P J H Denteneer, Y Bar Yam and S T Pantelides, (1989). Title*. *Phys. Rev. B*, **39** 10791.

4.8 S R Kreitzman, B Hitti, R L Lichti, T L Estle and K H Chow , (1995). Muon-spin-resonance study of muonium dynamics in Si and its relevance to hydrogen. *Phys. Rev. B*, **51** 13117.

4.9 K H Chow, R F Kiefl, J W Schneider, B Hitti, T L Estle, R L Lichti, C Schwab, R C Duvarney, S R Kreitzman, W A Mcfarlane and M Senba, (1993). Muonium dynamics in Si at high temperatures. *Phys. Rev. B*, **47** (23) 16004-16007.

4.10 Commission on Atomic Weights and Isotopic Abundances report for the International Union of Pure and Applied Chemistry in *Isotopic Compositions of the Elements 1989*, Pure and Applied Chemistry, 1998, **70**, 217. [Copyright 1998 IUPAC]
cited in http://www.webelements.com/webelements/elements/text/Si/isot.html

4.11 K H Chow, (1994). Spin dynamics and electronic structure of muonium and its charged states in silicon and gallium arsenide. PhD Thesis, The University of British Columbia.

4.12 M Senba, (1991). Spin dynamics of the positive muon radicals in the presence of rapid electron spin exchange: frequency shift and relaxation. *J. Phys. B*, **24** 3531-3549.

4.13 F Buda, G L Charriotti, R Car and M Parinello, (1989). Proton Diffusion in Crystalline Silicon. *Phys. Rev. Lett.*, **63** 294.

4.14 A Abragam, (1961). *The Principles of Nuclear Magnetism.* (OUP)

4.15 B Hitti, S R Kreitzman, T E Estle, E S Bates, M R Dawdy, T L Head and R L Lichti, (1999). Dynamics of negative muonium in n-type silicon. *Phys. Rev. B*, **59** 4918.

5. Semimetals

5.1 R A Mercuri, J J Gough, B S Fedor and M L Wardrup, (1999). GRAFOIL® 2000 - an improved gasket material. *(Technical Report – Ucar Carbon Company Inc.).* GRAFOIL® is a registered trademark of UCAR Carbon Company – a subsidiary of Graftech International Ltd.

5.2 S F J Cox, M Charlton and S P Cottrell, (1998). *ISIS Annual Report*, Experiment RB9182.

5.3 A Schenck, (1985). *Muon Spin Rotation Spectroscopy.* (Hilger, Bristol).

5.4 J A Chakhalian and R F Keifl, (1999) – private communication of TRIUMF Report on Experiment E758.

5.5 W D Knight, (1949). *Phys. Rev.*, **76** 1549.

5.6 J Korringa, (1950). *Physica*, **16** 601.

5.7 S J Blundell and S F J Cox, (2001). Longitudinal muon spin relaxation in metals and semimetals and the Korringa law. *J. Phys.: Condens. Mat.*, **13** 2163-2168.

5.8 O Hartmann, E Karlsson, L -O Norlin, K Pernestal, M Borghini and T O Niinikoski, (1979). Temperature and magnetic field dependence of the muonic Knight shift in antimony. *Hyp. Int.*, **6** 47-50.

5.9 Goodfellow Cambridge Ltd. Ermine Business Park, Huntingdon, Cambridgeshire, PE29 6WR, England. http://www.goodfellow.com/

5.10 S Estreicher and P F Meier, (1983). Energy profiles for light impurities in simple metals. *Phys. Rev. B*, **27** 642.

5.11 S F J Cox, S P Cottrell, M Charlton, P A Donnelly, C Ewels, M Heggie and B Hourahine, (2001). A molecular radical model for hydrogen and muonium in graphite. *J. Phys.: Condens. Mat.*, **13** 2196-2175.

5.12 J A Chakhalian, R F Kiefl, S R Dunsiger, W A Macfarlane, R Miller, J E Sonier and J E Fischer, (2002). Evidence for local moment formation around a positive muon in graphite. *Phys. Rev. B*, **66** 115107.

5.13 R Jones and P R Briddon, (1998). *Semicond. Semimet. A*, **51** 287.

APPENDIX I. NOBLE GAS VAPOUR PRESSURE CURVES

These vapour-pressure curves are plotted from tabulated values in [3.15] and are used as a guide to selecting an appropriate growth temperature for the partial gas layers in the silica powder studies in Chapter 3:

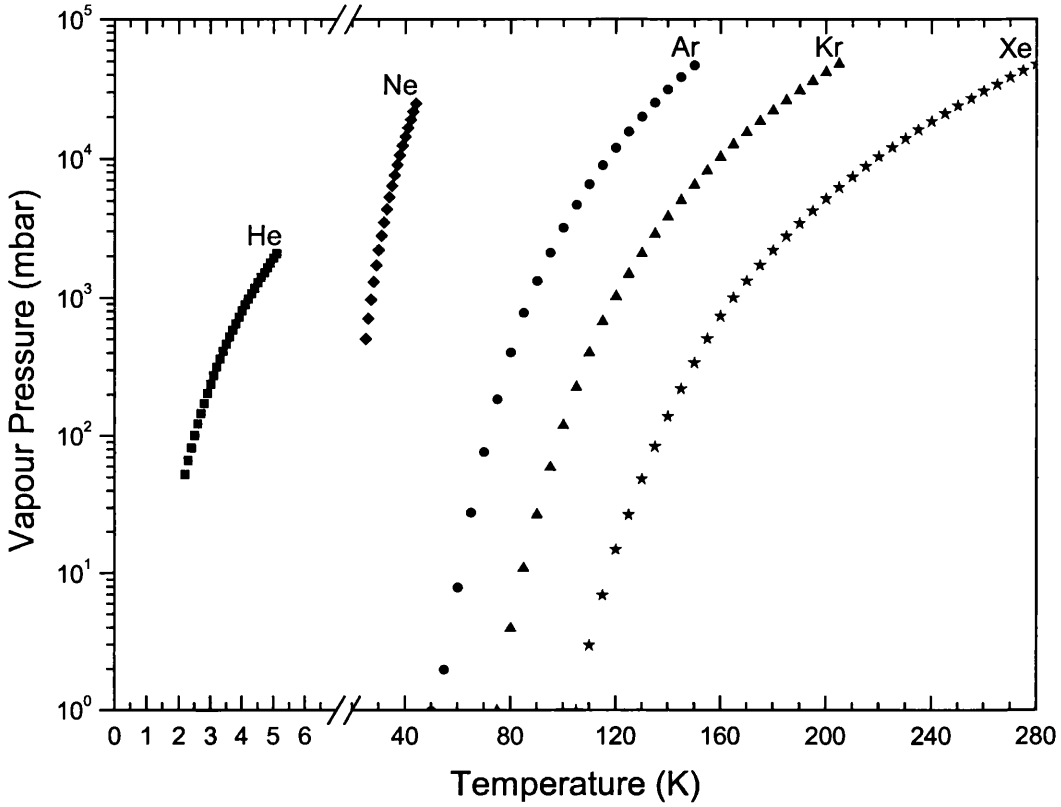

APPENDIX II. ALTERNATIVE CONDENSED GAS RESULTS

Mu asymmetry results (cf. Figure 3.15) for condensed gases on Cab-O-Sil®, presented as a function of adsorbed gas atoms (i.e. before calibration for monolayer coverage):

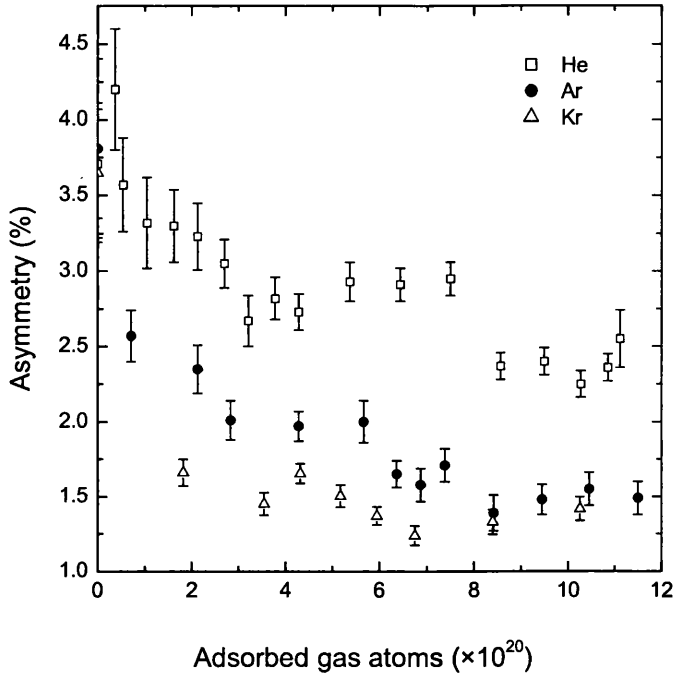

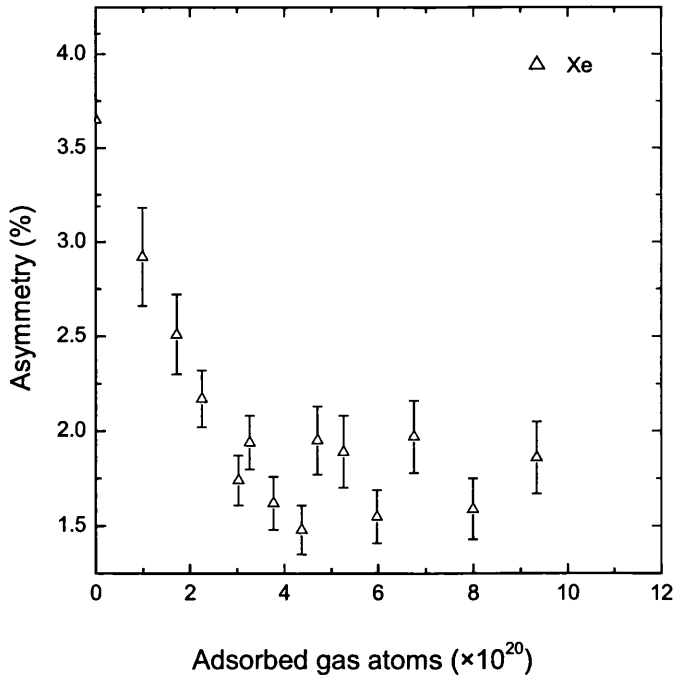

APPENDIX III. RELATIVE STATE FRACTIONS IN Si

As the occupation of Mu_T^0 in Si at equilibrium can be formulated for the site- and charge-exchange models of chapter 4, so may the occupation of the remaining states. We present here the corresponding state occupations for the basic 3- and 4-state models, where the occupation f_i of state i is given in terms of transition rates defined in chapter 4.

3-State: ($1=Mu_{BC}^+$, $2=Mu_T^0$, $3=Mu_{BC}^0$)

$$f_1 = \frac{W_{31}W_{23}}{K},$$

$$f_2 = \frac{W_{12}W_{31} + W_{12}W_{32} + W_{13}W_{32}}{K},$$

$$f_3 = \frac{W_{12}W_{23} + W_{13}W_{23}}{K},$$

where $K = W_{12}W_{31} + W_{12}W_{23} + W_{13}W_{23} + W_{31}W_{23} + W_{12}W_{32} + W_{13}W_{32}$.

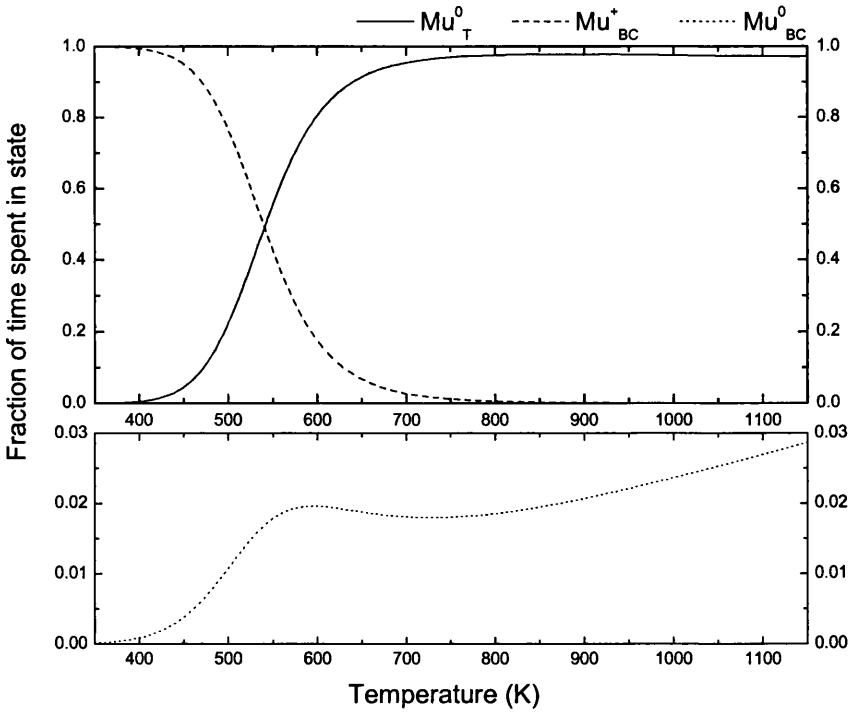

State occupations as a function of temperature according to the transition rates given by Hitti et al [4.15]. Note the smaller scale required to illustrate the neutral BC state – the stable state at low temperatures.

4-State: ($1=Mu^{+}_{BC}$, $2=Mu^{0}_{T}$, $3=Mu^{0}_{BC}$, $4=Mu^{-}_{T}$)

$$f_1 = \frac{W_{31}W_{23}W_{42}}{M}$$

$$f_2 = \frac{W_{12}W_{31}W_{42} + W_{12}W_{32}W_{42} + W_{13}W_{32}W_{42} + W_{12}W_{42}W_{34} + W_{13}W_{42}W_{34}}{M},$$

$$f_3 = \frac{W_{12}W_{23}W_{42} + W_{13}W_{23}W_{42}}{M},$$

$$f_4 = \frac{W_{12}W_{31}W_{24} + W_{12}W_{32}W_{24} + W_{13}W_{32}W_{24} + W_{12}W_{23}W_{34} + W_{13}W_{23}W_{34} + W_{12}W_{24}W_{34} + W_{13}W_{24}W_{34}}{M},$$

where $M = W_{12}W_{31}W_{24} + W_{12}W_{32}W_{24} + W_{13}W_{32}W_{24} + W_{12}W_{31}W_{42} + W_{12}W_{23}W_{42} + W_{13}W_{23}W_{42} + W_{31}W_{23}W_{42} + W_{12}W_{32}W_{42} + W_{13}W_{32}W_{42} + W_{12}W_{23}W_{34} + W_{13}W_{23}W_{34} + W_{12}W_{24}W_{34} + W_{13}W_{24}W_{34} + W_{12}W_{42}W_{34} + W_{13}W_{42}W_{34}$.

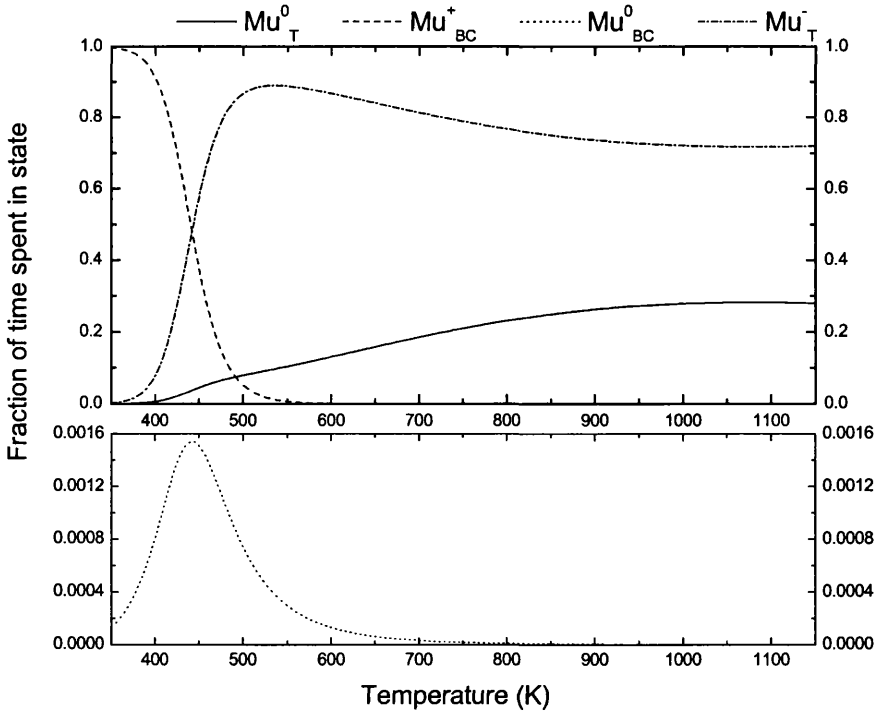

State occupations as a function of temperature according to the transition rates given by Hitti et al [4.15]. Note the even smaller scale required to illustrate the neutral BC state, and the dominance of the negative ion at temperatures above 450 K.